

NONEQUILIBRIUM CONTROL OF BROKEN-SYMMETRY PHASES IN  
QUANTUM MATERIALS

DISSERTATION

ZUR ERLANGUNG DES DOKTORGRADES AN DER FAKULTÄT FÜR  
MATHEMATIK, INFORMATIK UND NATURWISSENSCHAFTEN

FACHBEREICH PHYSIK  
DER UNIVERSITÄT HAMBURG

VORGELEGT VON

TOBIA F. NOVA

AUS MAILAND, ITALIEN

HAMBURG

2019



NONEQUILIBRIUM CONTROL OF BROKEN-SYMMETRY PHASES IN  
QUANTUM MATERIALS

TOBIA F. NOVA



A low-energy approach

Tobia F. Nova: *Nonequilibrium control of broken-symmetry phases in quantum materials*, A low-energy approach, © 15 October 2019

GUTACHTER DER DISSERTATION:

Prof. Dr. Andrea Cavalleri

Prof. Dr. Martin Eckstein

ZUSAMMENSETZUNG DER PRÜFUNGSKOMMISSION:

Prof. Dr. Andrea Cavalleri

Prof. Dr. Martin Eckstein

PD Dr. Guido Meier

Prof. Dr. Franz Kärtner

Prof. Dr. Michael Rübhausen

VORSITZENDER DER PRÜFUNGSKOMMISSION:

Prof. Dr. Michael Rübhausen

DATUM DER DISPUTATION:

09.12.2019

VORSITZENDER DES PROMOTIONS-AUSSCHUSSES:

Prof. Dr. Günter H. W. Sigl

DEKAN DER FAKULTÄT MIN:

Prof. Dr. Heinrich Graener

LEITER DES FACHBEREICH PHYSIK:

Prof. Dr. Wolfgang Hansen



---

## DECLARATION

---

Hiermit erkläre ich an Eides statt, dass ich die vorliegende Dissertationsschrift selbst verfasst und keine anderen als die angegebenen Quellen und Hilfsmittel benutzt habe. Diese Arbeit lag noch keiner anderen Person oder Prüfungsbehörde im Rahmen einer Prüfung vor.

I hereby declare, on oath, that I have written the present dissertation on my own and have not used other than the mentioned resources and aids. This work has never been presented to other persons or evaluation panels in the context of an examination.

*Hamburg, 15 October 2019*

---

Tobia F. Nova



A Tommaso, Maddalena e Roberto



---

## ABSTRACT

---

Quantum materials owe their remarkable properties to a delicate balance among many interacting degrees of freedom. Such precarious equilibrium renders these systems exceptionally sensitive to external stimuli. Even small perturbations can induce a multitude of diverse phases resulting in colossal changes in the materials functionalities.

The understanding of the microscopic interactions that govern these phenomena and the engineering of their collective responses have been long-standing goals of both fundamental and technological importance. In the last decades, significant effort has been made towards the control of quantum materials with intense ultrashort light fields. Laser pulses at terahertz and mid-infrared frequencies are particularly remarkable as they allow for the selective excitation of collective modes at their intrinsic energy scales. In particular, the optical excitation of infrared-active phonons to large amplitudes, which drives materials into highly nonlinear regimes, has proven to be a formidable tool for controlling electronic functionalities.

This thesis investigates how nonlinearities of the crystal lattice can be exploited to induce or control broken symmetry phases in quantum materials. In the first part of this thesis, I will show how the optical excitation of phonons promotes and stabilizes a dormant ferroelectric state that would be otherwise thermally inaccessible. Strontium Titanate ( $SrTiO_3$ ) is a quantum paraelectric where dipolar correlations grow with decreasing temperatures, albeit long-range order never sets in. The nonlinear excitation of lattice vibrations will be shown to break inversion symmetry and induce a metastable ferroelectric phase that survives for hours after the pump is removed. Spatially resolved

optical and electrical measurements reveal that the phenomenon is initiated by strain-activated flexoelectric polarizations.

In the second part of the thesis, I will show that nonlinear phonon excitation can also be used to manipulate the order parameter of a preexisting broken symmetry phase. The simultaneous excitation of pairs of non-degenerate orthogonal phonons generates circularly polarized phononic fields that couple directly to the magnetization of the canted antiferromagnet  $ErFeO_3$ . This time-reversal symmetry breaking atomic motion mimics the application of a magnetic field pulse which results in the excitation of a coherent magnon.

---

## ZUSAMMENFASSUNG

---

Quantenmaterialien verdanken ihre bemerkenswerten Eigenschaften einem empfindlichen Gleichgewicht zwischen vielen interagierenden Freiheitsgraden. Ein derart prekäres Gleichgewicht macht diese Systeme besonders empfindlich gegenüber äußeren Reizen. Bereits kleine Störeinflüsse können eine Vielzahl von unterschiedlichen Phasen induzieren, was zu kolossalen Änderungen der Materialeigenschaften führt.

Das Verständnis der mikroskopischen Wechselwirkungen, die diese Phänomene steuern, und die gezielte Beeinflussung ihrer kollektiven Reaktionen sind seit langem Ziele von grundlegender und technologischer Bedeutung. In den letzten Jahrzehnten wurden erhebliche Anstrengungen zur Kontrolle von Quantenmaterialien mit intensiven ultrakurzen Lichtfeldern unternommen. Laserpulse im Terahertz- und mittleren Infrarotbereich sind hier besonders erwähnenswert, da sie die selektive Anregung kollektiver Moden auf ihren intrinsischen Energieskalen ermöglichen. Insbesondere die optische Anregung von infrarotaktiven Phononen zu großen Amplituden, die Materialien in hochgradig nichtlineare Zustände treibt, hat sich als ein hervorragendes Werkzeug zur Steuerung der elektronischen Eigenschaften erwiesen.

Diese Arbeit untersucht, wie Nichtlinearitäten des Kristallgitters genutzt werden können, um in Quantenmaterialien Phasen mit Symmetriebrechung zu induzieren oder zu kontrollieren. Im ersten Teil dieser Arbeit werde ich zeigen, wie die optische Anregung von Phononen einen "schlafenden" ferroelektrischen Zustand begünstigt und stabilisiert, der sonst thermisch nicht zugänglich wäre. Strontiumtitanat ( $\text{SrTiO}_3$ ) ist ein quantenparaelektrisches Material, bei dem die dipolaren Korrelationen mit abnehmenden Temperaturen wachsen, wenngleich

eine langreichweitige Ordnung nie eintritt. Es zeigt sich, dass die nichtlineare Anregung von Gittervibrationen zu einer Brechung der Inversionssymmetrie führt und eine metastabile ferroelektrische Phase induziert, die noch stundenlang nach Abschaltung der externen Anregung überlebt. Ortsaufgelöste optische und elektrische Messungen zeigen, dass das Phänomen durch spannungsaktivierte flexoelektrische Polarisierungen ausgelöst wird.

Im zweiten Teil der Arbeit werde ich zeigen, dass nichtlineare Phononenanregung auch dazu verwendet werden kann, den Ordnungsparameter einer bereits existierenden gebrochenen Symmetriephase zu manipulieren. Die gleichzeitige Anregung von Paaren nicht-degenerierter orthogonaler Phononen erzeugt zirkular polarisierte Phononenfelder, die direkt an die Magnetisierung des gekippten Antiferromagneten  $\text{ErFeO}_3$  gekoppelt sind. Diese die Zeitumkehr brechende Atombewegung imitiert die Anwendung eines Magnetfeldpulses und führt zur Anregung einer kohärenten Spinpräzession.

---

## PUBLICATIONS LIST

---

The content of this thesis is based on the two main experiments that I carried out during my PhD at the Max Planck Institute for the Structure and Dynamics of Matter in Hamburg:

1. **T. F. Nova**, A. S. Disa, M. Fechner, and A. Cavalleri, *Metastable ferroelectricity in optically strained SrTiO<sub>3</sub>*, *Science*, 364, 6445, 1075-1079 (2019).
2. **T. F. Nova**, A. Cartella, A. Cantaluppi, M. Först, D. Bossini, R. V. Mikhaylovskiy, A. V. Kimel, R. Merlin, and A. Cavalleri, *An effective magnetic field from optically driven phonons*, *Nature Physics*, 13, 2, 132–136 (2017).

I also collaborated on research projects that are not or are only marginally part of this thesis:

1. A. Cartella, **T. F. Nova**, M. Fechner, R. Merlin, and A. Cavalleri, *Parametric amplification of optical phonons*, *PNAS* 115 (48), 12148-12151 (2018).
2. A. Cartella, **T. F. Nova**, A. Oriana, G. Cerullo, M. Först, C. Manzoni, and A. Cavalleri, *Narrowband carrier-envelope phase stable mid-infrared pulses at wavelengths beyond 10  $\mu\text{m}$  by chirped-pulse difference frequency generation*, *Optics Letters*, 42, 4, 663-666 (2017).
3. A. S. Disa, M. Fechner, **T. F. Nova**, B. Liu, J. Chen, M. Seo, M. Först, P. G. Radaelli, A. Cavalleri, *Polarizing an antiferromagnet by optical engineering of the crystal field*, (in preparation)



---

## CONTENTS

---

### I AN INTRODUCTION

- 1 INTRODUCTION 3
- 2 NONLINEAR LATTICE CONTROL 11
  - 2.1 Phonons in insulators - linear response 12
    - 2.1.1 Infrared-active phonons: charged harmonic oscillators 12
    - 2.1.2 Light-phonon interaction: phonon-polariton formation and optical response 17
  - 2.2 Nonlinear phononics 20
    - 2.2.1 Lattice anharmonicities and ionic Raman scattering 22
    - 2.2.2 Transient structural control of correlated phases 27

### II LIGHT-INDUCED SYMMETRY BREAKING

- 3 OPTICALLY-INDUCED METASTABLE FERROELECTRICITY 33
  - 3.1  $SrTiO_3$ : a failed ferroelectric 33
  - 3.2 Statically-induced ferroelectricity 37
  - 3.3 Optically-induced ferroelectricity 40
  - 3.4 Phonon-induced strain 58
  - 3.5 Flexoelectric domains 62
    - 3.5.1 Domain distribution 66
  - 3.6 Conclusions 72

### III PHONON-DRIVEN MAGNETIZATION CONTROL

- 4 PHONON-DRIVEN MAGNON EXCITATION 75
  - 4.1 The Erbium Orthoferrite  $ErFeO_3$  75
    - 4.1.1 Crystal structure and lattice vibrations 76

4.1.2	Magnetic properties	78
4.1.3	Megneto-optics	82
4.2	Experimental observation of phonon-driven effective magnetic fields	87
4.3	Conclusions	100
IV CONCLUSIONS		
5	CONCLUSIONS	105
V APPENDIX		
A	PARAMETRIC AMPLIFICATION OF OPTICAL PHONONS	111
B	EXPERIMENTAL SETUP	121
	BIBLIOGRAPHY	133

Part I

AN INTRODUCTION



---

## INTRODUCTION

---

**PHASE TRANSITIONS AND SYMMETRY BREAKING** Phase transitions are ubiquitous in nature. In our everyday life, we are mostly familiar with those induced by changes in temperature such as the transformation of water into ice. Typically, the high-temperature phase is more “disordered”, as in liquid water where the molecules are randomly distributed (Fig. 1.1A, top). On the contrary, the low-temperature phase is usually more “ordered”, as in ice where the molecules crystallize in a discrete periodic arrangement (Fig. 1.1A, bottom). These distinct phases can be identified by their symmetry. A physical system is said to be symmetric if its characteristics remain unchanged after being subjected to a variety of symmetry transformations, such as spatial translations and rotations. Water “looks” the same everywhere and from every angle. For example, a rotation of Fig. 1.1A would leave the pattern, or rather the lack thereof, unchanged. For this reasons, water possess continuous translational and rotational symmetry. On the other hand, ice has an intrinsically lower symmetry because there are fewer operations that leave the solid invariant. For example, only rotations of multiples of 60 degrees leave the lattice of Fig.1.1A unchanged.

The concept that across a phase transition a system loses a symmetry, referred to as *spontaneous symmetry breaking*, is quite general and lies at the heart of many fundamental properties of nature. Indeed, as famously captured by Pierre

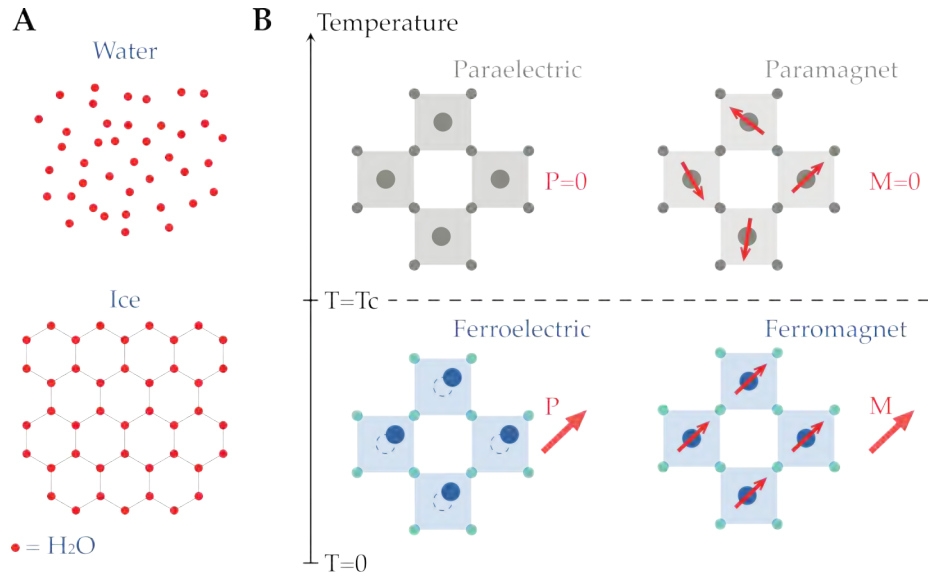


Figure 1.1: Spontaneous symmetry breaking. (A) Structure of water (top) and ice (bottom). (B) Left panel: Above the critical temperature, the material is paraelectric and possesses a center of inversion. Below  $T_c$ , the system undergoes a structural transition and breaks inversion symmetry, resulting in a macroscopic polarization  $P$ . Right panel: The spins in a paramagnet are randomly oriented. Below  $T_c$ , the spins order in a preferential direction resulting in a macroscopic magnetization  $M$ .

Curie: “c’est la dissymétrie qui crée le phénomène”, it is the dissymmetry that creates the phenomenon. When a symmetry is lost, a functionality can be gained. A common example consists in the symmetry breaking occurring across a paraelectric-to-ferroelectric phase transition. Above a certain critical temperature  $T_c$ , the structure of a paraelectric material is highly symmetric and it possesses a center of inversion. In this case, an electrical polarization cannot develop. When the material is cooled below  $T_c$ , a structural instability forces some ions to collectively move “off-center” in one specific direction. The lattice deformation allows for the formation of a long-range ferroelectric state, characterized by a macroscopic electrical polarization  $P$  (Fig. 1.1B, left). The system has now a lower symmetry and it is said to have broken inversion symmetry.

A similar behavior is observed in a paramagnet-to-ferromagnet phase transition. In the paramagnetic phase (above  $T_c$ ), the atomic magnetic moments

(spins) are randomly oriented and the total magnetization is zero. However, below  $T_c$  the strong interactions among the spins overcome thermal fluctuations leading to the formation of a ferromagnetic order. Here, all magnetic moments point in the same direction resulting in a macroscopic magnetization  $M$  (Fig. 1.1B, right). The system now lacks time-reversal symmetry.

A phenomenological description of spontaneous symmetry-breaking transitions was developed by Lev Landau [69]. He introduced the idea of an *order parameter* of the phase transition which quantifies the degree of “order” in the system. The order parameter is zero in the high-symmetry phase while it is non-zero in the broken-symmetry one. The magnetization  $M$  and the polarization  $P$  are order parameters of the ferromagnetic and ferroelectric phase transitions, respectively. Landau proved that by expanding the free energy of the system as a power series in the order parameter, many important features of the transition could be reproduced. Indeed, while not every phase transition belongs to the Landau paradigm of order parameters and spontaneous symmetry breaking<sup>1</sup>, many important phenomena such as ferroelectricity, ferromagnetism and superconductivity could be phenomenologically described using the same formalism. The power of Landau’s approach is to capture the relevant phenomenology of a multitude of phase transitions independently on the nature of the microscopic interactions that drive them.

The ability to control broken-symmetry phases and their order parameters is of fundamental importance for most technologically relevant applications. For example, polarization and magnetization switching can be used to store information in memories or make logical operations in transistors. In an ideal scenario, one would be able to activate a desirable property in an otherwise common material, use it for as long as needed and then revert the material to its original phase. Such degree of control relies necessarily on the ability to modify a material symmetry at will. It is the goal of this thesis to explore

---

<sup>1</sup> For example, topological phase transitions.

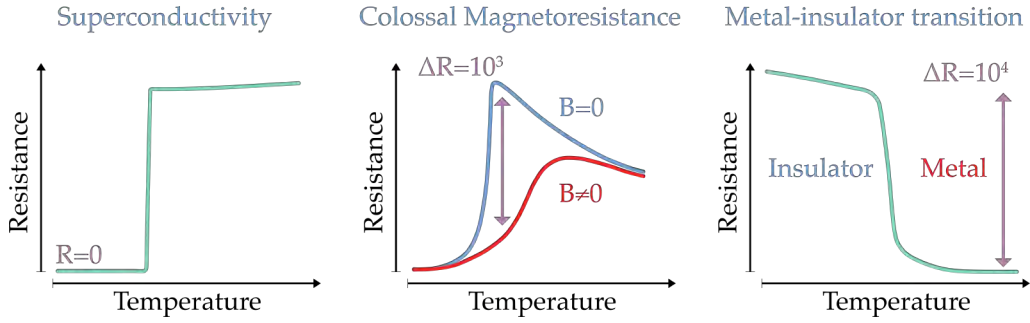


Figure 1.2: Giant collective responses in quantum materials. Left panel: At  $T_c$  the resistance of a superconductor becomes identically zero (adapted from [87]). Center panel: In a magnetoresistive material the application of an external magnetic field can change the resistance by several order of magnitude (adapted from [20]). Right panel: In an insulator-to-metal transition a colossal change in resistance occurs at  $T_c$  (adapted from [137]).

in what way and to what extent it is possible to manipulate or even induce a broken-symmetry phase.

**QUANTUM MATERIALS** Ideal candidates for the purpose are materials naturally sensitive to external perturbations, such as *quantum materials* [58, 116]. In this special class of solids, quantum mechanical effects survive over a wide range of temperatures and length scales resulting in some of the most fascinating phenomena in condensed matter physics such as superconductivity [57], colossal magnetoresistance [101] and Mott transitions [46] (Fig. 1.2). These remarkable properties originate from strong interactions among various degrees of freedom that bring these materials on the edge of stability among different, often entangled phases.

A useful example of this behavior consists of the series of transition-metal perovskites  $SrVO_3$ ,  $CaVO_3$ ,  $LaTiO_3$  and  $YTiO_3$  (Fig. 1.3). All these compounds owe their electronic properties to a single  $d$  electron per transition-metal ion and exhibit very similar electronic correlations<sup>2</sup>. However, despite these similarities, across the series the transition-metal electron becomes increasingly localized until it undergoes a Mott transition. While  $SrVO_3$  and  $CaVO_3$  are correlated

<sup>2</sup> They exhibit similar on-site Coulomb repulsion.

metals,  $\text{LaTiO}_3$  and  $\text{YTiO}_3$  are Mott insulators with energy gaps of  $0.2 \text{ eV}$  and  $1 \text{ eV}$ , respectively. The origin of this phenomenon lies in the progressing structural distortion which tilts and rotates the corner-sharing oxygen octahedra that enclose the transition-metal ions (Fig. 1.3). Stronger distortions make it harder for the electrons to hop from one transition-metal site to the other favoring an insulating state<sup>3</sup>. This example highlights the paramount role of structural deformations in controlling the electronic properties of solids. More importantly, it shows how in quantum materials, owing to the strong interplay among different degrees of freedom, small perturbations can result in substantial changes of the macroscopic properties. It is the delicate balance between competing and coexisting ground states that renders quantum materials particularly sensitive to external stimuli. Given the appropriate control parameter, their functionalities can be extensively tuned, leading to the formation of intricate phase diagrams where a multitude of electronic, magnetic and structural phases can be stabilized (Fig. 1.4). Conventionally, phase control of quantum materials is achieved statically, for example by synthesis and chemical substitution or by the application of stress, electric and magnetic fields. A fundamentally different approach consists in looking for order away from equilibrium. Dynamical driving of quantum systems with light fields has become an established route to material control [4].

**ENERGY SCALES AND NONLINEAR RESPONSE** To achieve strong modulation amplitudes, the enhanced light-matter coupling in the proximity of resonances is often exploited (Fig. 1.5). While direct excitation of electronic transitions at visible wavelengths has been shown capable of inducing phase transitions, the use of high energy ( $\sim \text{eV}$ ) photons restricts the control possibilities. Above-gap excitation inevitably heats up the electronic system, resulting in strongly incoherent dynamics. In the particular case of quantum materials, such high photon energies often lead to melting of the underlying low-energy

<sup>3</sup> Electron transport occurs through hybridization between Oxygen  $p$ -orbitals and transition-metal  $d$ -orbitals. Structural distortions reduce the orbital overlap and degeneracy (see [95]).

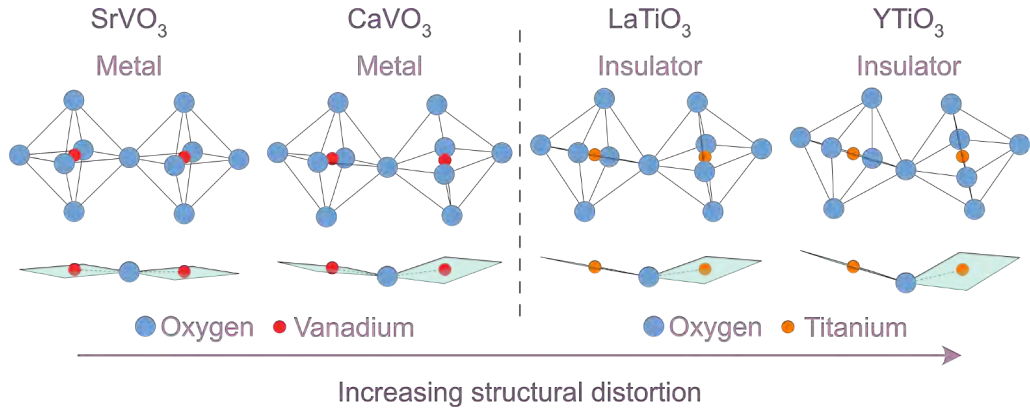


Figure 1.3: Crystal structures of  $\text{SrVO}_3$ ,  $\text{CaVO}_3$ ,  $\text{LaTiO}_3$  and  $\text{YTiO}_3$ . For clarity, part of the unit cell and the  $\text{Sr}$ ,  $\text{Ca}$ ,  $\text{La}$  and  $\text{Y}$  ions are not shown. The blue spheres represent the oxygen ( $\text{O}$ ) ions while the red and orange spheres represent the transition metal ( $\text{TM}$ ) ions. The bottom part highlights the  $\text{TM} - \text{O} - \text{TM}$  bond and how it is affected by the deformation. The arrow indicates the direction of increasing structural distortion which also corresponds to a growing electronic localization. The image is adapted from [95].

phenomena. An alternative approach consists in driving materials at the natural energy scales of their collective excitations [55, 88] (1-100s meV, Fig. 1.5). The development of laser sources capable of generating intense light pulses in the mid-infrared and terahertz frequency range has made it possible to resonantly and selectively drive collective degrees of freedom such as lattice vibrations [32] (phonons), superconducting gaps [5] and spin-waves [56] (magnons). In this excitation regime, the coherent coupling to collective modes minimizes heating and dissipation, thus allowing for the emergence of novel low-energy effects. In particular, nonequilibrium excitation of phonons with strong electromagnetic terahertz fields has proven to be an extremely efficient route towards phase control. Recent successful examples include ultrafast insulator-to-metal transitions [19, 103] or light-induced superconductivity [14, 26, 44, 54, 82].

The origin of this powerful technique lies in the nonlinear nature of the crystal lattice. When a material is subjected to extreme electromagnetic fields a multitude of nonlinear phenomena can be observed, such as high-harmonic generation [43], phonon amplification [15] or inelastic (Raman) scattering [32].

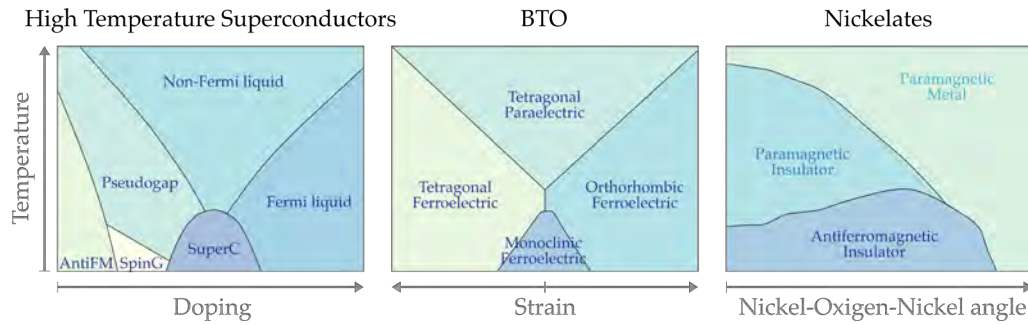


Figure 1.4: Phase diagrams of quantum materials. Left panel: prototypical phase diagram of high-temperature superconductors (adapted from [22]). Center panel: calculated phase diagram of  $BaTiO_3$  as a function epitaxial stress (adapted from [108]). Right panel: phase diagram of rare-earth nickelates ( $RNiO_3$ ) as a function of  $Ni-O-Ni$  angle controlled by changing the rare earth  $R$  (adapted from [18]).

For example, a phonon driven to large amplitudes can couple to other degrees of freedom that would be otherwise inaccessible in linear response, such as Raman phonons. This nonlinear phonon–phonon coupling results in a transient, selective and directional distortion of the crystal structure [33, 76]. Such phenomenon can be of extreme importance in quantum materials, where the macroscopic properties are closely linked to the atomic arrangement [113] (see also Fig. 1.3).

**STRUCTURE OF THE THESIS** It is the goal of this thesis to explore how ultrafast phonon excitation can be used to control or induce functional properties in complex oxides. Chapter 2 introduces the properties of infrared-active phonons both in the linear and nonlinear regime. I then highlight how lattice nonlinearities allow to achieve ultrafast structural control of complex materials. At the end of the Chapter, an example of electronic phase control through nonlinear phononics is presented. Chapter 3 introduces the properties of the quantum paraelectric  $SrTiO_3$ . I then show how nonlinear excitation of lattice vibrations with mid-infrared pulses can break inversion symmetry and induce a metastable ferroelectric state which persists for hours after the optical pump is interrupted. The optical and electrical measurements used to detect the phase transition are

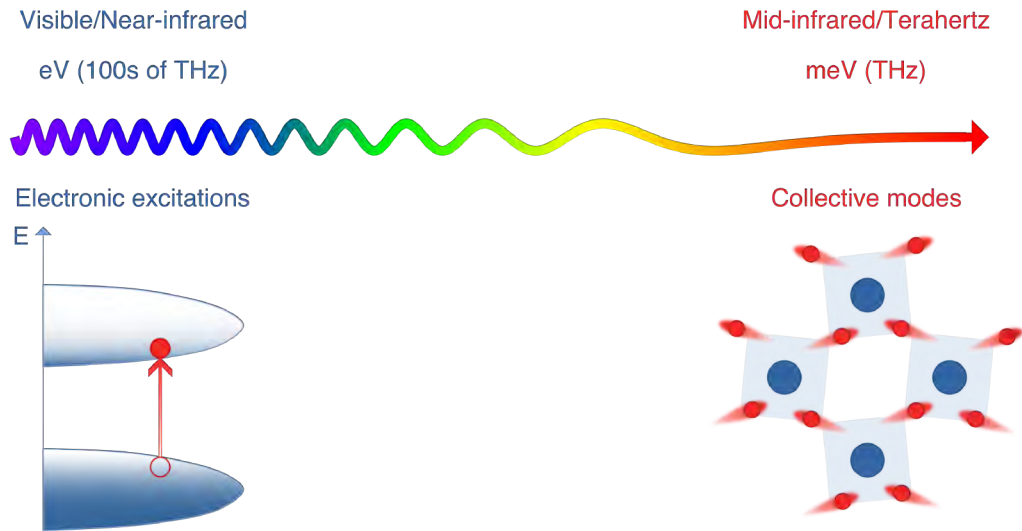


Figure 1.5: Energy scales. Electronic excitations in insulators lie in the electronvolt (eV) energy range. However, collective modes in quantum materials have typical energies of the order of few tens of millielectronvolt (meV). Image adapted from [88].

described in detail. At the end of the Chapter, I show how spatially resolved measurements suggest that a novel phono-flexoelectric coupling is responsible for the observed effect. Chapter 4 discusses how nonlinear phononics can be used to control the magnetization of a canted ferromagnet. Coherent mixing of non-degenerate orthogonal modes results in circularly polarized phonons which mimic the application of a magnetic field and triggers the excitation of a coherent spin wave. The experimental results are compared to simulations obtained solving numerically Maxwell and Landau-Lifshitz equations.

In appendix A, I describe how strong mid-infrared fields can also be used to amplify optical phonons. Details on the experimental setups can be found in appendix B.

# 2

---

## NONLINEAR LATTICE CONTROL

---

The resonant excitation of infrared-active phonons with ultrashort and intense pulses of light has proven to be an efficient route to material control [31, 74]. The origin of this powerful tool lies in the nonlinear nature of the crystal lattice. A phonon driven to large amplitudes can transfer energy to other lower-frequency vibrational modes. This nonlinear phonon–phonon coupling results in a transient, directional and selective distortion of the crystal structure, i.e. specific atoms of the lattice move temporarily to different positions. Because this coherent light-lattice coupling minimizes dissipation, such tailored displacements are especially relevant in quantum materials where transient structures could favor the formation of new, low-energy quantum phases.

In this Chapter, the properties of driven lattice vibrations both in the linear and nonlinear regimes are discussed. The first section describes the linear light-phonon interaction, reporting the equations governing the lattice dynamics and the resulting optical properties. The second section discusses the nonlinear lattice response to intense light fields and the related structural control capabilities. The theoretical framework developed in this Chapter serves as the foundation for the nonlinear phonon effects studied experimentally in this thesis.

## 2.1 PHONONS IN INSULATORS - LINEAR RESPONSE

In linear response, the interaction of light with an infrared-active optical phonon can be modeled as a charged harmonic oscillator driven by the oscillating electric field of light (Lorentz model).

2.1.1 *Infrared-active phonons: charged harmonic oscillators*

A phonon consists of the collective motion of ions along a specific eigenvector (2.1A). In the context of optical spectroscopy, which accesses only a small, long-wavelength region of the Brillouin zone where the momentum  $k \sim 0$ , the atoms can be considered to move synchronously throughout the entire solid. In the harmonic approximation, valid for small displacements  $Q_{IR}$ , the energy potential felt by the ions (2.1B) is described by the parabolic equation:

$$U_{harm} = \frac{1}{2} \omega_{TO}^2 Q_{IR}^2 \quad (2.1)$$

where  $\omega_{TO}$  is the phonon frequency. When the ions are displaced from their equilibrium position, they experience a restoring force proportional to the displacement given by

$$F_{harm} = -\frac{\partial U_{harm}}{\partial Q_{IR}} = -\omega_{TO}^2 Q_{IR} \quad (2.2)$$

which causes the atoms to oscillate at the resonance frequency  $\omega_{TO}$ , as described by the equation of motion

$$\frac{\partial^2 Q_{IR}}{\partial t^2} = F_{harm} = -\omega_{TO}^2 Q_{IR} \quad (2.3)$$

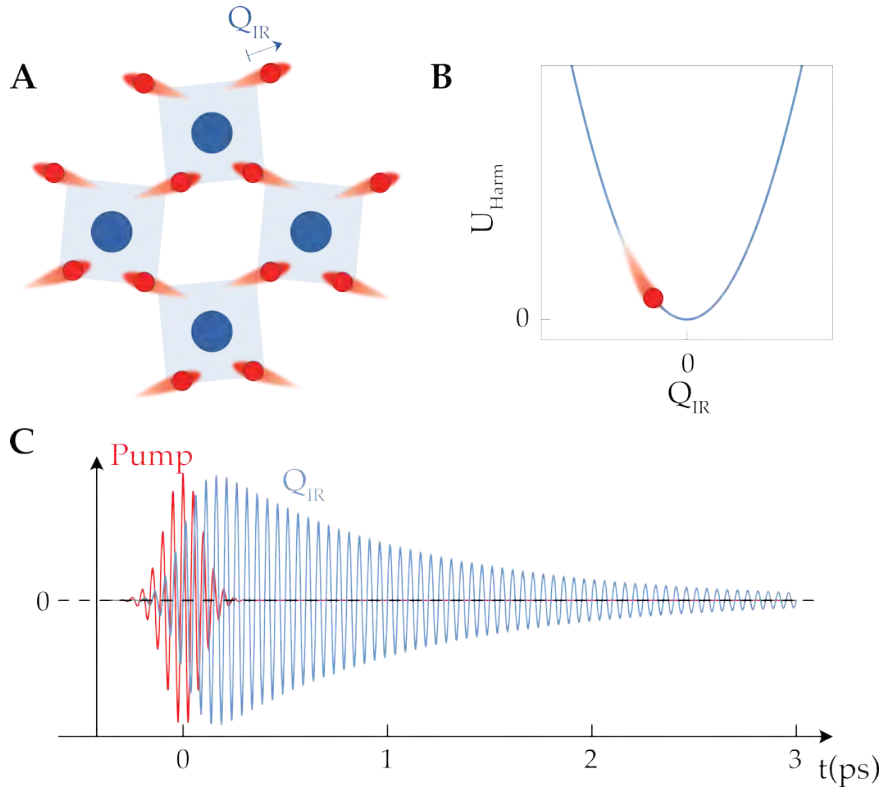


Figure 2.1: Infrared active phonon | Linear response. *A*: mode eigenvector in an insulating oxide. The high-frequency modes in oxides are mostly characterized by the motion of the lighter ions (oxygen).  $Q_{IR}$  is the phonon coordinate. *B*: harmonic potential. *C*: simulated time-dependence of the displacement vector of a coherently driven phonon (blue). The driving field (red) is 150 femtoseconds long while the phonon decay constant is 500 femtoseconds.

**DRIVEN PHONONS** Phonons that possess a dipole, so-called infrared-active, can directly couple to the electric field of light. The driving field  $E$  can be incorporated into Eq. 2.3:

$$\frac{\partial^2 Q_{IR}}{\partial t^2} + \omega_{TO}^2 Q_{IR} = \frac{Z^*}{\mu} E \quad (2.4)$$

where  $Z^*$  is the Born effective charge<sup>1</sup> associated with the phonon dipole and  $\mu$  is the effective mass of the oscillator.

<sup>1</sup> For small displacements, the effective charge defined as  $Z = \frac{\partial P_{IR}}{\partial Q_{IR}}$ , where  $P_{IR}$  is the phonon polarization, can be approximated by a constant. In Appendix A, the nonlinear regime in which this approximation is no longer valid is discussed.

Equation 2.4 describes the motion of an undamped oscillator driven by a force proportional to  $E$ . Such oscillator, once set in motion, would perpetually oscillate. This unphysical scenario is due to the harmonic approximation, which assumes that the ions are moving in a parabolic potential (2.1B), i.e. their restoring force is linearly proportional to the displacement. In real solids, anharmonicities of the lattice potential allow for the energy transfer among different modes and result in a finite lifetime of the phonon oscillations. These effects can be introduced here via a phenomenological damping term, which leads to a new equation of motion of the form

$$\frac{\partial^2 Q_{IR}}{\partial t^2} + \Gamma \frac{\partial Q_{IR}}{\partial t} + \omega_{TO}^2 Q_{IR} = \frac{Z^*}{\mu} E \quad (2.5)$$

where the damping  $\Gamma$  is inversely proportional to the lifetime of the phonon mode. A time-dependent monochromatic electromagnetic field can be written as:

$$E(t) = E_0 e^{-i\omega t} \quad (2.6)$$

where the complex parameter  $E_0$  accounts for additional phase terms. For a driver oscillating at frequency  $\omega$ ,  $Q_{IR}$  takes solutions of the form

$$Q_{IR}(t) = Q_{IR,0} e^{-i\omega t} \quad (2.7)$$

where  $Q_{IR,0}$  is the amplitude of the phonon oscillations. The phonon response to the field is therefore calculated by combining Eq. 2.6 and 2.7 with Eq.2.5:

$$Q_{IR}(t) = \frac{Z^*/\mu}{\omega_{TO}^2 - \omega^2 - i\Gamma\omega} E_0 e^{-i\omega t} \quad (2.8)$$

It is clear from Eq. 2.8 that the phonon amplitude  $Q_{IR}$  is maximized for driving frequencies  $\omega$  approaching  $\omega_{TO}$ . That is, in order to achieve the highest modulation amplitudes, the resonance condition must be satisfied.

LORENTZ MODEL The polarization of a macroscopic sample due to a single charged oscillator can be defined as:

$$P_{phonon}(t) = NZ^*Q_{IR}(t) \quad (2.9)$$

where  $N$  is the number of unit cells per unit volume. Taking into account eq. 2.8, the phonon polarization becomes:

$$P_{phonon}(t) = \frac{N(Z^*)^2}{\mu} \frac{1}{\omega_{TO}^2 - \omega^2 - i\Gamma\omega} E_0 e^{-i\omega t} \quad (2.10)$$

This is the polarization generated by an infrared-active phonon in response to a monochromatic electromagnetic wave.

The dielectric function of any insulator quantifies the reorganization of charges to an applied electric field  $E$ . In a linear and homogenous material,  $\epsilon$  defines the proportionality between  $E$  and the electric displacement field  $D$ :

$$D = \epsilon_0 \epsilon(\omega) E \quad (2.11)$$

By combining eq. 2.11 and the constitutive equation of the material:

$$D = \epsilon_0 E + P_{phonon} \quad (2.12)$$

we can obtain an expression for the dielectric function  $\epsilon$  in the presence of an infrared-active phonon:

$$\epsilon(\omega) = 1 + \frac{P_{phonon}}{\epsilon_0 E} \quad (2.13)$$

By substituting eq. 2.10 into eq. 2.13 we obtain:

$$\epsilon(\omega) = 1 + \frac{\omega_{plasma}^2}{\omega_{TO}^2 - \omega^2 - i\Gamma\omega} \quad (2.14)$$

where  $\omega_{plasma} = \sqrt{\frac{N(Z^*)^2}{\epsilon_0 \mu}}$  is defined as the plasma frequency of the phonon. Eq. 2.14 only considers the ionic contribution to the permittivity. However, the total dielectric behavior of a material consists also of other contributions, in particular those arising from the electrons' response to the applied electric field even when off-resonant. To take into account the effect of higher-energy electronic resonances, a constant background given by  $\epsilon_\infty$  can be added:

$$\epsilon(\omega) = \epsilon_\infty + \frac{\omega_{plasma}^2}{\omega_{TO}^2 - \omega^2 - i\Gamma\omega} \quad (2.15)$$

Eq. 2.15 constitutes the Lorentz model which successfully describes the linear interaction between a dielectric material and an electromagnetic field.

**LYDDANE-SACHS-TELLER RELATION** For simplicity, we consider a material with negligible damping ( $\Gamma \sim 0$ ). By imposing  $\epsilon(0) = \epsilon_0$ , from Eq.2.15 we obtain:  $\omega_{plasma}^2 = \omega_{TO}^2 (\epsilon_0 - \epsilon_\infty)$ . We can therefore rewrite Eq.2.15 as:

$$\epsilon(\omega) = \epsilon_\infty + \frac{(\epsilon_0 - \epsilon_\infty)}{1 - \frac{\omega^2}{\omega_{TO}^2}} \quad (2.16)$$

The condition for which the dielectric function becomes zero ( $\epsilon(\omega_{LO}) = 0$ ) is:

$$\omega_{LO}^2 = \omega_{TO}^2 \frac{\epsilon_0}{\epsilon_\infty} \quad (2.17)$$

where  $\omega_{LO}$  is defined as the longitudinal optical (LO) phonon frequency. The origin of this name is readily understood when considering Gauss' law in absence of free charges, that is:

$$\nabla \cdot \vec{D} = 0 \quad (2.18)$$

For a monochromatic plane-wave  $\vec{E}(\vec{r}, t) = E_0 e^{i(\vec{k} \cdot \vec{r} - \omega t)}$ , Eq. 2.18 becomes:

$$\epsilon_0 \epsilon(\omega) (\vec{k} \cdot \vec{E}) = 0 \quad (2.19)$$

which has two solutions. The first one,  $(\vec{k} \cdot \vec{E}) = 0$ , implies that the electric field  $\vec{E}$  must be perpendicular to the propagation direction (the electromagnetic field is transverse). However, the material also allows for longitudinal fields, that is  $(\vec{k} \cdot \vec{E}) \neq 0$ , provided that  $\epsilon(\omega) = 0$ . This condition is satisfied only at  $\omega_{LO}$  (see Eq. 2.17). It is however important to note that the electromagnetic field of light, which is transverse, can only couple to the transverse phonon.

Eq.2.17 is referred to as the Lyddane-Sachs-Teller relation and provides an important connection between the long-wavelength dynamical behavior of insulators ( $\omega_{TO}$  and  $\omega_{LO}$ ) and their dielectric properties ( $\epsilon_0$  and  $\epsilon_\infty$ ). In particular, this relationship can be used to describe the dielectric behavior of displacive ferroelectrics across a paraelectric-to-ferroelectric phase transition (for more details see Chapter 3). At the critical temperature, a phonon-instability brings  $\omega_{TO}$  to zero frequency, resulting in a divergence of  $\epsilon_0$  ( $\epsilon_0 \propto \frac{1}{\omega_{TO}^2} \xrightarrow{\omega_{TO} \rightarrow 0} \infty$ ).

### 2.1.2 Light-phonon interaction: phonon-polariton formation and optical response

The Lorentz model, presented above, describes the response of a charged harmonic oscillator to a resonant electromagnetic field. However, this model neglects all propagation effects<sup>2</sup> and, most importantly, it ignores the interaction between the driving field  $E$  and the field generated by the induced phononic polarization  $P_{phonon}$ . In particular, on resonance, the light-phonon interaction is so strong that the system cannot be described any longer as a simple superposition of its constituents. When the flat dispersion relation of the optical phonon ( $\omega = \omega_{TO}$ ) crosses that of light ( $\omega = \frac{c}{\sqrt{\epsilon}}k$ ) a new, mixed light-matter quasiparticle forms and the dispersion relations are strongly modified (Fig. 2.2). This hybrid state is known as a *phonon-polariton*. A complete description of

<sup>2</sup> The momentum of light is never considered.

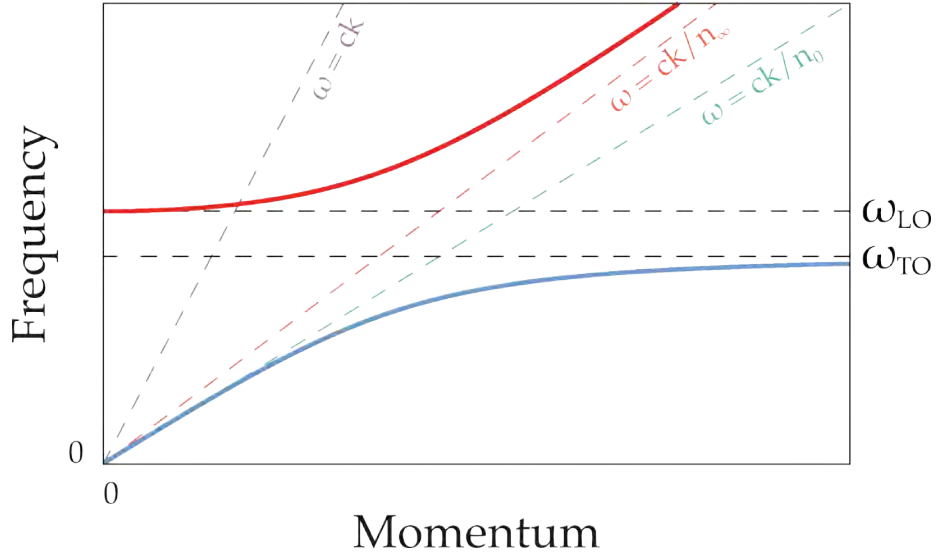


Figure 2.2: Phonon-polariton dispersion. The strong light-matter coupling in the proximity of a phononic resonance results in the formation of hybrid states called phonon-polaritons. Blue: lower polariton branch. Red: upper polariton branch. Between  $\omega_{TO}$  and  $\omega_{LO}$  there are no available states, i.e. light cannot propagate into the crystal.

the phenomenon requires the solution of the wave equation which in a non magnetic material and in the absence of free charges, takes the form:

$$\nabla \cdot \vec{E} = \frac{\epsilon}{c^2} \frac{\partial^2 \vec{E}}{\partial t^2} \quad (2.20)$$

For tranverse, monocromatic plane-waves  $\vec{E}(\vec{r}, t) = E_0 e^{i(\vec{k} \cdot \vec{r} - \omega t)}$ , Eq. 2.20 becomes:

$$k^2 = \frac{\epsilon}{c^2} \omega^2 \quad (2.21)$$

which represents the dispersion relation of light in a material with dielectric constant  $\epsilon$ . The phonon-polariton dispersion relation can be obtained by inserting Eq.2.16 and Eq.2.17 into Eq. 2.21:

$$\omega = \sqrt{\frac{(\omega_{LO}^2 \epsilon_\infty + c^2 k^2) \pm \sqrt{(\omega_{LO}^2 \epsilon_\infty + c^2 k^2)^2 - 4 \epsilon_\infty c^2 k^2 \omega_{TO}^2}}{2 \epsilon_\infty}} \quad (2.22)$$

Note that for a given  $k$  there are two possible values of  $\omega$  (Fig. 2.2). These two solutions are referred to as polariton branches and arise from the level anticrossing between the light and the phonon modes (they “repel” each other). This phenomenon originates from the interplay between the light field that sets the charges in motion and the field generated by the oscillating charges. These fields cannot be separated and the resulting dispersion will be strongly affected by their relative amplitudes and phases.

As  $k \rightarrow 0$ , the upper branch tends to  $\omega_{LO}$  behaving more like a phonon (flat band). On the other hand, the lower branch behaves like light in vacuum with a dispersion proportional to the momentum,  $\omega = k \frac{c}{\sqrt{\epsilon_0}}$ . For  $k \rightarrow \infty$ , the behavior is completely reversed: the upper branch displays a light-like behavior with a dispersion  $\omega = k \frac{c}{\sqrt{\epsilon_\infty}}$ , while the lower branch has a phonon-like character with  $\omega = \omega_{TO}$ . For intermediate values of  $k$ , both branches display a mixed light-phonon character with a rapidly changing dispersion. In the spectral region between  $\omega_{LO}$  and  $\omega_{TO}$ , called *Reststrahlen band*, there are no available states, that is, light is not allowed to propagate in the material. Indeed, the photons in this frequency range will be reflected.

**OPTICAL PROPERTIES** The strong light-matter coupling in the proximity of the phonon resonance has important consequences on the optical properties of the material. The dielectric function (real and imaginary) and the reflectivity are shown in Fig. 2.3. The real part of the permittivity  $\epsilon_1$ , is constant at low frequencies while it is maximized at the resonance  $\omega_{TO}$ . This reflects the fact that when the driver approaches the phonon eigenfrequency, the amplitude  $Q_{IR}$  increases. For frequencies between  $\omega_{TO}$  and  $\omega_{LO}$ ,  $\epsilon_1$  is negative, that is the phonon oscillates out of phase with respect to the driver resulting in the complete screening of the impinging electric field (high reflectivity). As already mentioned,  $\epsilon_1$  crosses zero at the longitudinal frequency  $\omega_{LO}$ . The imaginary

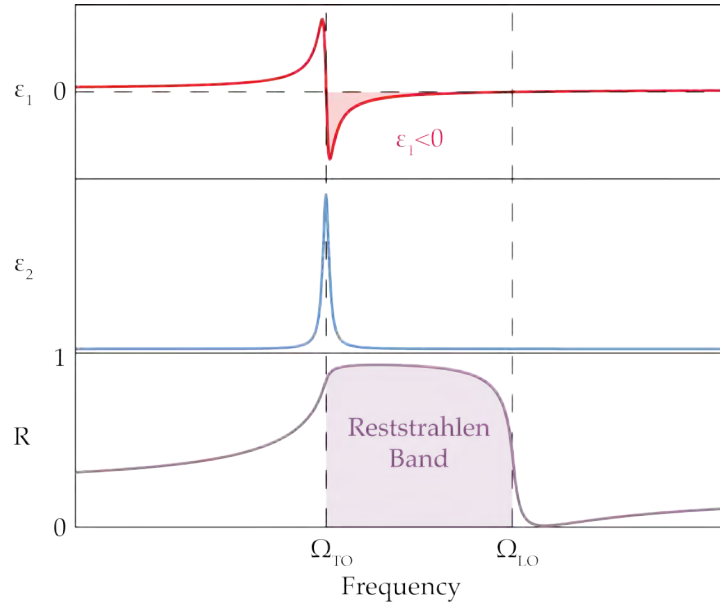


Figure 2.3: Optical properties of an infrared-active phonon in an insulator. Top: real part of the dielectric function. Middle: imaginary part of the dielectric function. Bottom: reflectivity.

part of the permittivity  $\epsilon_2$ , which is a measure of the dissipation, peaks at  $\omega_{TO}$ . The width of the peak is given by the damping parameter  $\Gamma_{IR}$ .

For frequencies below  $\omega_{TO}$ , the reflectivity is only slightly reshaped and tends to a constant value determined by  $\epsilon_0$ . In the Reststrahlen band, the reflectivity approaches unity. For frequencies slightly higher than  $\omega_{LO}$ ,  $\epsilon_1$  becomes one and the refractive index of the material matches that of air resulting in a vanishing reflectivity.

## 2.2 NONLINEAR PHONONICS

In section 2.1, we described the linear response of a phonon to a monochromatic light field. However, in real experiments optical phonons are driven by ultrashort

laser pulses. In this case, the constant field amplitude  $E_0$  in Eq. 2.6 becomes a time-dependent function  $E_0(t)$ :

$$E(t) = E_0(t) e^{-i\omega t} \quad (2.23)$$

where  $E_0(t) = e^{-\left[4\ln(2)\frac{t^2}{\tau^2}\right]}$  is the Gaussian pulse envelope of time duration  $\tau^3$ . Fig. 2.1C shows the linear response of an infrared-active phonon as defined by Eq. 2.5 to a 150 femtosecond long ultrashort optical pulse. The ions oscillate about their equilibrium position and after the driving field is removed, the phonon amplitude decays exponentially with  $\frac{1}{\Gamma}$ .

The main advantage in using ultrashort pulses is that enormous electric fields can be generated and phonons can be driven to large amplitudes. Indeed, the peak electric field amplitude scales with:

$$E_{peak} = \sqrt{\frac{2F}{\epsilon_0 c \tau}} \quad (2.24)$$

where  $F$  is the energy per unit area, or fluence, and  $c$  is the speed of light. Eq. 2.24 implies that, for a given energy per pulse, shorter pulses equate to higher fields.

Importantly, for strong driving electric fields the phonon dynamics becomes highly nonlinear and anharmonic contributions must be taken into account. In this section, I will first describe the theory of nonlinear phononics. I will then illustrate how lattice anharmonicities can be used to control the macroscopic phase of complex materials.

---

<sup>3</sup> Here the time duration is defined as the full width at half maximum, that is, the difference between the two points in time at which the electric field is equal to half of its maximum value.

### 2.2.1 Lattice anharmonicities and ionic Raman scattering

With the availability of strong mid-infrared light sources (peak fields in excess of  $10 \frac{MV}{cm}$ ), displacements of the order of several percents of the interatomic distances, corresponding to multiple picometers, can be achieved. In this regime, the restoring force felt by the ions is no longer linearly proportional to the displacement and the harmonic approximation defined by Eq.2.1 fails to reproduce the vibrational dynamics. The nonlinear lattice response can be described by expanding the energy potential Eq.2.1:

$$U_{NL} = \frac{1}{2}\omega_{TO}^2 Q_{IR}^2 + \alpha_1 Q_{IR}^3 + \alpha_2 Q_{IR}^4 + \dots + \phi_1 Q_{IR}^3 E + \phi_2 Q_{IR}^2 E^2 \dots \quad (2.25)$$

Higher order terms in  $Q_{IR}$  are responsible for the ionic equivalent of well known strong-field phenomena such as ionic high harmonic generation [43], identified by the pure terms in  $Q_{IR}$  multiplied by the coefficients  $\alpha_i$ , and phonon amplification [15], allowed by the mixed terms multiplied by the coefficients  $\phi_i$  (see Appendix A). Here,  $E$  is the driving electric field.

Lattice anharmonicities also allow for coherent coupling among different phonons [32, 78, 80, 125] (Fig. 2.4). For example, the driven infrared phonon can couple with and excite another vibrational mode  $Q_R$ . This inelastic scattering process can be described by the anharmonic potential:

$$U_{NL} = \frac{1}{2}\omega_{TO}^2 Q_{IR}^2 + \frac{1}{2}\omega_R^2 Q_R^2 - \beta Q_{IR}^2 Q_R \quad (2.26)$$

where  $\omega_R$  is the natural frequency of the coupled mode and  $\beta$  is a material-specific coupling coefficient. By symmetry, in centrosymmetric materials the nonlinearly coupled mode  $Q_R$  must be Raman-active. These modes do not possess a dipole moment and in linear response cannot couple to light (Fig. 2.5A shows an example of a Raman phonon motion). The phonon-phonon interaction described by 2.26 is the ionic equivalent of electronic Raman scattering. The driven mid-infrared phononic field loses some of its energy to a Raman phonon

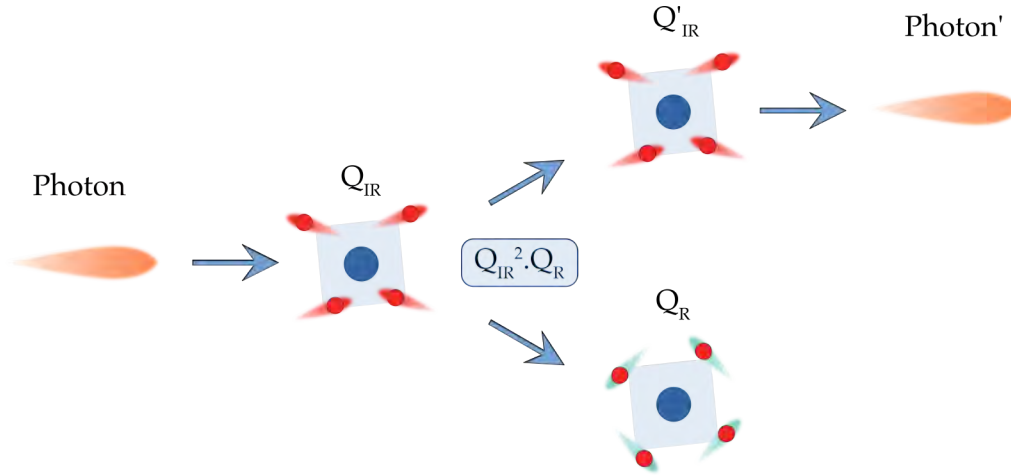


Figure 2.4: Impulsive stimulated Ionic Raman Scattering. A terahertz photon drives coherently an infrared-active phonon. Due to anharmonicities of the crystal lattice, the generated phononic field excites inelastically a Raman phonon. This process also renormalizes the frequency of the infrared-active phonon and of the reemitted terahertz photon. In the figure, the frequency change is indicated by the apostrophe.

which is excited (Stokes process). At the same time, also the frequency of the infrared phonon is renormalized due to the nonlinear interaction (Fig. 2.4). Note that the ionic contribution to the Raman cross-section is significant only for light frequencies resonant with the infrared-active phonon, that is, where the amplitude  $Q_{IR}$  is large.

**NONLINEAR DYNAMICS AND STRUCTURAL CONTROL** The cubic anharmonicity considered in Eq. 2.26 significantly modifies the energy landscape of the coupled Raman phonon. Indeed, for finite amplitudes of the infrared mode  $Q_{IR}$ , the potential felt by the ions along the coordinate  $Q_R$  becomes:  $U_R = \frac{1}{2}\omega_R^2 Q_R^2 - \beta Q_{IR}^2 Q_R$ . The energy minimum is now found for  $Q_R = \frac{\beta Q_{IR}^2}{\omega_R^2} \neq 0$ , shifted from the unperturbed equilibrium position (Fig. 2.5B). This means that due to cubic anharmonicities, the ions move towards a new equilibrium position along the Raman coordinate as long as the infrared-active mode is oscillating, thus forming a new, transient crystal structure.

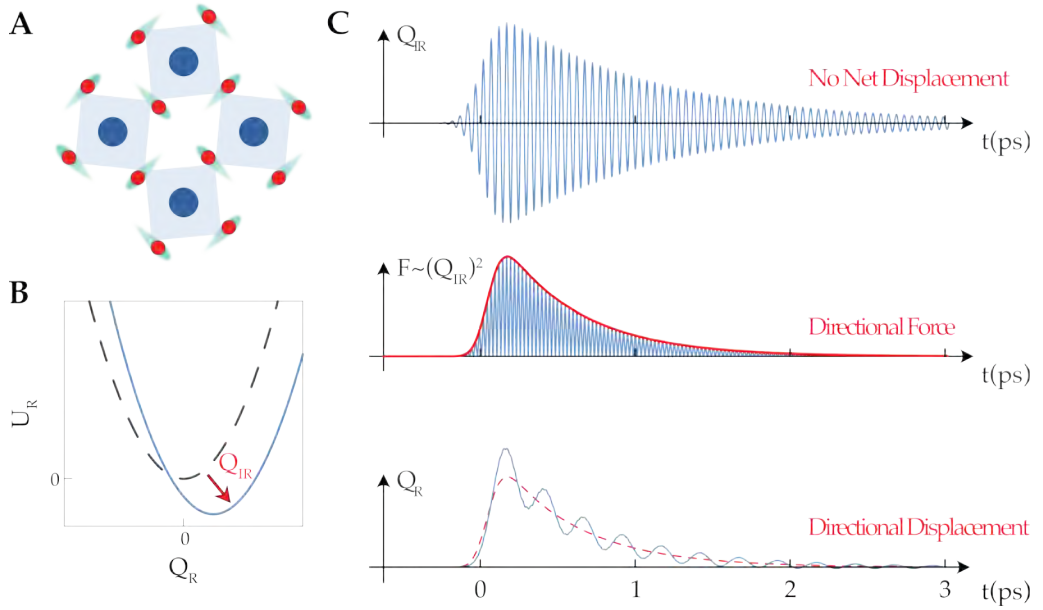


Figure 2.5: Nonlinear phononics. (A) representative Raman mode eigenvector in an insulating oxide. The mode does not possess a dipole. (B) harmonic potential for the Raman phonon. For finite amplitudes of the infrared phonon, the potential of the Raman mode is shifted towards a new equilibrium position. (C): Simulated nonlinear phonon dynamics. A 150 fs laser pulse drives resonantly a 20 THz infrared active phonons. The nonlinearly coupled Raman mode has a 4 THz resonance frequency. Top Panel: time-dependence of the displacement vector of a coherently driven phonon. Middle Panel: time-dependence of the force acting on the ions along the Raman coordinate. Bottom Panel: time evolution of the inelastically coupled Raman mode. Fig. B and C are inspired by [75].

The equation of motion that describes this phenomenon can be derived from Eq. 2.26. The force acting on the ions along  $Q_R$  is:  $F_R = -\frac{\partial U_{NL}}{\partial Q_R} = \beta Q_{IR}^2$ . The corresponding dynamical response is defined by:

$$\frac{\partial^2 Q_R}{\partial t^2} + \Gamma_R \frac{\partial Q_R}{\partial t} + \omega_R^2 Q_R = a Q_{IR}^2 \quad (2.27)$$

where  $\Gamma_R$  and  $\omega_R$  are the damping and the resonance frequency of the Raman mode, respectively. Upon excitation of the infrared-active mode, the ions oscillate about their equilibrium positions along the eigenvector  $Q_{IR}$  (Fig. 2.5C, top panel). On average, there is no net displacement. However, due to the proportionality of  $F_R$  to  $Q_{IR}^2$ , the Raman mode experiences a directional force modulated at  $2\omega_{IR}$ .

Since the natural frequency of the Raman mode is much lower than that of the infrared-active phonon, i.e.  $\omega_R \ll 2\omega_{IR}$ , the quickly oscillating components of  $F_R$  become negligible and the effective force felt by the coupled phonon is proportional to the envelope of the squared infrared coordinate (Fig. 2.5C middle). This rectified, directional force causes a transient displacement of the ions along  $Q_R$ . For example, when the infrared mode of Fig. 2.1A is combined with the deformation along the Raman coordinate of Fig. 2.5A, the structure of Fig. 2.6 develops where the rotation of the oxygen octahedra is modified as compared to the unperturbed lattice. This structural change may be slow or fast relative to the frequency of the coupled mode  $\omega_R$ . In particular, if the dispersive force rises promptly compared to the period of the Raman mode, coherent phonon oscillations can also be initiated (Fig. 2.5C bottom). Assuming that no transition to a metastable state takes place, the displaced structure survives as long as the infrared-active phonon oscillates.

It is important to mention that for the sake of clarity we considered a simplified case in which *one* infrared-active phonon couples to *one* Raman-active phonon. However, two important extensions should be considered. First, in real experiments the driven IR mode couples to many Raman phonons at once and the resulting transient structure is a combination of the ionic displacements along all of the coupled Raman mode eigenvectors [113]. Second, more than one infrared mode can be excited simultaneously<sup>4</sup> leading to important selection rules modifications [90, 100].

PHONON MIXING AND SELECTION RULES      The interaction Hamiltonian Eq.2.26 must be totally symmetric by all elements of the point group [100, 113]. As a consequence, the nonlinear coupling to a Raman phonon is allowed only when the product between the square of the irreducible representation of the infrared-active phonon  $\Gamma_{IR}$  and the irreducible representation of the Raman

<sup>4</sup> For example, in the case of two degenerate but orthogonal phonons, a simultaneous excitation would occur if the linear polarization of the driver lay in between the two modes.

mode  $\Gamma_R$  contains the totally symmetric irreducible representation, that is:  $[\Gamma_{IR} \times \Gamma_{IR}] \times \Gamma_R \supseteq A_{1g}$ . For non-degenerate infrared-active modes ( $A_u$  and  $B_u$ ) the cubic term  $U_{coupling} = -\beta Q_{IR}^2 Q_R$  only allows for coupling to  $A_{1g}$  symmetry Raman modes, which preserve the crystal symmetry. However, if the infrared-active mode is degenerate or if two infrared-active phonons are simultaneously excited, the coupling with Raman modes of other symmetries becomes possible. In general, the third-order coupling term can be rewritten as:

$$U_{coupling} = -\beta_{12} Q_{IR,1} Q_{IR,2} Q_R \quad (2.28)$$

where  $Q_{IR,1}$  and  $Q_{IR,2}$  are different infrared-active phonons,  $Q_R$  is the coupled Raman mode and  $\beta_{12}$  is the coupling coefficient. The importance of the generalized coupling Eq. 2.28 is twofold.

First, the coupling with a Raman mode of symmetry other than  $A_{1g}$  can result in a transient lattice deformation that changes the crystal symmetry[100]. In particular, in materials where inversion (or time-reversal) symmetry is already broken, nonlinear degenerate phononics can lead to the creation of a transient electrical polarization (or magnetization). It is however important to note that if inversion is an element of the crystal class or time reversal is an element of the magnetic point group, the coupling term described in Eq. 2.28 cannot break either of these symmetries<sup>5</sup>.

Second, when two infrared phonons are independently and simultaneously excited their relative phases can differ, while in the case of a single driven mode,  $Q_{IR}^2$ , the phase difference is always zero. In particular, when the two driven phonons are orthogonal and with the appropriate relative phases, circularly polarized phononic fields can be generated. Under these conditions, phonons can directly couple to the magnetization of a material [90] and not only to Raman phonons<sup>6</sup>.

<sup>5</sup> Different nonlinear couplings are needed to achieve light-induced inversion symmetry breaking in centrosymmetric materials, as discussed in In Chapter 3.

<sup>6</sup> For a more detailed discussion see Chapter 4

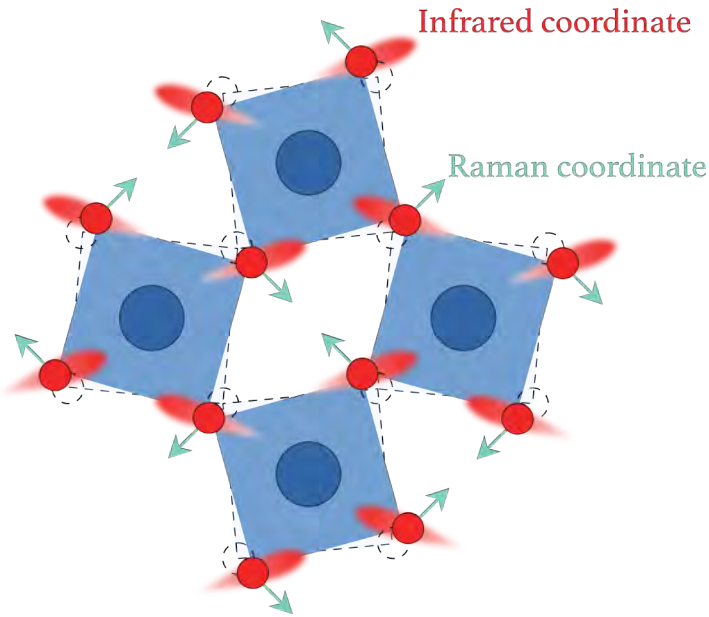


Figure 2.6: A new, transient structure. As long as the driven infrared phonon is oscillating, the ions move along the Raman coordinate to create a new crystal structure.

### 2.2.2 Transient structural control of correlated phases

The nonlinear coupling between an infrared-active phonon driven to large amplitude and a Raman mode can lead to transient structural modifications. The nonlinearly driven structural distortions were experimentally observed with time-resolved X-ray diffraction in different transition metal oxides [34, 77]. Changes of the order of few picometers can be routinely achieved. Such displacements can be extremely relevant in strongly correlated materials where the macroscopic properties arise from the delicate balance among different degrees of freedom. Small structural deformations can lead to dramatic modifications of the material's properties. The first example of such phonon-driven phase control was achieved in a strongly correlated manganite ( $AMnO_3$  family).

In these materials, the collective electronic properties are mostly affected by the manganese (3d) orbitals occupation and by crystal lattice distortions. In particular, the overlap between the manganese  $e_g$  and oxygen  $p$  orbitals decreases

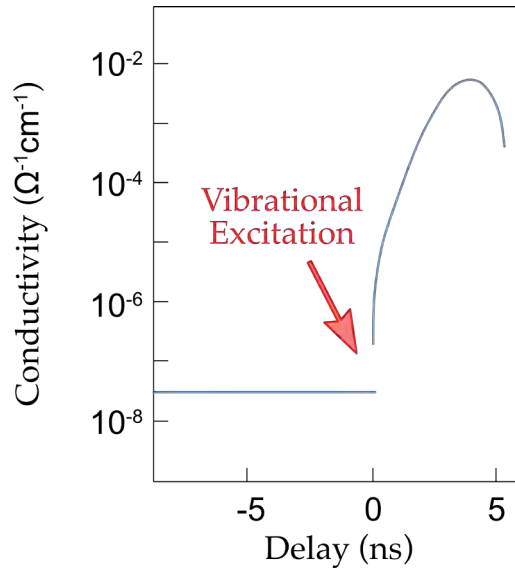


Figure 2.7: Metal-insulator transition in a manganite. Upon vibrational excitation, the conductivity of *PCMO* changed by several orders of magnitude, confirming the transition to a metallic state (adapted from [103]).

for increasing distortions of the  $Mn - O - Mn$  angle. Therefore, rotational deformations of the oxygen octahedra make it harder for the electrons to hop from one site to the other, strongly affecting the material transport properties. The conventional way to control these rotations is via chemical substitution and doping. For example, stronger distortions and, thus, insulating properties can be achieved by exchanging the A-site cation with smaller ions. Indeed, while  $La_xSr_{1-x}MnO_3$  is a metal (for  $x > 0.15$ ),  $Pr_xCa_{1-x}MnO_3$  (*PCMO*) is an insulator at all temperatures or dopings [117]. Despite the absence of a metallic phase in its equilibrium phase diagram, the electronic phase of *PCMO* has been shown to be efficiently controlled by phonon pumping. Upon vibrational excitation of the highest energy  $Mn - O$  stretching phonon, an increase in the material conductivity of more than five orders of magnitude has been observed [103].

An explanation for such phonon-driven insulator-to-metal transition can be found in the framework of nonlinear phononics [113]. Indeed, by combining electronic structure and dynamical mean-field theory calculations (LDA + DMFT)

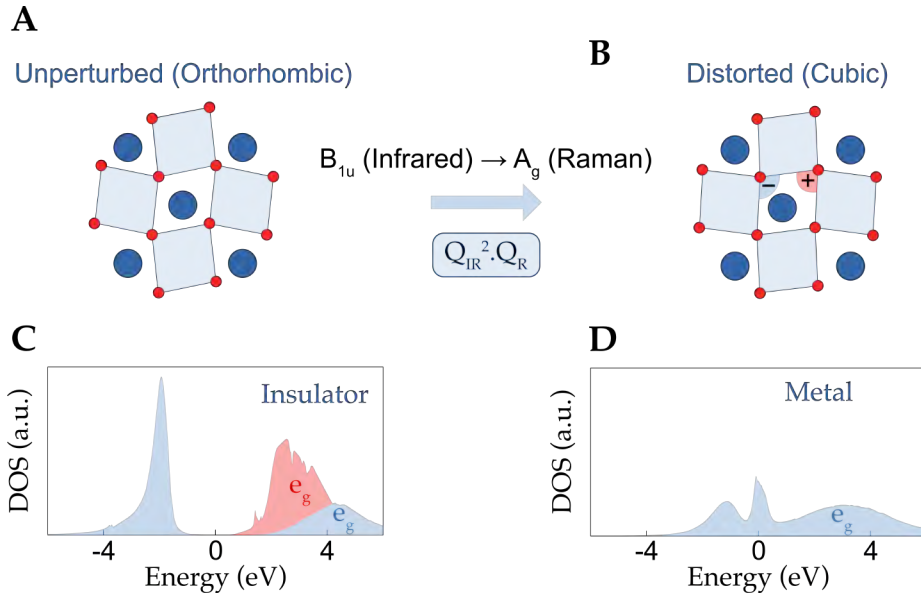


Figure 2.8: Structurally driven electronic transition. (A) Crystal structure of unperturbed *PCMO*. The materials is orthorhombic. (B) Crystal structure of the dynamically distorted phase. The nonlinear coupling between the infrared and Raman phonons transiently reduces the octahedra rotations, resulting in a more cubic structure. (C) Electronic density of states in the orthorhombic phase. The material is an insulator. (D) Density of states in the cubic phase. Following a phonon-driven collapse of the gap, the material became a metal. The image is adapted from [113].

it has been shown<sup>7</sup> that the driven  $Mn - O$  stretching phonon of  $B_{1u}$  symmetry couples nonlinearly to a rotational Raman mode of  $A_g$  symmetry. According to nonlinear phononics, a transient directional force develops along the Raman coordinate and results in a reduction of the rotational distortion of the oxygen octahedra. As a consequence, the material goes from an orthorhombic (Fig. 2.8A) to a more cubic structure (see Fig. 2.8B). Under these conditions, the overlap between the manganese and oxygen orbitals increases favoring a metallic state. While the density of states of the unperturbed orthorhombic material is that of an insulator (Fig. 2.8C), the density of state in the distorted structure is clearly that of a metal with spectral weight at the Fermi level (Fig. 2.8D). It is important to mention that a recent experiment has challenged this interpretation [24]. Time-resolved resonant X-ray diffraction data shows that the charge order melting,

<sup>7</sup> Calculations made for the parent compound *PrMnO<sub>3</sub>*.

induced by the mid-infrared pump, depends nonlinearly on the excitation fluence. This observation is in contrast with the structural mechanism presented above which predicts a linear dependence on the fluence. The authors suggest that a different, nonlinear electron-phonon coupling triggers the metal-insulator transition.

Nevertheless, this experiment successfully proves how strong lattice nonlinearities can be exploited for the optical control of correlated phases.

**CONCLUSIONS** In this chapter, a theory describing the linear and nonlinear behavior of driven phonons has been presented. Importantly, I have shown how nonlinear phonon-phonon coupling, activated by strong-field excitation of infrared-active modes, can be exploited to transiently and selectively distort the structure of complex materials.

The framework developed in this chapter will serve as the foundation for the experiments presented in the rest of the thesis. In particular, I will show how different types of lattice nonlinearities can be used to achieve different degrees of control. In Chapter 3, the nonlinear coupling between infrared-active phonons and strain will be shown to initiate a phase transition towards a ferroelectric phase. In Chapter 4, I will demonstrate how nonlinear spin-phonon couplings allow for the generation of phonon-driven effective magnetic fields.

Part II

LIGHT-INDUCED SYMMETRY BREAKING



# 3

---

## OPTICALLY-INDUCED METASTABLE FERROELECTRICITY

---

In this chapter, I discuss how lattice nonlinearities can be exploited to break inversion symmetry and stabilize a long-range ferroelectric order which is otherwise thermally inaccessible. Excitation of the highest-energy infrared-active phonon in centrosymmetric  $SrTiO_3$  induces features typical of ferroelectrics as revealed by optical and electrical measurements. Strikingly, the photo-induced state was found to be metastable with a multiple hours lifetime. We conclude that the long-lived state is initiated by flexoelectric polarizations driven by inhomogeneous phonon-induced strain <sup>1</sup>.

### 3.1 $SrTiO_3$ : A FAILED FERROELECTRIC

Ferroelectrics are materials that spontaneously break inversion symmetry and develop an electric polarization below a critical temperature  $T_c$  (the Curie temperature). Importantly, such polarization can be reversed by the application of an external electric field.

In a displacive ferroelectric, the transition is driven by a lattice instability that manifests itself in a complete softening of the lowest energy polar “soft” mode (Fig.3.1A). Upon cooling, the frequency of such *soft mode* strongly decreases and

---

<sup>1</sup> The experiment described in this chapter was published in [92]. Some sections were adapted from the Supplementary Materials of the same article.

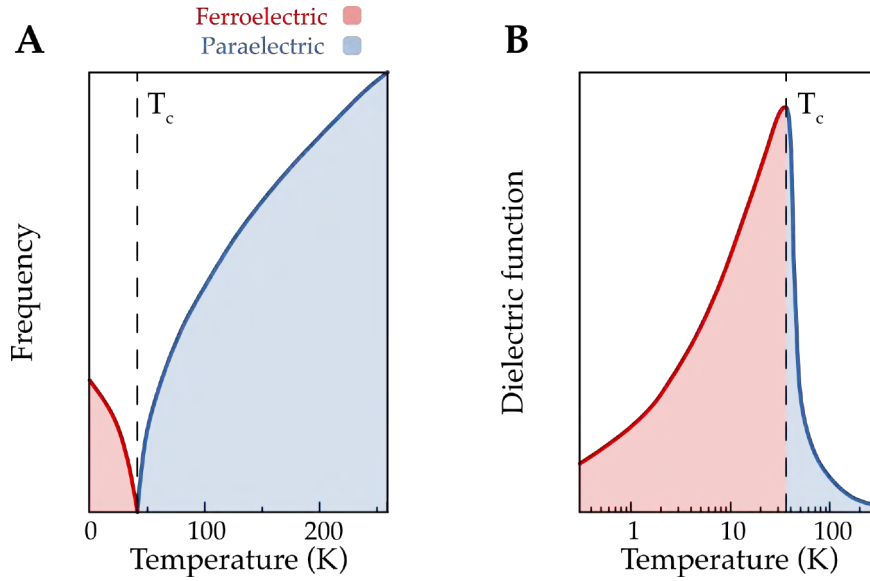


Figure 3.1: Fingerprints of a ferroelectric transition. (A) complete softening of the lowest energy polar phonon. (B) divergence of the dielectric function at the transition temperature.

becomes zero at the transition temperature. The mode freezing displaces the ions into a new structure with a lower symmetry and the relative polar motion between cation and anion results in a spontaneous polarization. Below  $T_c$ , the ions oscillate around the new equilibrium position with the mode frequency increasing with decreasing temperatures.

Another typical fingerprint of a ferroelectric transition consists in the divergence of the dielectric function at the transition temperature (Fig.3.1B). This behavior can be readily understood when considering the Lyddane–Sachs–Teller relationship  $\epsilon_0 \propto 1/\omega_{TO}$ . The softening of a zone-centre phonon results in the divergence of the dielectric function at  $T_c$ .

**INCIPIENT FERROELECTRICITY IN  $SrTiO_3$**   $SrTiO_3$  is an insulator with an optical gap of 3.2 eV (see Fig. 4.1B). This material remains paraelectric and centrosymmetric at all temperatures. At 105 K, it undergoes an antiferrodistortive (AFD) transition from cubic to tetragonal, although it retains a center of inversion (see Fig. 4.1A for the low-temperature crystal structure). When cooled,

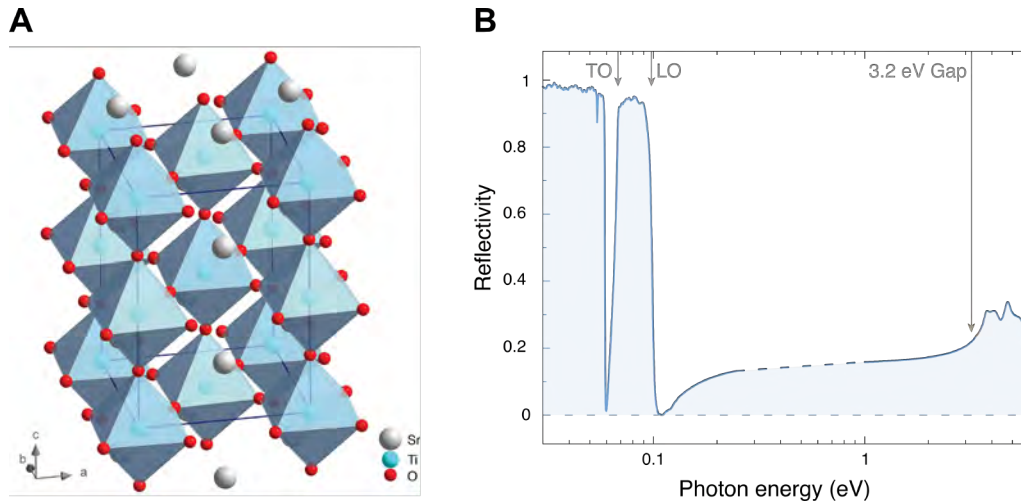


Figure 3.2: (A) low-temperature tetragonal structure of  $SrTiO_3$  (from [60]). (B) Reflectivity. The grey arrows highlight the TO and LO frequency of the highest energy phonon and the position of the optical gap. The data for photon energies smaller than 0.2 eV were measured with an FTIR. The data for photon energies higher than 1 eV were adapted from [23].

it displays many anomalies that suggest its proximity to a ferroelectric phase. The frequency of the lowest energy polar mode closely follows the expected behavior of a paraelectric approaching a ferroelectric transition: a significant mode softening takes place for decreasing temperatures [133]. However, instead of vanishing, the phonon frequency saturates to a finite value and no transition takes place (Fig. 3.3A). The observed softening, suggestive of a zone centre mode instability, appears to extrapolate following a Curie-Weiss law to a putative ferroelectric transition temperature of around 37 K (Fig. 3.3A dotted line). This is the temperature at which the mode frequency would have become zero if it did not stabilize at a finite value.

The same anomalous behavior can be observed in the temperature dependence of the dielectric function [106]. While  $\epsilon_0$  grows substantially for decreasing temperatures, a maximum never develops and the permittivity saturates (Fig. 3.3B).

The behavior shown in Fig. 3.3 is often referred to as *incipient ferroelectricity* because the material appears to be on the verge of a ferroelectric transition even if long-range order never develops spontaneously.

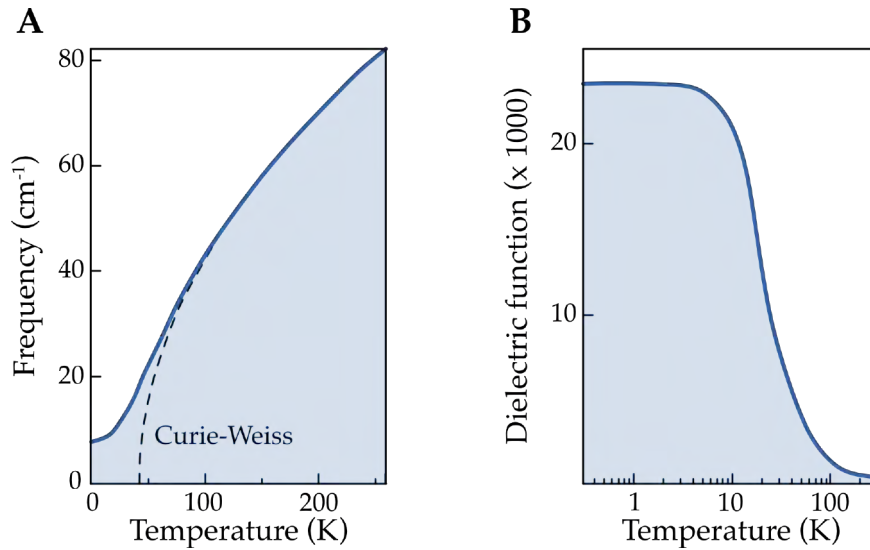


Figure 3.3: Incipient ferroelectricity in  $SrTiO_3$ . (A) incomplete softening of the lowest energy polar mode (adapted from [106]). (B) despite a strong increase with decreasing temperatures, the dielectric function does not diverge (adapted from [133]).

$SrTiO_3$  : A QUANTUM PARAELECTRIC      The absence of a ferroelectric transition despite significant phonon softening and strong dipolar correlations are signatures of a *quantum paraelectric* phase [85, 86]. In such a state, the ferroelectric transition is suppressed by quantum fluctuations of the atomic positions. In other words, the ions would want to displace in a specific direction but strong zero-point motion overcome this tendency, preventing the formation of long-range order.

In transition metal oxides, it is usually possible to neglect quantum effects of the ionic motion because of their heavy masses. However, when the energy barriers between different structural phases are very small, as in the case of  $SrTiO_3$ , suppression of a phase transition due to zero-point motion becomes possible, even in materials made of massive ions. Indeed, ab-initio calculations that consider the atomic motion as classical, always predict  $SrTiO_3$  to be ferroelectric (Fig. 3.4 blue). However, when quantum fluctuations of the ionic positions are taken into account [139] the ferroelectric transition is found to be almost entirely suppressed (Fig. 3.4 red).

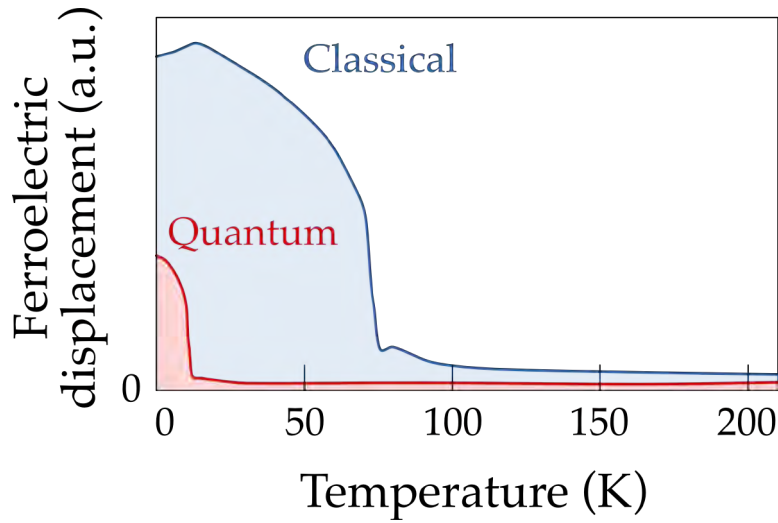


Figure 3.4: Quantum fluctuations suppress the ferroelectric order. The plot displays the size of the ferroelectric displacement in  $SrTiO_3$  as a function of temperature with (red) and without (blue) considering zero-point motion (adapted from [139]).

### 3.2 STATICALLY-INDUCED FERROELECTRICITY

Despite the lack of a spontaneous transition,  $SrTiO_3$  is exceptionally sensitive to perturbations. The proximity to multiple collective states is underscored by the ease with which  $SrTiO_3$  can be forced to change phase. While Calcium substitution [8], isotope substitution [48], the application of electric fields [41, 42] and strain [108] drive the material into a ferroelectric state, extremely low doping concentrations make it superconductive [66, 109]. In some cases, superconductivity and ferroelectricity can even coexist [104].

**CHEMICAL AND ISOTOPE SUBSTITUTION** Substitution of  $^{16}O$  oxygen atoms with the heavier isotope  $^{18}O$  induces ferroelectricity with a maximum critical temperature of  $T_c = 25K$  [48]. The ordered phase appears for  $^{18}O$  isotope concentrations higher than 33% [126] as evidenced by the divergence of the dielectric function [126] (Fig. 3.5A) and the complete softening of the lowest energy polar mode [115] (Fig. 3.5B). The increased mass of the isotope is believed

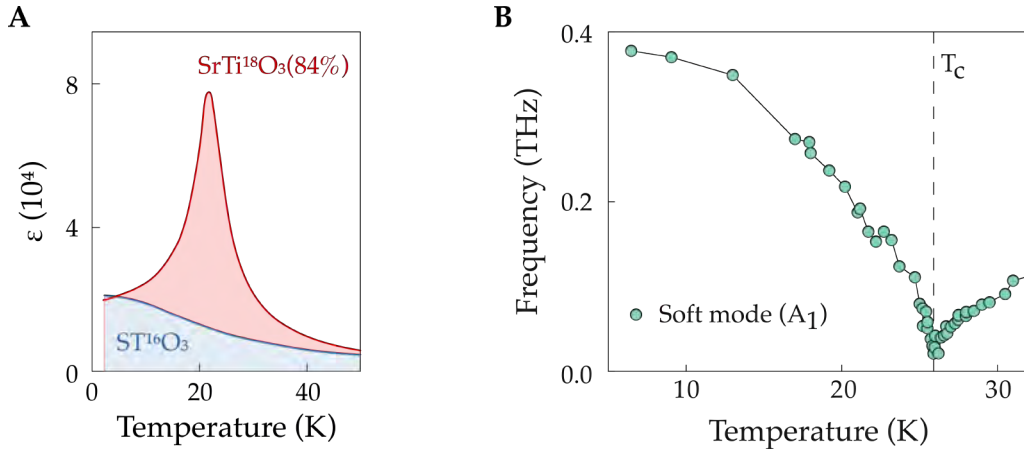


Figure 3.5: Induced ferroelectricity by isotope substitution. (A) dielectric function as a function of temperature in unsubstituted, paraelectric (blue) and in 84% isotope-substituted, ferroelectric (red)  $\text{SrTiO}_3$  (adapted from [126]). (B) Frequency of the lowest energy (“soft”) phonon in isotope-substituted  $\text{SrTiO}_3$  (adapted from [115]).

to favor the transition to a ferroelectric state for two separate reasons [123]. First, an heavier mass translates into an intrinsically lower phonon frequency (the phonon is “softer”) which brings the system closer to a structural instability. Second, more massive ions suppress quantum fluctuations of the ionic positions, allowing for the transition to spontaneously occur.

An alternative way to induce a phase transition in  $\text{SrTiO}_3$  consists in doping it with suitable cations [8]. For example,  $\text{SrTiO}_3$  becomes ferroelectric when a small amount of strontium atoms is substituted with isovalent calcium ( $\text{Sr}_{1-x}\text{Ca}_x\text{TiO}_3$ ,  $x > 0.002$ ). Interestingly, the maximum critical temperature that can be achieved ( $T_c$  depends on the doping) is again in the tens of Kelvin range ( $T_c = 37\text{K}$ ).

**STRAIN** While different methods can make  $\text{SrTiO}_3$  ferroelectric, the application of biaxial strain to thin films has proven to be most effective in controlling the transition [108]. Oxide thin films are epitaxially grown on high quality oxide substrates. Different thermal expansion coefficients and lattice spacings between the substrate and the film can both result in significant biaxial strains. Because of the reduced dimensions, enormous strains up to several percents can be applied

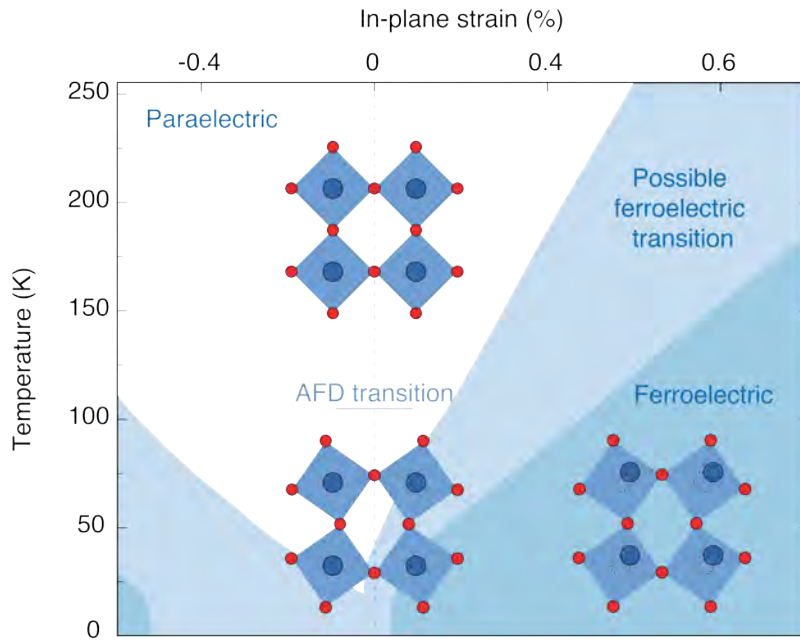


Figure 3.6: Strain-induced ferroelectricity. The phase diagram is obtained by minimizing the total free energy of  $SrTiO_3$  as a function of polarization and strain. The dark blue areas indicate the regions of the diagrams where the material is calculated to be ferroelectric. The light blue areas indicate the range of temperatures and strain values in which the transition could occur. The image is adapted from [73].

without damaging the material. Epitaxial strain has been used to modify the critical temperatures in superconducting [13, 107] and magnetic [7, 36] materials by several degrees. In the case of  $SrTiO_3$ , even small amounts of strain steer the material into a ferroelectric phase, with reported transition temperatures exceeding room temperature [40] (in Fig. 3.6 we show a thermodynamic analysis).

These experiments highlight the prominent role of lattice deformations in controlling the ferroelectric properties of this material.

### 3.3 OPTICALLY-INDUCED FERROELECTRICITY

The close proximity to different collective phases and the anomalous susceptibility to external stimuli render  $SrTiO_3$  an ideal candidate to explore light-driven phase control. In particular, in this Section I discuss how nonlinear excitation of an infrared-active phonon can break inversion symmetry and induce a ferroelectric order.

In the experiments reported here, the highest-energy  $A_{2u}$  vibrational mode of a cryogenically cooled (at  $T = 4\text{ K}$ )  $SrTiO_3$  sample was excited with femtosecond mid-infrared pulses tuned to  $15\ \mu\text{m}$ -wavelength ( $83\ \text{meV}$  photon energy, see Fig. 4.1B for the phonon reflectivity). The pump polarization was aligned along the  $[001]$  axis of a  $(110)$ -oriented crystal. As a probe of light-induced symmetry breaking [28], we monitored the sample via second harmonic generation (SHG) of a  $2.2\ \mu\text{m}$ -wavelength optical probe pulse (see Fig. 3.7 for the experimental setup). By symmetry, dipole SHG is only allowed in crystals without a center of inversion, like ferroelectrics, while it is zero in centrosymmetric materials, like  $SrTiO_3$ . The probe was collinear and time-delayed with respect to the mid-infrared pump. The second harmonic ( $1.1\ \mu\text{m}$  wavelength) was detected in transmission geometry.

**LIGHT-INDUCED SYMMETRY BREAKING** Upon vibrational excitation, a time-delay-independent second harmonic signal, absent at equilibrium, was observed to appear and grow with the exposure time to mid-infrared radiation (Fig. 3.8, left). After several minutes, the second harmonic growth reached a saturation value, determined by the pump fluence<sup>2</sup>. Because in our experimental geometry surface and quadrupole contributions to the nonlinear susceptibility tensor are negligible, the appearance of a second harmonic signal demonstrates

---

<sup>2</sup> Also the growth rate was found to depend on the fluence. To a higher fluence corresponded a faster growth.

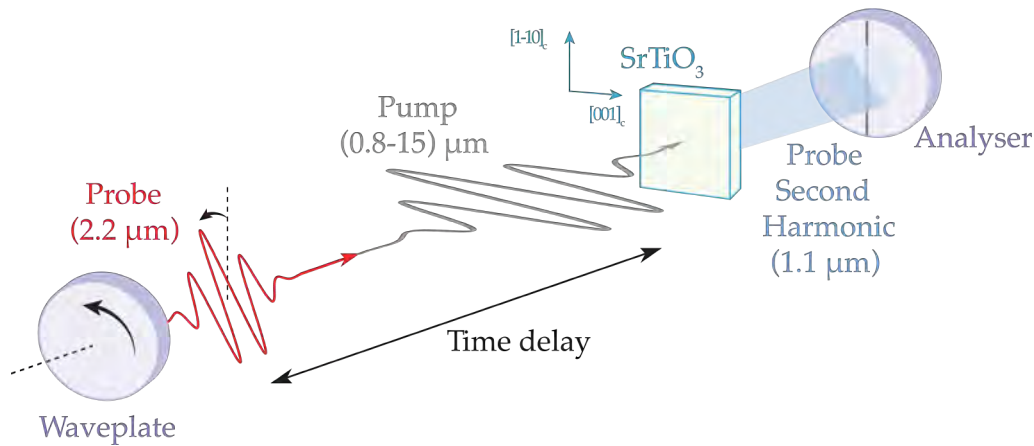


Figure 3.7: Experimental setup. The sample (green) was excited with tunable pump pulses (0.8 to 15  $\mu\text{m}$ , gray line) impinging at normal incidence. The probe pulse (2.2  $\mu\text{m}$  wavelength, red line) polarization was controlled with a half-waveplate. The generated second harmonic (1.1  $\mu\text{m}$ , blue) was detected in transmission. When needed, orthogonal polarization components of the second harmonic could be isolated by an analyzer, that is, a polarizer. The full width at half maximum (FWHM) spot sizes were 72  $\mu\text{m}$  and 52  $\mu\text{m}$  for the pump and the probe beams, respectively.

that the material is driven into a new phase with broken inversion symmetry<sup>3</sup>. Information on the structure and point group of the photo-induced phase were obtained via second harmonic polarimetry measurements. The incoming probe polarization was continuously rotated while only the second harmonic polarized along the two orthogonal pseudo-cubic  $[1 - 10]$  and  $[001]$  crystallographic directions was measured. The detected angular dependences (Fig. 3.9) were fully consistent with a (non-centrosymmetric) polar point group ( $C_{2v}$ ), indicating the formation of a polar order with polarization along the  $[1 - 10]$  direction. In the next paragraph, I explain in more detail the analysis leading to these conclusions.

**SECOND HARMONIC POLARIMETRY** In order to determine the point group of the photo-induced phase and, in particular, if it is polar, we analyze the

<sup>3</sup> See next sections for a more detailed analysis.

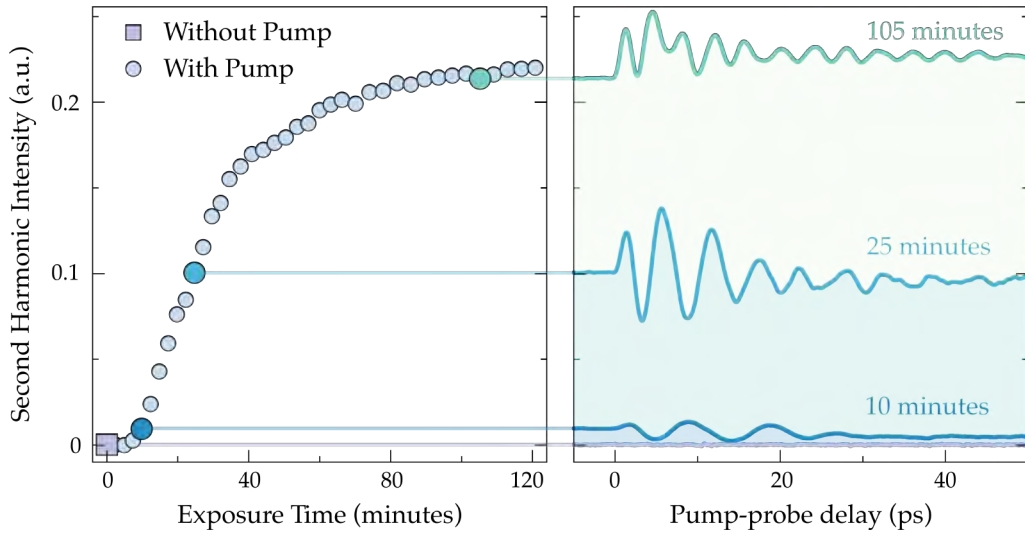


Figure 3.8: Light-induced symmetry breaking. Left: growth of baseline second harmonic signal as a function of exposure time to mid-infrared radiation. Note that this signal is independent on the pump-probe delay. Right: ultrafast pump-induced dynamics.

angular dependence of the generation process. Dipole SHG can be described by the relationship [11]:

$$P_i(2\omega) = \sum_{jk} \chi_{ijk}^{(2)} E_j(\omega) E_k(\omega) \quad (3.1)$$

where  $\chi^{(2)}$  is the third-rank nonlinear susceptibility tensor,  $E(\omega)$  is the impinging electric field which oscillates at frequency  $\omega$  and  $P(2\omega)$  is the induced nonlinear polarization oscillating at frequency  $2\omega$ . The indices  $i, j, k$  identify the tensor components along the axes  $(x, y, z)$ .

Only 21 of the 32 crystallographic point groups are non-centrosymmetric. Among these, only 10 allow for a spontaneous polarization to develop along a unique axis, that is, they are polar. The number of non-zero tensor elements in  $\chi^{(2)}$  is dictated by the point group symmetry. At equilibrium, bulk  $SrTiO_3$  is centrosymmetric at all temperatures and below the 105 K antiferrodistortive structural transition it belongs to the  $D_{4h}$  ( $4/mmm$ ) point group. The different components of  $\chi^{(2)}$  can be accessed by rotating the polarization of the incident

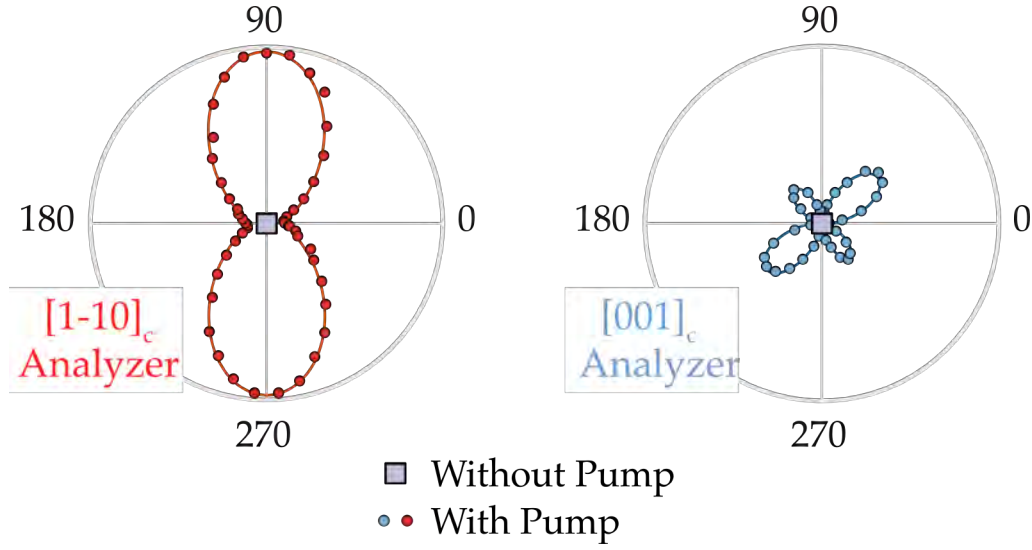


Figure 3.9: Second harmonic polarization dependence. The second harmonic intensity is displayed as a function of the polarization angle of the impinging  $2.2 \mu\text{m}$  probe. Only the second harmonic emitted along the  $[1 - 10]$  (left panel) or  $[001]$  (right panel) crystallographic directions was measured.

electric field and analyzing the polarization of the second harmonic along two orthogonal directions. In the experiment, the probe light impinged normal to the  $(110)$  surface, propagating parallel to the  $z = [110]$  direction (Fig. 3.7). The probe was polarized in the  $xy$ -plane defined by the  $[001]$  and  $[1 - 10]$  crystallographic axes in pseudocubic notation. For simplicity, we rewrite Eq. 3.1 in its reduced form,

$$P_i(2\omega) = \varepsilon_0 d_{ij} E_j^2(\omega) \quad (3.2)$$

where  $\varepsilon_0$  is the vacuum permittivity,  $d_{ij}$  is the reduced nonlinear susceptibility tensor and  $E_j^2(\omega) = (E_x^2, E_y^2, E_z^2, 2E_y E_z, 2E_x E_z, 2E_x E_y)$  ( $j$  indexes the vector elements). In our measurements, the linear polarization of the incident light was continuously rotated in the  $xy$  plane with a half-waveplate and the transmitted second harmonic polarized either along  $x$  or  $y$  was selected with an analyzer that

$d_{ij}$ lab frame	$d_{ij}$ crystal frame	Fit value ( $C_1, C_s$ )	Fit value ( $C_2, C_{2v}, C_4, C_{4v}$ )
$d_{11}$	$d_{11}$	0.462	0
$d_{12}$	$d_{12}$	0.047	0
$d_{16}$	$d_{15}$	3.648	3.417
$d_{21}$	$d_{31}$	1.284	1.195
$d_{22}$	$d_{33}$	5.351	5.804
$d_{26}$	$d_{35}$	-0.056	0

Table 3.1: Reduced nonlinear susceptibility tensor. The components of  $d_{ij}$  are shown in both the lab and crystal frame of reference. The fit values were obtained by assuming the crystal point group symmetry to be  $C_1$  or  $C_s$ , as well as  $C_2$ ,  $C_{2v}$ ,  $C_4$ , or  $C_{4v}$ . In the second case, three components must be zero by symmetry.

is, a polarizer. Eq. 3.2 can be rewritten as a function of the probe polarization angle  $\theta$  relative to the  $x$  axis:

$$\begin{aligned} P_x(2\omega) &= \varepsilon_0 E_0^2(\omega) [d_{11}\cos^2\theta + d_{12}\sin^2\theta + 2d_{16}\cos\theta\sin\theta] \\ P_y(2\omega) &= \varepsilon_0 E_0^2(\omega) [d_{21}\cos^2\theta + d_{22}\sin^2\theta + 2d_{26}\cos\theta\sin\theta] \end{aligned} \quad (3.3)$$

for  $x$  and  $y$  analyzer polarizations, respectively. Because the detector only measures the second harmonic intensity, the plots in Fig. 3.9 represent the intensity as a function of the impinging polarization angle  $I_x(2\omega, \theta) \propto |P_x(2\omega, \theta)|^2$  and  $I_y(2\omega, \theta) \propto |P_y(2\omega, \theta)|^2$ . These data are simultaneously fit using Eqs. 3.3 with free parameters  $E_0$ ,  $d_{11}$ ,  $d_{12}$ ,  $d_{16}$ ,  $d_{21}$ ,  $d_{22}$ , and  $d_{26}$ . Note that the components in Eqs. 3.3 are expressed in the laboratory frame. Because the crystal axes orientation in the pumped  $SrTiO_3$  phase is known,  $d_{ij}$  can also be written in the crystal frame. The fit values for  $d_{ij}$  are given in Table 3.1.

Two important pieces of information can be extracted from table 3.1. First, because the largest component is  $d_{22}$ , the primary symmetry axis in the photo-induced phase can be considered to be  $y = [1 - 10]$ . Second, the elements  $d_{11}$ ,  $d_{12}$  and  $d_{26}$  are far smaller in magnitude than  $d_{22}$  and, thus, can be considered

to be zero by symmetry<sup>4</sup>. These observations imply that in the crystal frame the only components of the nonlinear susceptibility tensor to be non-zero are  $d_{15}$ ,  $d_{31}$ ,  $d_{33}$ . Only nine point groups (besides the triclinic  $C_1$ ) are consistent with this constraint:  $C_s$ ,  $C_2$ ,  $C_{2v}$ ,  $C_4$ ,  $C_{4v}$ ,  $C_3$ ,  $C_{3v}$ ,  $C_6$ , and  $C_{6v}$ . Importantly, all of the possible point groups are polar, and of these, five ( $C_s$ ,  $C_2$ ,  $C_{2v}$ ,  $C_4$ ,  $C_{4v}$ ) are subgroups of the point group of unperturbed  $SrTiO_3$  ( $D_{4h}$ ). If the photo-induced phase transition is second order and/or displacive, a group-subgroup relation between the initial and pump-induced point groups must hold. Because of the experimental geometry, it is not possible to distinguish with polarimetry the four groups  $C_2$ ,  $C_{2v}$ ,  $C_4$ , or  $C_{4v}$ . However, despite the above mentioned limitations and constraints, the fit quality for these point groups is excellent. The fit values for  $d_{ij}$ , assuming different point symmetries, are shown in Table 3.1.

The symmetry analysis presented here, demonstrates that the nonequilibrium phase induced by mid-infrared radiation is polar with a photo-induced polarization aligned with the  $[1 - 10]$  direction. While it is not possible to identify the exact point group that describes the new phase, it is important to note that the polarimetry measurements are fully consistent with the  $C_{2v}$  point group. Importantly, this is the same point group which describes the ferroelectric phase in  $^{18}O$ -isotope substituted [3] and  $Ca$ -substituted [65]  $SrTiO_3$ .

QUADRUPOLE AND SURFACE CONTRIBUTION      The previous symmetry analysis was made assuming that the nonlinear light-matter interaction occurs in the bulk within the dipole approximation. However, in general, even centrosymmetric materials can generate second harmonic which originates from the (much weaker) bulk electric quadrupole and surface electric dipole contributions. In this paragraph, I investigate these two second harmonic sources and conclude

<sup>4</sup> A reasonable assumption within the experimental error.

that they should not be considered in the analysis of the observed nonlinear signal.

The second harmonic polarization arising from the electric quadrupole can be written as [134]:

$$P_i(2\omega) = \sum_{ijkl} \Gamma_{ijkl} E_{ijk}(\omega) \nabla_k E_l(\omega) \quad (3.4)$$

where  $\Gamma_{ijkl}$  is the fourth-rank quadrupole susceptibility tensor<sup>5</sup>. The probe electric field can be written as:

$$\vec{E}(\vec{r}, t) = E_0 e^{i(\kappa z - \omega t)} [\cos\theta \vec{x} + \sin\theta \vec{y}] \quad (3.5)$$

where  $E_0$  is the field amplitude,  $\kappa = \frac{2\pi n}{\lambda}$  is the momentum, and  $\theta$  is the polarization angle with respect to the  $x$  axis. By inserting Eq. 3.5 into Eq. 3.4 it becomes clear that in our experimental geometry the only accessible terms are those with  $k = z$  and  $j, l = x$  or  $y$ . For these reasons, only terms of the form  $\Gamma_{ijzl}$  where  $i, j, l = x$  or  $y$  should be taken into account. In the equilibrium tetragonal phase of  $SrTiO_3$ , with symmetry  $D_{4h}$ , 21 components of  $\Gamma_{ijkl}$  are non-zero and only nine are independent. The tensor can be then rewritten as [134]:

$$\begin{aligned} \Gamma_{ijkl} = & a_1 \delta_{ijkl} + a_2 (\delta_{ij} \delta_{kl} + \delta_{il} \delta_{jk}) + a_3 \delta_{ik} \delta_{jl} + a_4 \delta_{ij} \delta_{zz} + a_5 \delta_{il} \delta_{jk(z)} + \dots \\ & + a_6 \delta_{ik} \delta_{jl(z)} + a_7 \delta_{jl} \delta_{ik(z)} + a_8 (\delta_{ij(z)} \delta_{kl} + \delta_{il(z)} \delta_{jk}) + a_9 \delta_{ijkl(z)} \end{aligned} \quad (3.6)$$

where  $\delta$  is the Kronecker delta, and  $a_i$  are constants. Terms of the form  $\delta_{ij} \delta_{kl}$  imply  $i, j \neq k, l$  and the label (z) signifies  $\delta_{ij(z)} = 1$  when  $i = j = z$ . The elements  $\Gamma_{ijkl}$ , defined by Eq. 3.6, are non-zero only when each index appears an even number of times. However, these elements are inaccessible in the experiment presented here. Therefore, the electric quadrupole contribution should be neglected.

<sup>5</sup> Note that the indices refer to the laboratory frame.

An additional source of second harmonic originates from the crystal surface, due to the intrinsic inversion symmetry breaking that occurs at the interface between the vacuum and the bulk. In (110)-oriented  $SrTiO_3$ , the point group symmetry reduces from  $D_{4h}$  to  $C_s$  at the surface. In this case, the polar axis is perpendicular to the sample surface. Importantly, the tensor elements that we measure experimentally to be dominant ( $d_{21}$ ,  $d_{22}$ ,  $d_{16}$ ) are zero by symmetry in the surface second-order susceptibility tensor. The other detected tensor components ( $d_{11}$ ,  $d_{12}$ ,  $d_{26}$ ) could originate from the surface. However, because they are much smaller than the other measured elements and because no second harmonic could be detected before exciting the sample with mid-infrared light, it is possible to conclude that also the surface contribution to the second harmonic signal is negligible.

The above analysis establishes that both the bulk electric quadrupole and surface sources of second harmonic are negligible or not detectable in our experimental geometry. It is therefore possible to conclude that the growing second harmonic signal in photo-excited  $SrTiO_3$  originates from the electric dipole term and, as such, it is a reliable reporter of photo-induced, bulk symmetry breaking.

**POLAR STATE STABILITY** Given the extremely long timescales required to grow such a state (as compared to the 150 femtoseconds duration of the excitation), it is reasonable to wonder if and how the polar phase relaxes back to the equilibrium ground state once the pump is removed. Surprisingly, the pump-induced phase was found to be extremely robust if unperturbed, relaxing back to the non-polar equilibrium paraelectric phase only several hours after the pump was interrupted. The metastability of the polar state was confirmed by growing the state to saturation and then by simultaneously removing the pump and the probe. To avoid any disturbance to the state, the remaining second harmonic intensity was then briefly and rarely sampled at later times by the

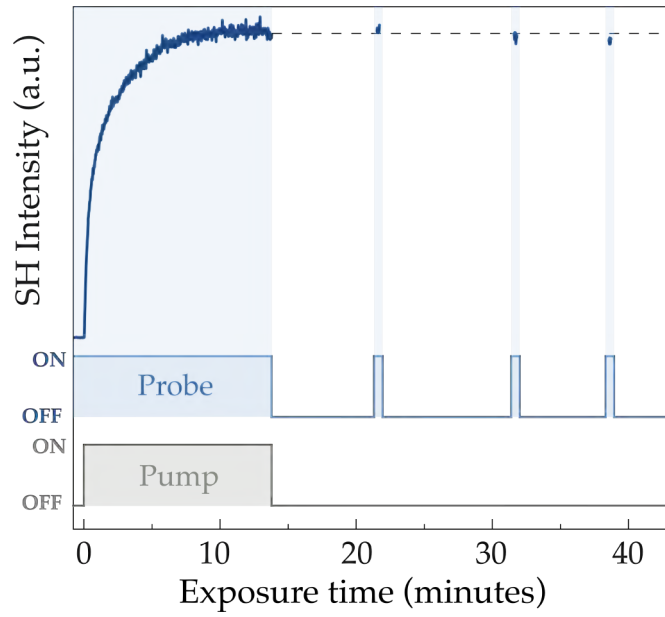


Figure 3.10: Polar state stability. The remaining second harmonic intensity was rarely and briefly sampled after removal of the pump.

probe (Fig. 3.10). The second harmonic signal reduced by only 2% in around 30 minutes, confirming the metastability of the polar phase.

**POLAR STATE ERASURE** However, the photo-induced state could be reverted to the paraelectric ground state by exposing the transformed area to above-bandgap radiation ( $> 3.2$  eV). This happens even with the mid-infrared light still impinging on the sample (Fig. 3.11). This observation can be interpreted by noting that UV light generates free carriers which could efficiently screen any induced polarization. Note that this phenomenon is already well known in bulk ferroelectrics and should be even more relevant in dynamically stabilized phases. Furthermore, the excitation with above bandgap photons has been shown to reduce the in-plane rotations of the oxygen octahedra in  $SrTiO_3$ . The increase in crystal symmetry strengthens the stability of the paraelectric phase at the expense of the ferroelectric instability [99]. Once the macroscopic order parameter has been suppressed below some critical strength or length scale

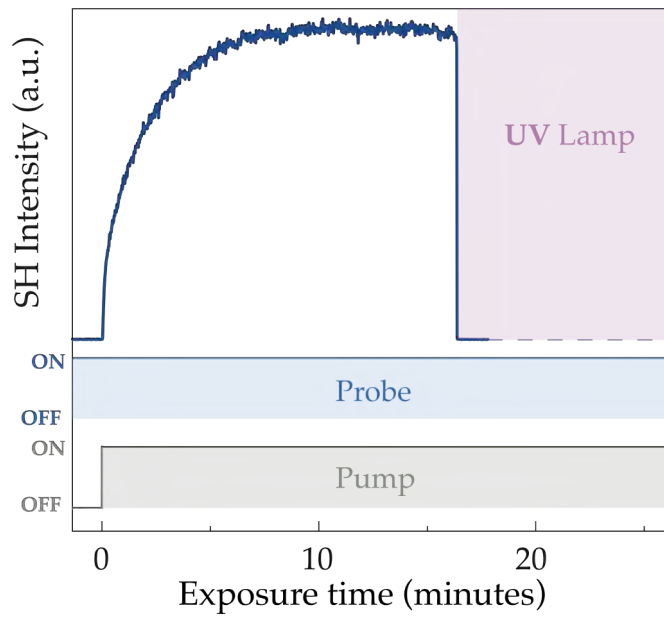


Figure 3.11: Above-bandgap illumination erases the polar state.

and the system has been reverted to its paraelectric phase, the material cannot spontaneously develop a ferroelectric order which is thermally inaccessible. Importantly, as soon as the UV-light is removed the second harmonic starts growing again, provided that the sample is being illuminated by the mid-infrared pulses.

**STABILITY UNDER CONTINUOUS PROBING** The polar state is metastable if it is not perturbed. However, even the interaction with the probe can be detrimental for the photo-induced phase. Fig. 3.12 shows the stability of the induced state while it is being continuously sampled but after the pump is removed. The lifetime changes significantly, decreasing to only few tens of minutes. This observation, suggestive of a destructive interaction between probe photons and the polar phase, can also be understood in the context of polarization screening by photo-generated carriers as in the case of above-bandgap excitation. For  $1.1 \mu\text{m}$  second harmonic photons, which are far smaller than the gap, the probability to produce free carriers via multi-photon processes

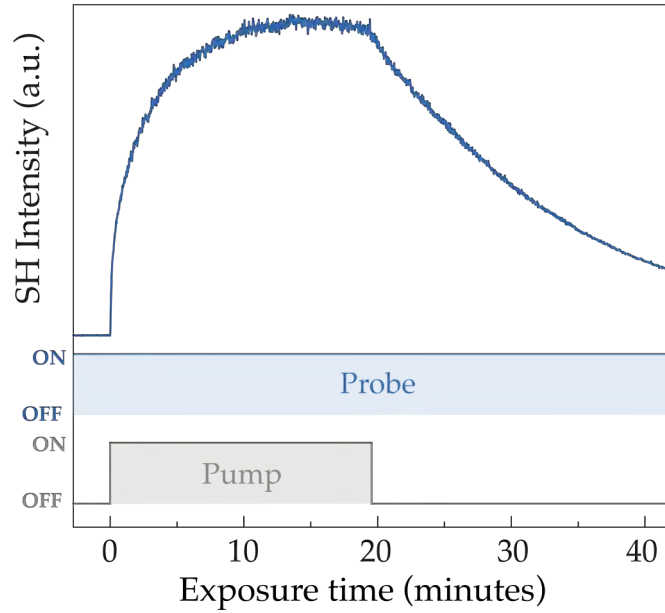


Figure 3.12: Polar state stability under continuous sampling. The mid-infrared light was only active for the first ~20 minutes of the experiment while the probe sampled the second harmonic continuously.

is heavily reduced, yet finite. Thus, over a scale of minutes, with hundreds of thousands of pulses hitting the sample, the probe can also generate enough carriers to erase the polar state. This intuition was confirmed by repeating the same experiments with probe photons closer to but smaller than the optical gap. Probe wavelengths of  $1.6 \mu\text{m}$  and  $0.8 \mu\text{m}$  were used to generate second harmonic phonons of  $0.8 \mu\text{m}$  and  $0.4 \mu\text{m}$  wavelength, respectively. Not only the decay times became faster but it was also increasingly difficult to observe second harmonic growth (still finite for  $1.6 \mu\text{m}$  light, while undetectable for  $0.8 \mu\text{m}$  probe wavelengths). Moreover, for fixed probe photon energies, stronger probe fields also resulted in shorter lifetimes. In conclusion, in order to properly observe the second harmonic growth, it is necessary to use low probe intensities at wavelengths far from the optical gap.

**TEMPERATURE DEPENDENCE** In calcium and isotope substituted  $\text{SrTiO}_3$ , ferroelectricity emerges at temperatures of few tens of Kelvin. In strained

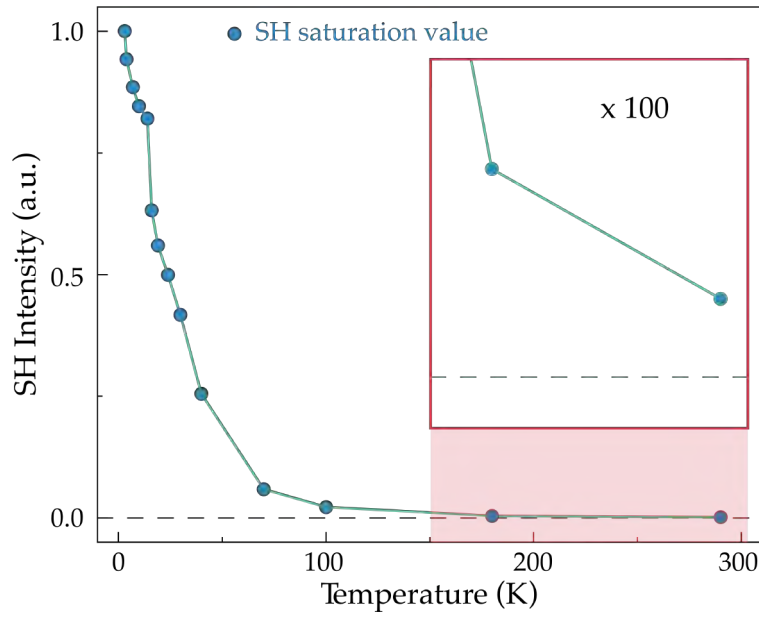


Figure 3.13: Second harmonic temperature dependence. Saturation value of the second harmonic at each temperature (blue dots). All measurements were taken with the same pump wavelength, fluence and pulse duration. Inset: 100 times magnification of the high temperature data.

$SrTiO_3$ , however, ferroelectricity can be stabilized at much higher temperatures, even in excess of room temperature. To investigate how the observed mid-infrared induced polar state compares to these energy scales, the experiment was performed as a function of sample temperature. For each temperature, the same pump fluence was used to grow the polar state till saturation. Fig. 3.13 shows the second harmonic saturation value as a function of temperature. In between measurements, the equilibrium paraelectric state was restored by exposure to UV-light. The induced second harmonic signal was found to be maximum at low temperatures, but remained detectable up to room temperature. The signal did not seem to be affected by the cubic-to-tetragonal structural transition naturally occurring in  $SrTiO_3$  at 105 K. Nevertheless, the size of the pump-induced effect seemed to closely reproduce the behavior of the static dielectric function  $\epsilon_0$  (Fig. 3.3A).

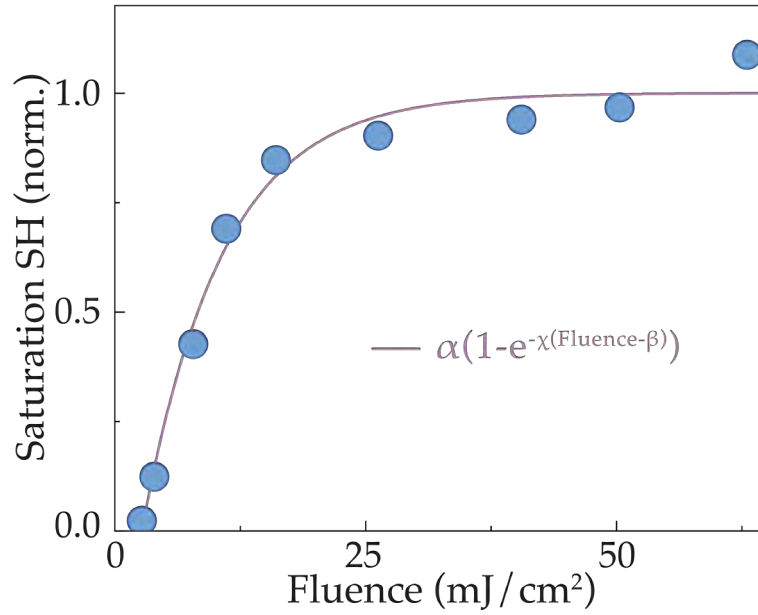


Figure 3.14: Pump fluence dependence. Second harmonic saturation value as a function of pump fluence. The pump wavelength was tuned to  $15 \mu\text{m}$ . Note that in estimating the fluence values, because the pump power was measured outside the cryostat, the diamond window absorption was not considered.

**FLUENCE DEPENDENCE** The experiment was also performed as a function of pump fluence at a constant temperature of 4 K. The dependence of the second harmonic saturation value on the pump fluence is shown in Fig. 3.14<sup>6</sup>. In order to initiate the second harmonic growth, a minimum threshold in fluence was needed. For  $15 \mu\text{m}$  pump wavelengths, resonant with the phonon, the threshold was  $2.7 \frac{\text{mJ}}{\text{cm}^2}$ . Importantly, while at low fluences the amount of second harmonic seemed to scale linearly with the pump intensity, for stronger fields the second harmonic saturation value did not grow any longer resulting in a saturation behavior also in fluence. The experimental data can be fit by the function:

$$f(F) = \alpha(1 - e^{-\chi(F-\beta)}) \quad (3.7)$$

<sup>6</sup> Note that, in between measurements, the material was reverted to its equilibrium paraelectric phase.

where  $F$  is the fluence, and  $\alpha$ ,  $\beta$  and  $\chi$  are the saturation value, the threshold fluence and the photosusceptibility, respectively. The photosusceptibility  $\chi$  is a measure of how rapidly in fluence the polar phase reaches saturation. These parameters will be used in the next paragraph to construct a wavelength dependence of the effect.

**WAVELENGTH DEPENDENCE** To confirm the phononic origin of the observed effect, the experiment was performed as a function of pump wavelength. However, it is usually difficult to compare measurements taken at different wavelengths because the excitation conditions, such as pump penetration depth or reflectivity, change significantly across the electromagnetic spectrum. In addition, if the system is undergoing a photo-induced phase transformation, the “known” optical properties are also expected to vary considerably. For these reasons, the fluence dependence of the second harmonic saturation value was measured and fit with Eq.3.7 at each pump photon energies. The wavelength dependence of the effect can now be estimated by the size of the photosusceptibility  $\chi$ . This quantity measures the efficacy of the pump-induced process directly from the unprocessed data and without relying on equilibrium properties of the material. The photo-susceptibility is maximized for pump photon energies approaching the resonance frequency of the  $A_{2u}$  phonon (Fig. 3.15). On the contrary, the effect is considerably diminished if not entirely missing for photon energies close to the optical gap (3.2 eV).

There is also another way to evaluate the size of the effect. The transformed volume changes considerably due to the different penetration depths of light at different pump photon frequencies. By dividing the second harmonic saturation value (parameter  $\alpha$ ) by the pump penetration depth, it is possible to estimate the the amount of generated second harmonic per unit length. The results, which are shown in Fig. 3.16 (left panel), reproduce qualitatively the behavior observed

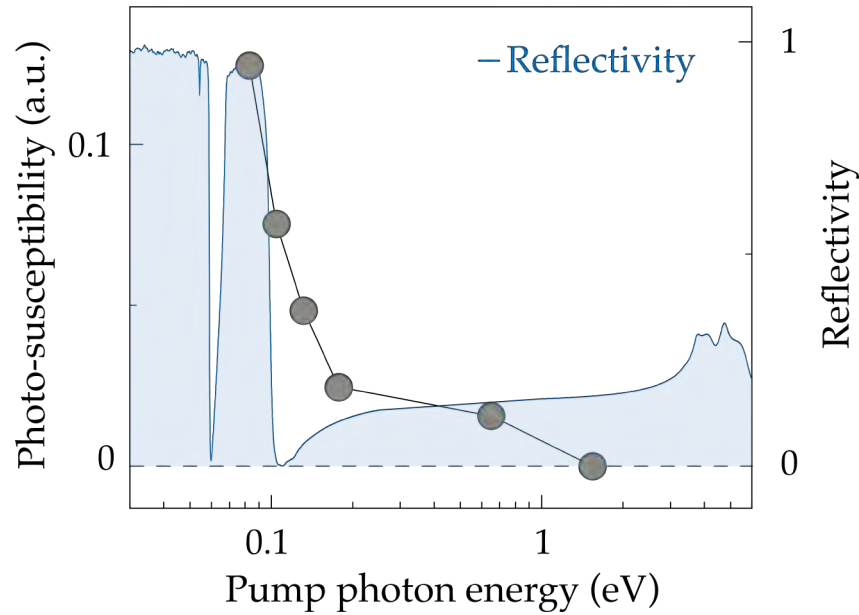


Figure 3.15: Wavelength dependence of the photosusceptibility. The equilibrium reflectivity of  $SrTiO_3$  is shown in light blue.

with the photosusceptibility (Fig. 3.15). The effect is maximum at the phonon resonance.

Lastly, the pump photon energy is also found to strongly affect the threshold fluence (parameter  $\beta$ ). For photons in the proximity of the optical gap, much higher intensities are needed to see any effect (Fig. 3.16, right panel). However, for pump wavelengths closer to the phonon, smaller pump fluences are needed to induce a polar phase.

**ULTRAFAST RESPONSE** So far, only the static second harmonic has been discussed. However, important insights into the induced structural changes can be obtained by considering the pump-induced ultrafast response of Fig. 3.8, right panel. Hyper-Raman spectroscopy involves the modulation of the second harmonic intensity by inelastically driven polar excitations<sup>7</sup>. Figure 4.8A shows the pump-induced ultrafast dynamics of the second harmonic

<sup>7</sup> Note that the “polar” label is lost in non-centrosymmetric media.

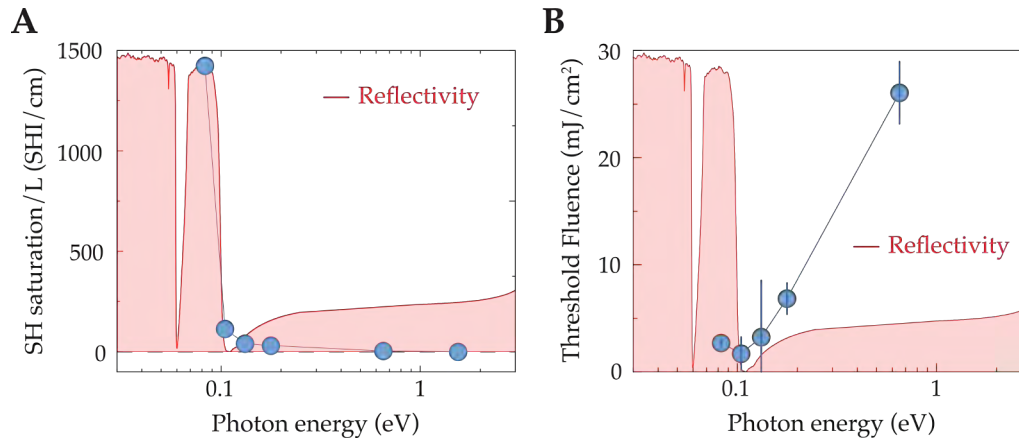


Figure 3.16: (A) saturation second harmonic intensity (parameter  $\alpha$ ) divided by the pump penetration depth. (B) Pump photon energy dependence of the threshold fluence (parameter  $\beta$ ).

after subtracting the background and the slow varying responses. Indeed, the second harmonic signal exhibited ultrafast oscillations that resulted from the pump-driven, impulsive, inelastic excitation of low-frequency polar modes. Three representative measurements taken after 10, 25 and 105 minutes of mid-infrared illumination are shown in Fig. 4.8A. Importantly, the frequency of these oscillations increased visibly with exposure time, as shown comprehensively in Figure 4.8B. A more meaningful comparison can be made by correlating the mode frequency with the amount of total second harmonic (which is in turn proportional to the induced polarization). Also in this case, the mode frequency increased monotonically with the baseline second harmonic. The observed mode-hardening is strongly reminiscent of the behavior of a ferroelectric soft-mode following a paraelectric to ferroelectric phase transition [9, 115, 121] (as discussed in the first section). The appearance and hardening of a low frequency coherent oscillation suggests a long-range symmetry breaking response potentially related to the stabilization of some inherent fluctuating ferroelectric order.

**LIGHT-DRIVEN CURRENT PULSES** The appearance of a metastable polar order and the observation of a ferroelectric-like mode hardening are suggestive of the creation of a laser-induced macroscopic polarization. In ferroelectrics,

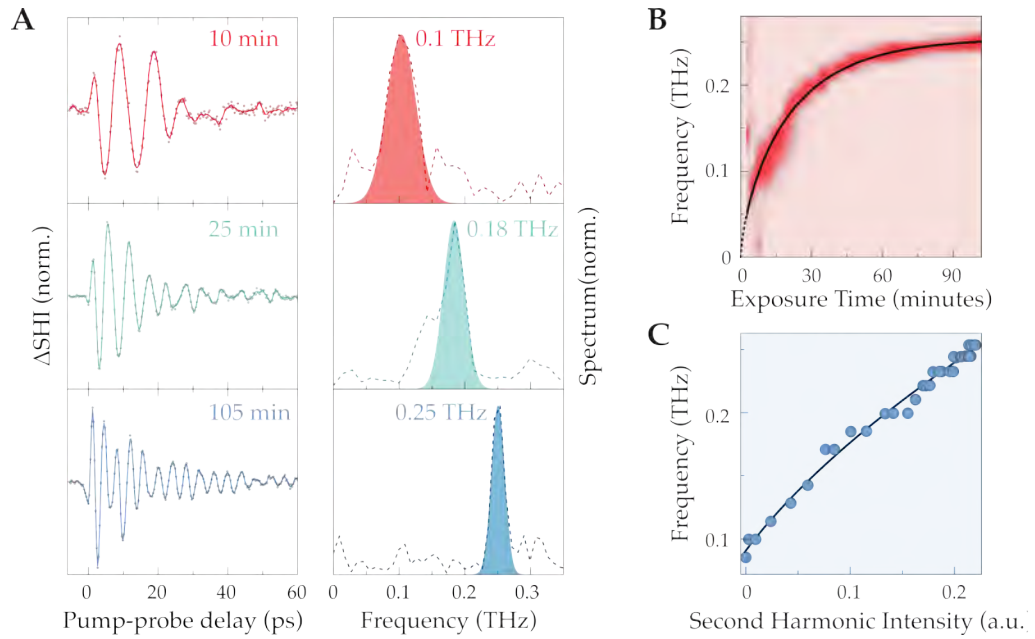


Figure 3.17: Ultrafast Hyper-Raman spectroscopy. (A) Left: mid-infrared-induced modulation of the second harmonic intensity as a function of the pump-probe delay for three representative exposure times. The growing second harmonic offset of Fig. 3.8 was removed. Right: Fourier transform of the time-dependent traces. The red, green and blue peaks are gaussian fits. (B) Fourier transform of the oscillatory traces for different exposure times. The spectra have been normalized for each measurement to better visualize the frequency change and not be affected by the different oscillation amplitudes. The data before minute 5 only contain noise (no second harmonic has grown yet) and, thus, they are not shown. (C) Frequency of the detected oscillations as a function of total second intensity. The dots represent the frequency at which the Fourier spectrum of each time-dependent trace is maximized.

when the electrical polarization switches between the two possible directions ( $P^+$  and  $P^-$ ) a switching current develops in an external circuit, typically consisting of two electrodes that sandwich the ferroelectric material. In the same way, when a polarization is created in a paraelectric material, an electrical response should be expected.

To measure the electrical response of  $SrTiO_3$  following mid-infrared irradiation we deposited two gold contacts (4 mm wide Ti/Au) on the sample surface using e-beam evaporation through an aluminum shadow mask. The electrodes were separated by a distance of 1.5 mm along the  $[1 - 10]$  crystallographic direction (Fig. 3.18A), while the optical pump was focussed on a much smaller area (70  $\mu m$  diameter) to avoid direct irradiation of the contacts. In this configuration, the coupling between the transformed area and the external circuit was capacitive. One contact was connected to the input of a transimpedance amplifier (TIA), while the other was directly connected to the same ground of the amplifier. The light-induced electrical response was measured without any applied bias in the short-circuit conditions described above. Short pulses of current were detected at the same 1 kHz repetition rate of the pump laser (Fig. 3.18B). Each mid-infrared pulse produced a sharp pulse of current, followed by a fast decay and a subsequent slow, overdamped oscillation. The measured temporal shape is likely due to the amplifier response to a current pulse shorter than its rise time (7  $\mu s$ ) rather than the actual time-dependence of the photo-induced currents. Nevertheless, the detected signal is a reliable reporter of a pump-driven photocurrent. Importantly, when the pump light was blocked, no current was detectable.

The observation of short-circuit (zero-bias) photocurrents is highly surprising for three reasons. Firstly, since the pump photon energy is far smaller than the energy gap (0.083 eV and 3.2 eV, respectively) no photo-excited carriers can be generated by direct absorption<sup>8</sup>. Secondly, even if there were free carriers,

<sup>8</sup> Impurity centers might play a role in the observed response and will be discussed at the end of the chapter.

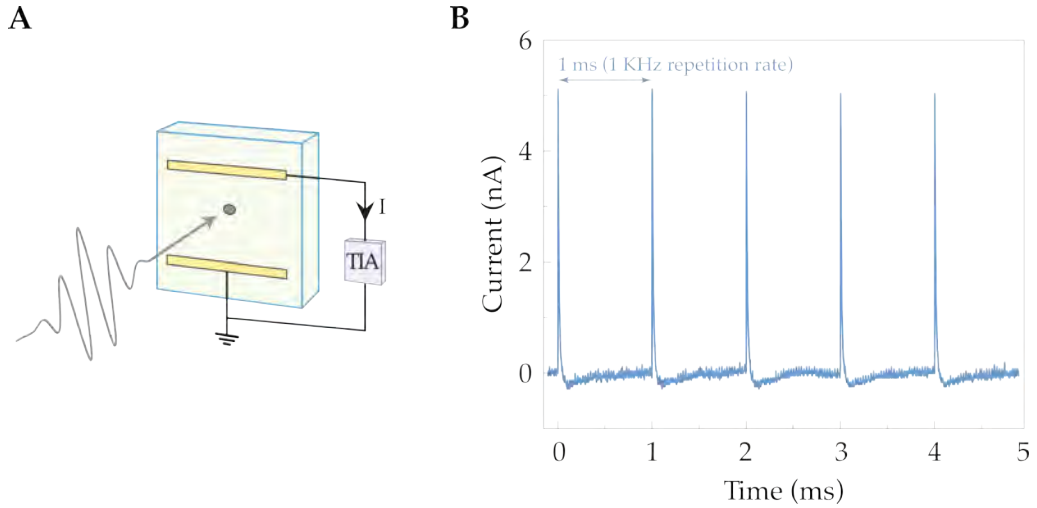


Figure 3.18: Light-driven current pulses. (A) Transport measurements setup. The photo-induced electrical response was measured in short-circuit conditions without applying any bias. Two gold electrodes were deposited on the sample surface, one connected to ground and the other to a transimpedance amplifier (TIA) which shares the same ground. (B) Electrical currents induced in unbiased  $SrTiO_3$  by successive pump pulses (1-kHz repetition rate).

because unperturbed  $SrTiO_3$  is centrosymmetric and no bias is applied to the electrodes, there would be no conventional mechanisms which should lead to charge separation [21, 35]. Lastly, because the distance between the contacts (1.5 mm) is much bigger than the size of the pump pulses ( $72 \mu m$ ), the impact of band bending at the contact/sample interface can also be considered negligible, as the typical depletion width for an  $Au/SrTiO_3$  junction is on the order of  $0.1\text{--}1 \mu m$  [110].

The observed electrical response in an unbiased sample is strongly suggestive of the light-driven creation and enhancement of a polarization akin to the switching current of a poled ferroelectric material.

### 3.4 PHONON-INDUCED STRAIN

In the previous section, we have shown how phonon excitation in a quantum paraelectric reveals signatures typical of ferroelectric materials such as a large

second-order optical nonlinearity, a polar point group, soft-mode behavior and light-driven current pulses. In this section, we propose a possible explanation for the observed phenomenon.

PHONON-INDUCED STRAIN As mentioned at the beginning of the chapter, the application of strain is the most effective way to force  $SrTiO_3$  into a ferroelectric phase. If we consider the dynamical equivalent of the ionic contribution to electrostriction, it is reasonable to expect that a driven phonon can acoustically deform the lattice. A full description of the elastic and structural properties of a material requires the expansion of the free energy in both strain and phonon degrees of freedom [122]:

$$U = \frac{1}{2} c_{ijkl} \varepsilon_{ij} \varepsilon_{kl} + \frac{1}{2} \omega_i^2 Q_i^2 + g_{ijk} Q_i Q_j Q_k + q_{ijkl} \varepsilon_{ij} Q_k Q_l \quad (3.8)$$

where  $c_{ijkl}$  is the elastic tensor,  $q_{ijkl}$  is the electrostrictive tensor,  $\omega_i$  is the phonon eigenfrequency,  $\varepsilon_{ij}$  and  $Q_i$  are the strain and phonon amplitudes, respectively. The first term in Eq. 3.8 accounts for the elastic energy due to a rigid deformation of the crystal lattice. The two terms containing only the phonon amplitude  $Q_i$ , account for the energy corresponding to the atomic arrangement within the crystal lattice. As already mentioned in Chapter 2, the quadratic and cubic terms describe harmonic and anharmonic contributions, respectively. The last, mixing term in Eq. 3.8 which contains both strain and phonon amplitudes accounts for electrostrictive effects. Due to this nonlinearity, a driven phonon can exert a prompt pressure (stress) on the material which turns into an acoustic macroscopic deformation of the lattice (strain). The total stress acting on a sample can be expressed as:

$$\sigma_{ij} = \frac{\partial U}{\partial \varepsilon_{ij}} = c_{ijkl} \varepsilon_{kl} + q_{ijkl} Q_k Q_l \quad (3.9)$$

where the last term accounts for the phonon-induced pressure. The contribution of a single driven phonon is:

$$\sigma_{ij}^{phonon} = q_{ijkl} Q_k^2 \quad (3.10)$$

When considering the effect of an individual infrared-active mode, symmetry considerations restrict the allowed phonon-induced stress components. In particular, only stress components compatible with an irreducible representation of  $A_{1g}$  symmetry which maintain the symmetry of the hamiltonian are possible. In tetragonally distorted  $SrTiO_3$ , there are only two possibilities which fulfill this requirement. The allowed stress components correspond to a pure in-plane ( $a/b$  - axis) stress

$$\sigma_{in-plane} = \left\{ \begin{array}{ccc} \chi_{xx} & 0 & 0 \\ 0 & \chi_{xx} & 0 \\ 0 & 0 & 0 \end{array} \right\} \quad (3.11)$$

or an out of plane ( $[001]_c$ ) stress

$$\sigma_{out-of-plane} = \left\{ \begin{array}{ccc} 0 & 0 & 0 \\ 0 & 0 & 0 \\ 0 & 0 & \chi_{zz} \end{array} \right\} \quad (3.12)$$

Density functional theory (DFT) calculations<sup>9</sup> allow for a quantitative estimate of the above-mentioned phonon-induced stress. In the low-temperature tetragonal phase of  $SrTiO_3$  (space group  $I4/mcm - D_{4h}$ ), there are  $N = 10$  atoms per the unit cell, resulting in  $3N - 3 = 27$  zone-center phonons. The polar modes belong to the irreducible representation  $5E_u + 3A_{2u}$  for a total of 13 infrared-active phonons (the  $E_u$  modes are doubly degenerate). The highest-energy mode

<sup>9</sup> Based on [27, 52, 70, 84, 96].

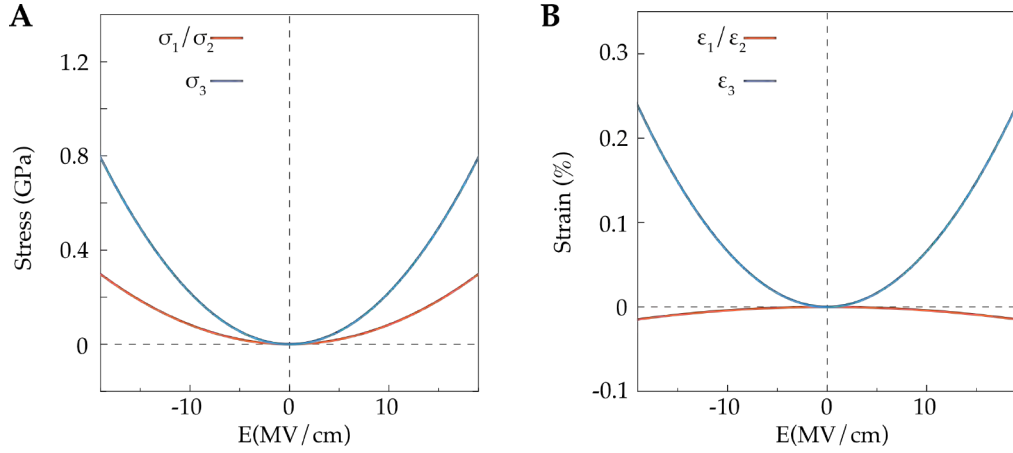


Figure 3.19: (A) First-principles calculations of the phonon-induced stress. (B) Total deformation of the unit cell obtained considering both the phonon-induced stress and the elastic response of the solid.

excited in our experiments is of  $A_{2u}$  symmetry and is polarized along the (tetragonal)  $c$ -axis. Pump pulses tuned at 20 THz (in proximity of the  $A_{2u}$  resonance), 150 fs long and with a maximum field amplitude of  $18 \frac{MV}{cm}$ , induce oxygen displacements of up to 5 picometers, equivalent to about 3% of the equilibrium  $Ti - O$  bond length. For these amplitudes, the peak phonon-induced stress is found to be 0.19 GPa and 0.5 GPa for  $\sigma_{in-plane}$  and  $\sigma_{out-of-plane}$ , respectively. The direct excitation of the  $A_{2u}$  vibrational mode results in an effective expansive pressure both along the tetragonal axis ( $[001]_c$ ) and in-plane, with the former having the strongest magnitude (Fig. 3.19A). It is important to note that because of the nonlinear nature of the electrostrictive coupling ( $\propto Q_{IR}^2$ ), the induced stress is expansive for both positive and negative values of  $Q_{IR}$ .

In order to obtain a quantitative estimate of the induced acoustic deformation (strain) in response to the calculated phonon-driven stress we must consider the full elastic response of the solid, described by Eq. 3.8. The total energy is minimized with respect to the strain variables for fixed values of phonon amplitude. Fig. 3.19B shows the strain as a function of the peak electric field of the impinging mid-infrared pulses. The material expands along the tetragonal axis and compresses along the in-plane axes. This behavior originates from

Poisson's ratio, which in contrast to the phonon-induced stress, tends to maintain the volume constant. As a consequence, to compensate the large stress along the tetragonal axis the system reduces the in-plane dimensions. The strain induced by the optical pulses along the  $c$ -axis is found to be up to 0.2%.

It is important to note that the output of frozen-phonon (DFT) calculations are time-independent quantities. In particular, the instantaneous conversion of stress into strain described in this section does not take into account the inherently different timescales of these two quantities in a macroscopic sample. The prompt stress generated by the optically pumped phonon mode is indeed expected to evolve into transient strain only nanoseconds after the femtosecond mid-infrared pulse<sup>10</sup>. An accurate description of the phenomenon would have to take into account strain-wave and phonon-polariton propagation effects over macroscopic length scales in a material undergoing a phase transition. Such an effort goes far beyond the scope of this thesis. Nevertheless, the estimated acoustic deformation represents an upper bound for the phonon-generated strain.

Importantly, first-principle calculations confirm that an optically-driven phonon in  $SrTiO_3$  can strain the material to large deformations.

### 3.5 FLEXOELECTRIC DOMAINS

The estimated 0.2 % phonon-induced strain would be enough to induce a ferroelectric phase transition (see Fig. 3.6). However, DFT calculations neglect spatial inhomogeneities which arise from the nonuniform nature of the excitation. In reality, the phonon-induced strain profile must follow the gaussian shape of the pump intensity (Fig. 3.20A). In this case, phonon-induced acoustic lattice deformations could result in two different polarization profiles. The most trivial

<sup>10</sup> The relevant timescales can be roughly estimated by considering the speed of sound in  $SrTiO_3$  (around 7900 m/s) and the pump spot size (72  $\mu m$ ).

option involves a direct, strain-induced ferroelectric order, developing in a single domain with a well defined polarization (Fig. 3.20A). Another option accounts for the coupling between the spatial gradient of the optically-induced strain and the polarization (Fig. 3.20B), where  $P \propto \nabla \varepsilon$ . This term arises from the *flexoelectric* effect [140, 142] which is activated by inhomogeneous strain. In this case, pairs of polar domains with opposing polarizations would form (Fig. 3.20A). In the next sections, we will first evaluate more quantitatively how the flexoelectric domains would develop. We will then discuss which types of experiments allow to distinguish between the two possibilities of Fig. 3.20.

**PHONO-FLEXOELECTRIC POLARISATIONS** Strain itself cannot break inversion symmetry and thus induce a polarization. A homogeneously strained centrosymmetric material will retain the center of inversion. This is why piezoelectricity - a polarization induced by homogenous strain - is only allowed in materials which lack a center of inversion. On the contrary, a strain gradient can break inversion symmetry by rendering the structure of a material antisymmetrical. In other words, the strain-induced polarization in a piezoelectric originates from the low symmetry of the unperturbed material while a flexoelectric polarization arises from the symmetry-breaking action of the inhomogeneous deformation. For this reason, flexoelectricity is allowed by symmetry in all solids.

The flexoelectric effect can be expressed as:

$$P_i^{flexo} = f_{ijkl} \nabla_j \varepsilon_{kl}(x, y, z) \quad (3.13)$$

where  $P_i^{flexo}$  is the polarization,  $\varepsilon_{kl}$  is the strain tensor, and  $f_{ijkl}$  is the fourth-rank flexoelectric tensor. The excitation of the infrared mode to large amplitudes results in the phonon-induced stress (pressure) of Eq. 3.10 which is quadratic in the phonon amplitude  $Q_{IR}$ . Owing to the linear relationship between the driving field and the phonon amplitude, and the linear relationship between  $\sigma$  and  $\varepsilon$ ,

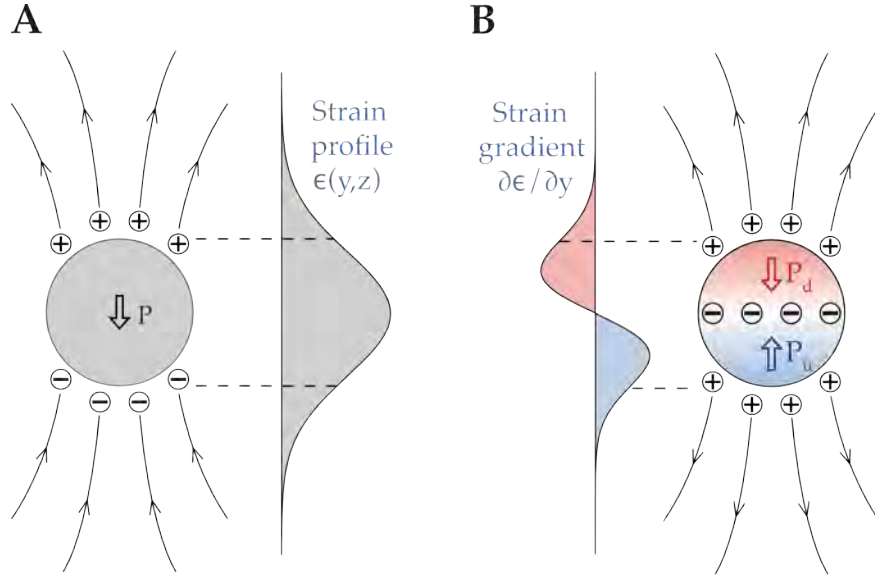


Figure 3.20: Possible domain profiles. (A) Strain profile that follows the Gaussian shape of the pump intensity. A direct, strain-induced transition results in a ferroelectric monodomain. (B) Inhomogeneous strain leads to the formation of two distinct flexoelectric domains, characterized by opposite polarities. In this case, the polarization profile follows the strain gradient.

the spatial profile of the induced strain  $\varepsilon_{ij}(x, y, z)$  on the sample can be retrieved. The pump intensity, which penetrates in the material for the penetration depth  $\delta$ , is assumed to have a Gaussian beam profile:

$$I(x, y, z) = I_0 e^{-\frac{(4ln2)x^2}{w^2}} e^{-\frac{(4ln2)y^2}{w^2}} e^{-\frac{z}{\delta}} \quad (3.14)$$

where  $w$  is the full-width at half-maximum of the pump spot. Assuming  $\varepsilon_{ij}(x, y, z) = \varepsilon_{ij} \frac{I(x, y, z)}{I_0}$ <sup>11</sup>, it is possible to write:

$$P_i^{flexo} = \varepsilon_{kl} e^{-\frac{(4ln2)(x+y)^2}{w^2}} e^{-\frac{z}{\delta}} \left[ (f_{ixkl}x + f_{iykl}y) \left( -\frac{8ln2}{w^2} \right) + f_{izkl} \left( -\frac{1}{\delta} \right) z \right] \quad (3.15)$$

where  $\varepsilon_{kl}$  are the values obtained with DFT calculations which are spatially independent. Experimental values for  $f_{ijkl}$  in  $SrTiO_3$  are available only in the

<sup>11</sup> Again, the lab frame is  $x = [001]$ ,  $y = [1 - 10]$ ,  $z = [110]$ .

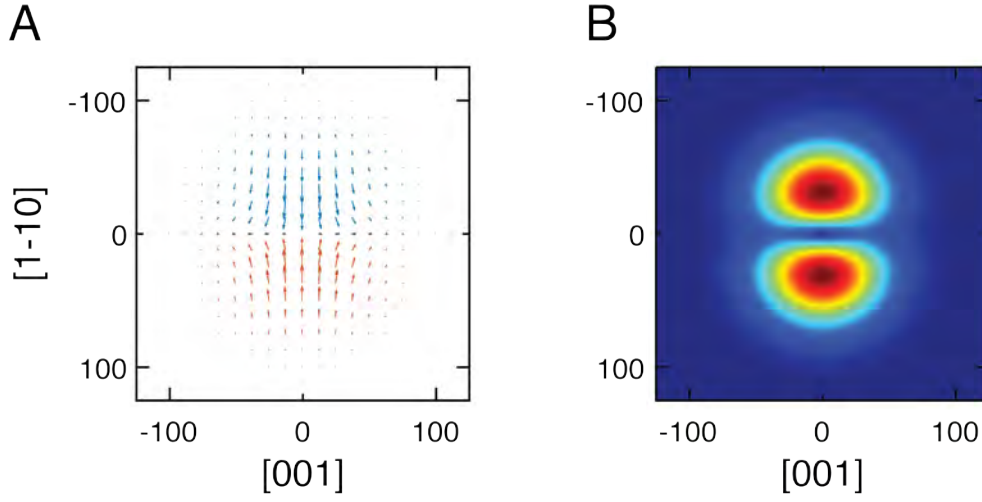


Figure 3.21: Calculated flexoelectric polarizations. (A) polarization vector field in the  $xy$ -plane. (B) polarization amplitude in the  $xy$ -plane.

cubic phase and at room temperature. Under these conditions, there are only three independent elements of the form  $f_{iiii}$ ,  $f_{iijj}$ , and  $f_{ijij} = f_{ijji}$ . The bulk flexoelectric coefficients are known to be directly proportional to the dielectric constant of a material. It is therefore possible to estimate the low-temperature flexoelectric coefficients by rescaling the values of the room-temperature cubic phase by the known changes of the dielectric function:

$$f_{ijkl}^{low-T} = \sum_m \frac{\epsilon_{im}}{\epsilon_{cubic}} f_{mjkl}^{cubic} \quad (3.16)$$

where  $\epsilon_{im}$  is the linear electric dielectric function in the low temperature phase and  $\epsilon_{cubic}$  is the susceptibility in the cubic phase. The values for  $f_{mjkl}^{cubic}$  are taken from Ref. ([141]) and the values for  $\chi_{im}$  from Ref. ([106]). The calculated flexoelectric polarization field is shown in Fig. 3.21. Two distinct domains with opposite polarizations are expected to form. Importantly, even if the gaussian strain profile is symmetric in the  $xy$ -plane, because in  $SrTiO_3$  the dielectric function is highly anisotropic [106], the resultant polarization distribution is also anisotropic.

### 3.5.1 Domain distribution

The measurements presented so far do not distinguish between the possible domain structures of Fig. 3.20. In order to determine the spatial distribution of the photo-induced polar phase two additional experiments were performed. First, the spatial distribution of the emitted second harmonic was detected with a shadow imaging setup. Second, spatially resolved electrical measurements were obtained in the same setup described in Fig. 3.18A by sliding the sample with respect to the pump.

**SHADOW IMAGING - EXPERIMENT** The second harmonic growth experiment was repeated with a now collimated<sup>12</sup> 2.2  $\mu\text{m}$  probe (1200  $\mu\text{m}$  spot size) impinging on the sample on a much larger area than the transformed region (70  $\mu\text{m}$ ). The “shadow” of the induced polar structure was detected with a CMOS camera to retain spatial information (Fig. 3.22, left). Two, distinct second harmonic sources were detected (Fig. 3.22, right), suggestive of the formation of an inhomogeneous ferroelectric phase (Fig. 3.20B). This observation can be understood as follows. The second harmonic light is emitted from the transformed area with divergence angle  $\theta \propto \frac{\lambda_{SH}}{D}$ , where  $D$  is the size of the emitter. A single domain like the one in Fig. 3.20B would act as a single source of second harmonic. The emitted light would propagate towards the detector, forming a circular far-field intensity profile known as Airy’s disc, akin to the diffraction pattern of a circular aperture. In the double domain case of Fig. 3.20B, there would be two sources of second harmonic, each roughly half the size of the excited area ( $\sim 35 \mu\text{m}$ ). Because the phase of the emitted light depends on the sign of the polarization, the two domains would generate second harmonic fields  $\pi$  phase-shifted with respect to each other. These light fields would diffract

<sup>12</sup> To compensate for a slight divergence of the incoming beam and to avoid beam clipping on the mid-infrared focusing optics, a lens with long focal length was used on the probe ( $f = 1200 \text{ mm}$ ).

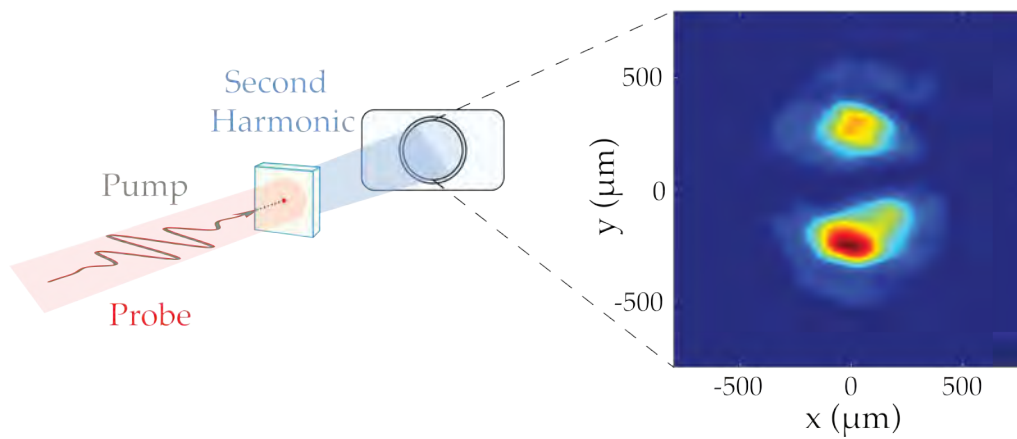


Figure 3.22: Spatial dependence of the second harmonic intensity. Left: Second harmonic shadow imaging setup. Right: second harmonic shadow image.

towards the detector partially overlapping in the central area. On the camera, the interference between the phase-shifted fields would result in a far-field image with an empty central region and intense side lobes (Fig.3.23A), consistent with the experimental observation.

**SHADOW IMAGING - SIMULATIONS** To confirm that the detected second harmonic shadow distribution arises from the interference of two anti-phase light fields, beam propagation simulations were performed following the same approach described in [37]. A  $1.1 \mu\text{m}$ -wavelength beam irradiated a structure composed of a punctured mask and two transparent slabs. These two non-absorbing, linear, dielectric materials, which bisect the beam in the direction of propagation, mimic the effect of two anti-phase domains. The material thickness was chosen so that the light propagating through one of the dielectrics would experience a  $\pi$  phase shift with respect to the other. Therefore, one dielectric had thickness  $\lambda$  while the other  $\frac{\lambda}{2}$ . The pumped area was defined by placing a  $70 \mu\text{m}$  diameter circular aperture of the dielectrics. The light propagating through this structure produced an interference pattern in agreement with the experimental

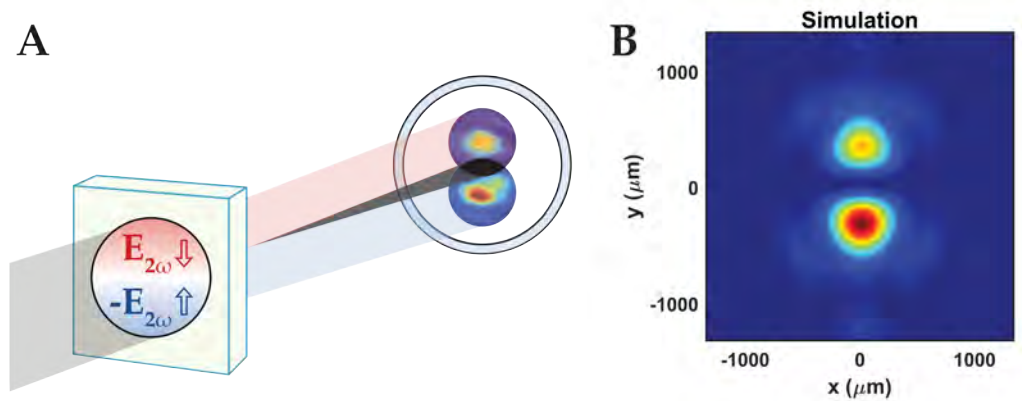


Figure 3.23: Shadow imaging interpretation and simulation. (A) Two antiphase second harmonic fields generated by a bipolar domain structure interfere destructively on the camera. (B) Simulated shadow image.

results (Fig. 3.23B)<sup>13</sup>. Note that the asymmetry in the simulated lobes arises from an artificial and unwanted offset ( $\sim 1$  micron) between the circular aperture and the boundary between the two dielectrics. It is also important to note that there is a slight discrepancy between the size of the simulated (Fig. 3.23B) and experimental (Fig. 3.22, right) patterns. However, the simulation only accounts for the linear propagation of optical beams and does not consider any nonlinear effects such as self-focusing, which might explain the observed inconsistencies.

The good agreement between experiment and simulations is supportive of the formation of a bipolar domain structure. Note, however, that the lobe slight asymmetry in the experimental data might be suggestive of a partially mixed polarization state, where the the dominant flexoelectric domains are superimposed to a much weaker ferroelectric monodomain<sup>14</sup>.

SPATIAL DEPENDENCE OF THE ELECTRICAL RESPONSE      Also the spatial dependence of the current pulses reflects the inhomogeneity of the in induced

<sup>13</sup> Note that, as in the experiment, the probe light was weakly focused with a long focal length lens,  $f = 1200$  mm, and the far-field image was sampled at  $100$  mm from the emitter.

<sup>14</sup> Needless to say, the asymmetry could also arise from an experimental artifact.

polar domains. Indeed, the amplitude and sign of the current pulses were found to strongly depend on the position of the pump beam with respect to the contacts. Current pulses of opposite sign were detected as the pump was moved towards either of the electrodes, while no current was observed when the pump spot was at equal distance from the contacts (Fig. 3.24A and B).

This observation can also be explained in the context of two oppositely oriented flexoelectric domains. The photo-induced current pulses arise from the capacitive coupling between the electrodes and each domain boundary. The relative capacitance between the top ( $C_d$ ) and bottom ( $C_u$ ) contacts is controlled by the position of the pump spot with respect to the contacts (see Fig. 3.24C). Indeed, for a bipolar domain structure, an average charge density  $+\sigma$  would form on the top and bottom boundaries. Because the domains are characterized by oppositely oriented polarizations, the boundary charge densities have the same sign. On both contacts, negative screening charges would accumulate to compensate for  $+\sigma$ . The resulting capacitance is inversely proportional to the distance  $d$  between the contact and the domain boundary, that is,  $C \propto \frac{1}{d}$ . This implies that the amount of charges on each contact depends on the distance of the domains from each electrode. When the pump spot is closer to the top contact  $C_u$  decreases while  $C_d$  increases resulting in a current flow towards the upper contact. The opposite happens for the pump closer to the bottom contact. When the domains are equally distant from the contacts, no net current is observed. By changing the pump position with respect to the electrodes, the screening charge densities and the polarity of the current can be controlled, as observed in the experiment.

Importantly, the formation of a ferroelectric monodomain, like that in Fig. 3.20A, would produce a markedly different spatial dependence. In this case, the boundary charges would have opposite sign,  $+\sigma$  on the upper half of the domain and  $-\sigma$  on the bottom half. As a consequence, the screening charges on the contacts would also have different signs. Changing the capacitances  $C_d$  and

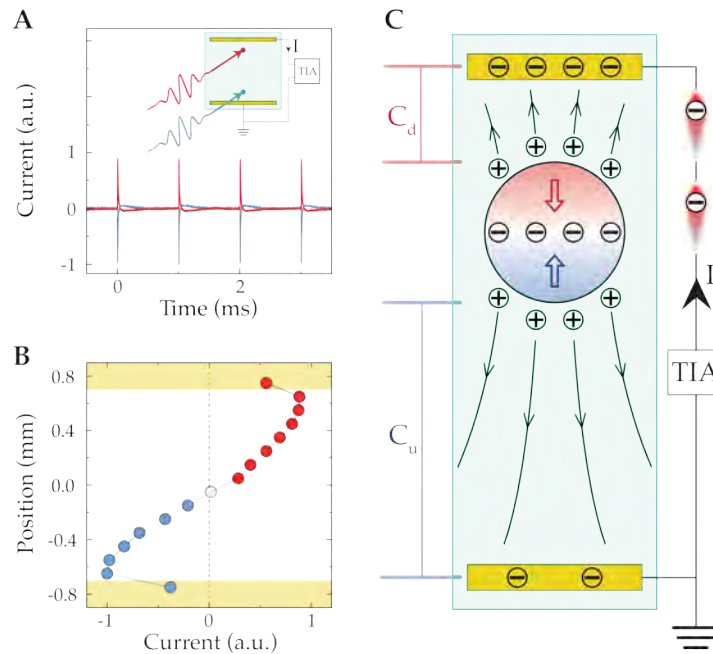


Figure 3.24: Spatial dependence of the electrical response. (A) Current pulses with different amplitudes and polarities were detected for the pump impinging closer to one of the two contacts. (B) Current pulses peak amplitude as a function of the pump position with respect to the contacts (yellow). (C) Schematic explanation of the detected current distribution. The domains position relative to the contacts determines the current amplitude and sign.

$C_u$  would only affect the magnitude of the screening charges, but it would not affect the sign of the current.

The spatial dependences of the optical and electrical measurements are fully consistent with the formation of oppositely oriented polar domains.

**ACCUMULATION AND METASTABILITY** Phonon-flexoelectricity has been identified as the plausible mechanism responsible for the formation of the observed optically-induced polarizations and domains. However, this microscopic interpretation does not explain the detected slow accumulation and metastability. In the following, some possible explanations are discussed.

The first mechanism considers the alignment of polar nano-regions (PNR). Indeed, even the purest  $SrTiO_3$  sample develops local nanometer-sized polar

clusters around defects. These PNR are randomly distributed and oriented and, as such, do not contribute to a net macroscopic polarization. An ultrafast phonon-induced flexoelectric polarization would force these preexisting PNR to align along a common direction. A single pump pulse would only result in a partial alignment because of the inherently slow PNR dynamics and the transient nature of the aligning field. Therefore, in order to grow macroscopic domains, multiple subsequent pulses would be required<sup>15</sup>. The accumulation would only occur if in between two pulses the induced partial alignment did not relax back to the unperturbed phase. Indeed, PNR are known to exhibit an extremely slow relaxation dynamics in response to an applied electric field. Piezoresponse force microscopy experiments [50] have proven that the application of an electric field on strain-free  $SrTiO_3$  can induce a ferroelectric order that spontaneously relaxes back to the paraelectric phase only on a scale of hours once the field is removed. This slow “glassy” [124] dynamics could be associated with the observed accumulation effects and metastability of the photo-induced state.

Another viable alternative accounts for the ionization of impurity centers and their slow diffusion, also known as *photorefractivity* [89]. The mid-infrared light used here could simultaneously induce strain and ionize some shallow impurity centers. Then, the flexoelectric polarizations would act as a separating field, forcing a slow diffusion of the photo-generated charges towards the edge of the transformed area, where they eventually recombine. This mechanism of spatial charge separation would result in a strong local electric field that can alter the structural and optical properties of the material. Subsequent pulses would favor the accumulation of more charges which would translate in stronger electric fields. However, conventional photorefractive effects occur for pump photon energies in the proximity of the optical gap [94]. Here, on the contrary, the second harmonic growth is maximized for pump photons in the mid-infrared while it vanishes for pump wavelengths approaching the optical gap.

*Conventional photorefractivity involves the separation of ionized impurity charges due to the intrinsic internal fields of polar materials with broken inversion symmetry.*

<sup>15</sup> At the pump repetition rate of 1 kHz, tens of thousand of pulses hit the sample every minute.

### 3.6 CONCLUSIONS

In this Chapter, I have shown how ultrafast phonon excitation can induce a structural phase transition and stabilize long-range ferroelectric correlations. Importantly, this photo-induced order was “hidden” in that it was not a spontaneously accessible phase. The resonant vibrational control of strain could lead to new opportunities for on-demand material control. Because flexoelectricity is a common material property [142], allowed by symmetry in all materials, the ability to induce ultrafast flexoelectric polarizations should be applicable in a multitude of cases. Furthermore, because  $SrTiO_3$  is routinely used as a substrate in complex heterostructures, the optical access to flexoelectric polarizations should find extensive applications in the manipulation of collective phenomena at interfaces [1, 93].

## Part III

### PHONON-DRIVEN MAGNETIZATION CONTROL



# 4

---

## PHONON-DRIVEN MAGNON EXCITATION

---

In this chapter, I generalize these ideas of nonlinear phononics and explore the simultaneous excitation of more than one lattice mode. The mixing of orthogonal, non-degenerate phonons drives rotations of the crystal-field ions, which mimic the application of a magnetic field pulse and result in the excitation of coherent magnetic oscillations in the rare-earth orthoferrite  $ErFeO_3$ . This experiment proves that nonlinear phonon excitation can control the magnetization of a material as well as its structure. More generally, this technique allows for all-optical control of the order parameter of pre-existing broken symmetry phases<sup>1</sup>.

### 4.1 THE ERBIUM ORTHOFERRITE $ErFeO_3$

$ErFeO_3$  belongs to the family of rare-earth orthoferrites ( $REFeO_3$ ). These materials are magnetic insulators known for their unusual magnetic properties, such as the coexistence of ferro- and antiferromagnetic phases and the occurrence of multiple magnetic phase transitions.

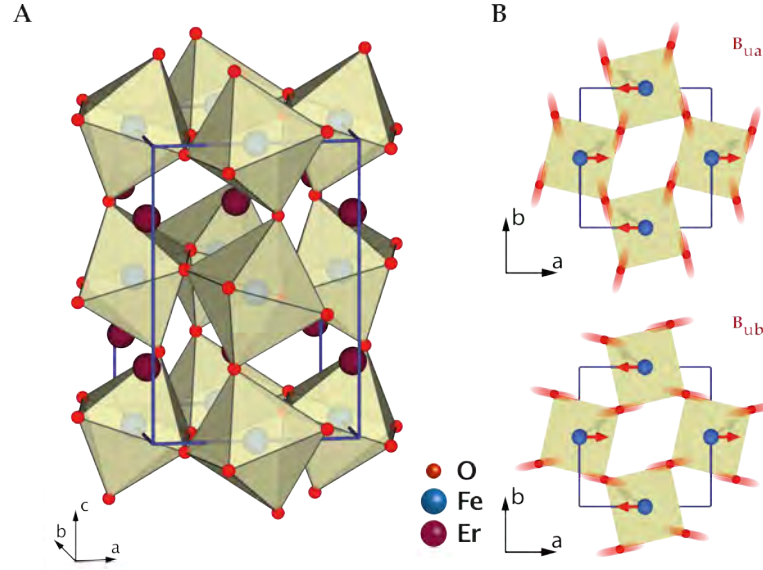


Figure 4.1: (A) Crystal structure of  $ErFeO_3$ . (B) Calculated phonon eigenvectors. The  $B_{1u}$  and the  $B_{2u}$  are polarized along the  $a$  and  $b$  crystallographic axes, respectively. The highest energy phonons are characterized by the motion of the lighter atoms, oxygen in this case.

#### 4.1.1 Crystal structure and lattice vibrations

Erbium ferrite crystallizes in an orthorhombically distorted perovskite structure [79] (space group:  $Pbnm$ ; Fig. 4.1A). There are  $N = 20$  atoms in the unit cell, resulting in  $3N = 60$  vibrational modes. At the Brillouin zone center, the irreducible representation is [53]:

$$\Gamma = 7A_{1g} + 7B_{1g} + 5B_{2g} + 5B_{3g} + 8A_{1u} + 8B_{1u} + 10B_{2u} + 10B_{3u} \quad (4.1)$$

Only the modes with symmetry  $B_{1u}$ ,  $B_{2u}$ , and  $B_{3u}$  have infrared activity (they possess a dipole moment). Because of the orthorhombic distortion, the phonons polarized along the in-plane axes are non degenerate. In particular, the two highest energy *orthogonal* modes excited in the present experiment have slightly different TO frequencies. For these phonons, polarized along the

<sup>1</sup> The experiment described in this chapter was published in [91]. Some sections were adapted from the Supplementary Materials of the same article.

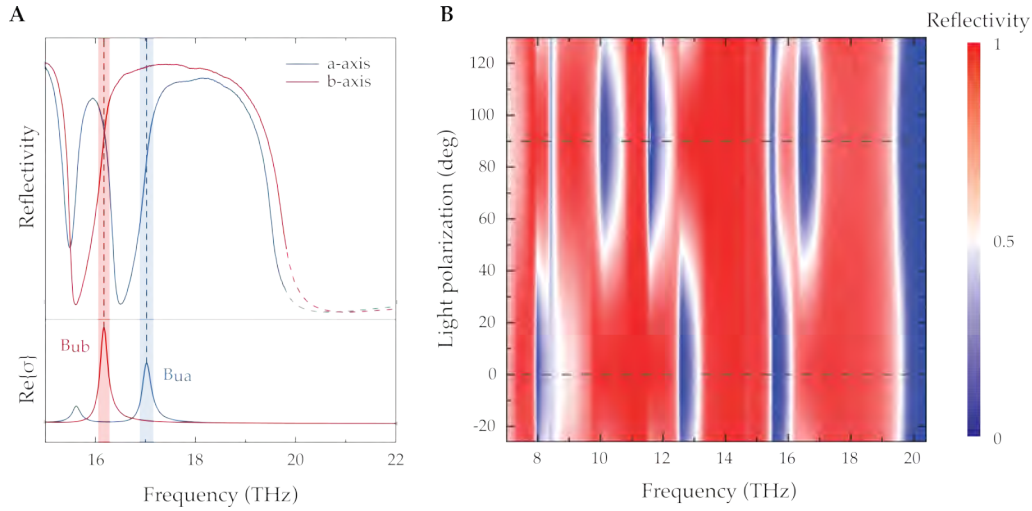


Figure 4.2:  $ErFeO_3$  reflectivity. (A) Top: reflectivity for light polarization along the  $a$  and  $b$  crystallographic axes in blue and red, respectively. Bottom: real part of the optical conductivity. The peaks identify the frequency of the TO phonon. (B) polarization dependent reflectivity.

$a$  ( $B_{3u}$  symmetry) and  $b$  ( $B_{2u}$  symmetry) crystallographic axes, the resonance frequencies are  $\omega_{B_{3u}} = 16.2$  THz and  $\omega_{B_{2u}} = 17$  THz, respectively (Fig. 4.2A). The broad ( $\sim 2$ -3 THz) high reflectivity region that starts from the TO frequency (as identified by the peak in the optical conductivity) and ends around  $\sim 19.5$  THz is the reststrahlen band of the phonon. The atomic motion associated with these vibrational modes is shown in Fig. 4.1B. As it is common for the highest-energy modes, the main contribution comes from the lighter oxygen ions.

Figure 4.2B shows a more comprehensive measurement of the polarization dependent lattice response. The 100 K spectrally resolved reflectivity, measured in a broad spectral range as a function of the polarization angle of the impinging light with respect to one crystallographic axis, highlights the effects of the orthorhombic distortion on the optical and vibrational properties of the ferrite. The phonons' TO frequency, damping and plasma frequency change as a function of light polarization. The two crystallographic axes of the material can be easily identified from this measurement (dotted lines in Figure 4.2B).

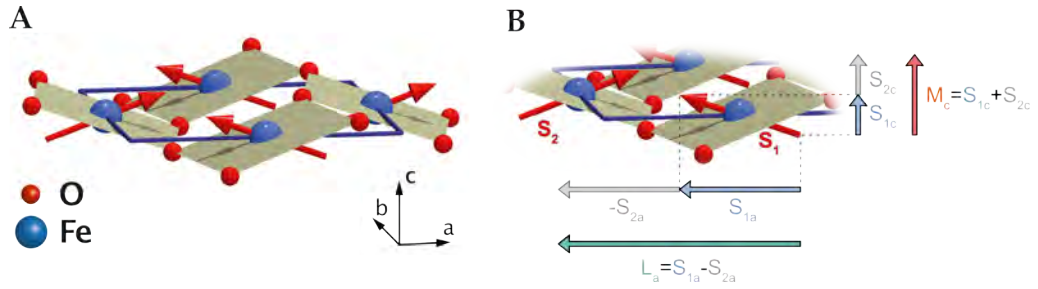


Figure 4.3: Magnetic structure. (A)  $ErFeO_3$  is a canted ferromagnet. Antiferromagnetic order in the  $ab$ -plane and small ferromagnetic moment along the  $c$  axis. (B) Illustration showing how the ferromagnetic  $M$  and antiferromagnetic  $L$  vectors can be constructed from the two spin sublattices.

#### 4.1.2 Magnetic properties

Erbium orthoferrite is an antiferromagnetic insulator that displays a variety of magnetic configurations and phase transitions. Its peculiar magnetic structure originates from the presence of two different magnetic ions, the 4f  $Er^{3+}$  and the 3d  $Fe^{3+}$  ions.

**CANTED ANTIFERROMAGNET** The first phase transition is driven by the strongest magnetic interaction in the system, that is  $Fe^{3+} - Fe^{3+}$  superexchange [127]. The iron ions order antiferromagnetically at high Neel temperatures ( $T_N = 643$  K) along the crystallographic  $a$ -axis. The high transition temperature arises from a strong nearest-neighbor exchange interaction and the large magnetic moment of iron ( $S = \frac{5}{2}$ ). The  $Fe^{3+}$  magnetic moments align in the typical G-type magnetic structure with antiferromagnetic coupling both inter-plane and intra-plane. However, due to the Dzyaloshinskii-Moriya interaction (DMI), the  $Fe^{3+}$  spins collectively tilt slightly out of the  $ab$ -plane ( $\theta < 1^\circ$ ) resulting in a small net magnetization along the  $c$ -axis (Fig. 4.3A). The small ferromagnetic moment is saturated by a 7.5 mT field [118]. The DMI, also known as antisymmetric superexchange, arises from the contribution of spin-orbit coupling to superexchange and favors spin canting. The magnetic configuration below  $T_N$  is referred to as  $\Gamma_4(L_a M_c)$ . Here,  $L = S_1 - S_2$  is the antiferromagnetic vector,

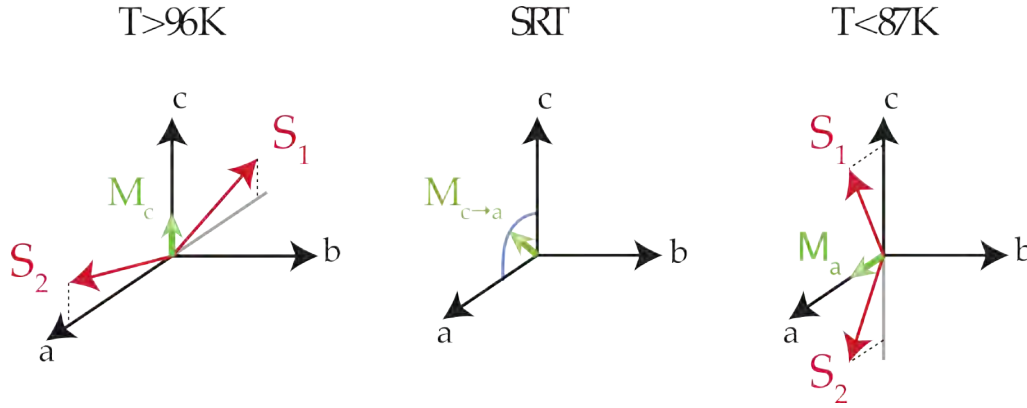


Figure 4.4: Spin reorientation transition. Due to a temperature dependent magnetic anisotropy, the spin axis continuously rotates from the  $a$  to the  $c$  axis for temperatures between 96 and 87 K.

$M = S_1 + S_2$  is the ferromagnetic vector and the indices  $a$  and  $c$  indicate the direction of the vectors (Fig. 4.3B).

**COMPENSATION TEMPERATURE** Also the erbium sublattice undergoes a phase transition, but at much lower temperature. The interaction among the rare-earth ions is rather weak and results in an ordering only below  $\sim 4$  K [12, 59]. Above this temperature, the rare-earth sublattice is paramagnetic. However, the  $Er^{3+}$  ions develop a small magnetic moment due to an antiferromagnetic superexchange coupling with the neighboring  $Fe^{3+}$  sublattice. While this interaction is negligible at high temperatures ( $>100$  K), the erbium magnetization becomes comparable to the magnetization of the iron ions with decreasing temperatures. In  $ErFeO_3$  there exists a compensation point [129] where the magnetizations of the two magnetic ions are of equal magnitude but opposite sign. At this temperature [51],  $T_{comp} \sim 47$  K, the total ferromagnetic moment vanishes.

**SPIN REORIENTATION TRANSITION** At intermediate temperatures ( $87$  K  $< T < 96$  K), the material undergoes a spin reorientation transition (SRT) where the spin axis gradually rotates from the  $a$ -axis to the  $c$ -axis [6, 127, 131]. The

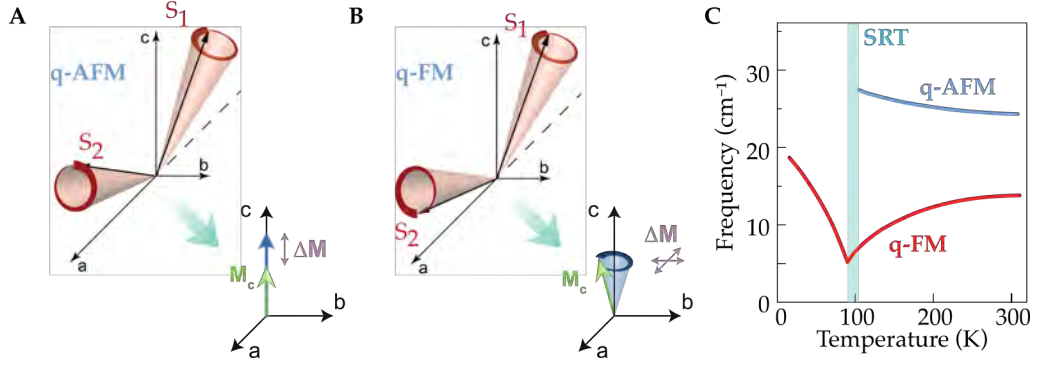


Figure 4.5: Magnon branches. (A) Spin motion associated with the quasi-antiferromagnetic magnon (q-AFM). The magnitude of the ferromagnetic moment  $M$  oscillates at the magnon frequency. (B) Quasi-ferromagnetic (q-FM) magnon. The vector  $M$  precesses around the  $c$ - (above the SRT) or the  $a$ - (below the SRT) axis. (C) Magnon frequency as a function of temperature (adapted from [67]).

SRT changes the magnetic configuration from  $\Gamma_4(L_a M_c)$  to  $\Gamma_2(L_c M_a)$  via an intermediate phase  $\Gamma_{42}(L_{ac} M_{ca})$ . At each boundary between different configurations, that is  $\Gamma_4 \rightarrow \Gamma_{42}$  and  $\Gamma_{42} \rightarrow \Gamma_2$ , the spin system undergoes a second order phase transition.

The SRT originates from the different temperature dependence of the magnetic anisotropies [132]: the  $Fe^{3+}$  single ion anisotropy and the  $Fe^{3+} - Er^{3+}$  antisymmetric superexchange interaction. The former dominates at high temperatures, favoring the  $\Gamma_4$  configuration. The latter is strongly affected by the electronic properties of the erbium ion and favors the  $\Gamma_2$  magnetic configuration. While the single ion anisotropy remains constant with decreasing temperature, the anisotropic superexchange varies significantly. This phenomenon is due to a temperature-driven electronic redistribution in the erbium ions, which affects the  $Fe^{3+} - Er^{3+}$  interaction and results in a modification of the magnetic anisotropy. The interplay between the two anisotropies is responsible for the change in easy axis and the SRT.

MAGNON BRANCHES The magnetic structure and the spin waves in erbium orthoferrite can be described in terms of a two-sublattice model [62]:

$$U_{spin} = J (\vec{S}_1 \cdot \vec{S}_2) + \vec{D} \cdot (\vec{S}_1 \times \vec{S}_2) + K_x (S_{1x}^2 + S_{2x}^2) + K_z (S_{1z}^2 + S_{2z}^2) + K_4 (S_{1x}^4 + S_{1y}^4 + S_{1z}^4 + S_{2x}^4 + S_{2y}^4 + S_{2z}^4) \quad (4.2)$$

where  $S_1$  and  $S_2$  are the spin vectors that identify each sublattice,  $K_x$ ,  $K_z$  are second-order magnetocrystalline anisotropy constants while  $K_4$  is fourth-order<sup>2</sup>,  $J$  and  $D$  are the nearest-neighbor isotropic and antisymmetric (Dzyaloshinskii-Moriya) exchange constants, respectively.

The model in Eq. 4.2 predicts two spin-wave branches [128]: the quasi-antiferromagnetic ( $q$ -AFM) and the quasi-ferromagnetic ( $q$ -FM) modes:

$$\begin{aligned} \hbar\omega_{q-AFM} &= \sqrt{24JS [6DS \tan(\theta) + 2K_x S]} \\ \hbar\omega_{q-FM} &= \sqrt{24JS [2(K_x - K_z) S]} \end{aligned} \quad (4.3)$$

where  $\theta$  is the canting angle. The spin precession in the  $q$ -AFM mode is associated with an amplitude modulation of the ferromagnetic moment (Figure 4.5A). In the  $q$ -FM mode (Fig. 4.5B), the ferromagnetic moment precesses about the spin axis, that is, the  $c$ -axis for temperatures higher than the SRT and the  $a$ -axis for temperatures lower than the SRT. Because the coupling between the iron ions is mostly antiferromagnetic, the magnon frequencies are particularly high, approaching the terahertz range [67]. However, while the exchange constants  $J$  and  $D$  are temperature independent, the second-order magnetocrystalline anisotropy constants  $K_x$  and  $K_z$  are not (they are indeed responsible for the SRT). As a result, the magnon frequencies change significantly with temperature (Fig. 4.5C). In particular, the  $q$ -FM acts as the soft-mode of the SRT, approaching

<sup>2</sup> Note that the fourth-order anisotropy constant is necessary to correctly describe the SRT. This small term allows for the continuous rotation of the spins in the  $ab$  plane.

zero frequency at one of the two transition temperatures. A more accurate four-sublattice model that accounts for multiple, slightly different coupling and anisotropy constants leads to the same results.

**DOMAINS** While the exchange interaction dominates at short length scales, the magnetic dipole-dipole interaction - which favors antiparallel alignment - takes over at macroscopic length scales. The interplay between these two tendencies leads to the formation of magnetic domains in ferromagnetic crystals. Rare-earth orthoferrites spontaneously form magnetic stripe domains [68]. However, the formation of cylindrical domains can be stimulated by the application of an external magnetic field. Owing to the large magnetic anisotropy and the small saturation magnetization, the domains are as big as hundreds of microns [105] or, in some cases, even millimeters [119]. Because of the large size of the domains compared to the pump spot size, during the optical experiments reported here the material could be considered in a monodomain state.

#### 4.1.3 *Magneto-optics*

**NEAR-INFRARED - ELECTRONIC TRANSITIONS** Erbium orthoferrite is a charge transfer insulator [98], transparent at photon energies smaller than the optical gap ( $\sim 2.5$  eV). The absorption spectrum at below-gap wavelengths, while still remaining pretty low (in the tens of  $cm^{-1}$  range), is dominated by the iron ion optical transitions [120].  $Fe^{3+}$  contains five 3d electrons in a high-spin state. Optical crystal-field d-d transitions from the iron ground state are forbidden by spin and parity selection rules. However, due to different structural and electronic perturbations these transitions can still be weakly active. In  $ErFeO_3$ , there are two main below-gap absorption bands centered around  $\sim 1.2$  eV and  $\sim 1.7$  eV which arise from the  ${}^6A_{1g} \rightarrow {}^4T_{1g}$  and  ${}^6A_{1g} \rightarrow {}^4T_{2g}$

ionic transitions, respectively. Such transitions are spectrally broadened by strong electron-phonon coupling.

Unlike the  $Fe^{3+}$  optical activity, the transitions of the erbium ions are much weaker and sharper. Indeed, 4f electrons are significantly more isolated from the environment as compared to the 3d electrons and, as such, they are only weakly affected by the lattice. In the case of erbium orthoferrite the coupling between the 4f erbium electrons and phonons is particularly weak, resulting in narrow lines. Nevertheless, crystal field and magnetic interactions split the weakly active transitions from the erbium  $^4I_{15/2}$  ground state[129].

For photon energies above the gap, the material absorption becomes significant and is characterized by multiple charge transfer transitions. Due to the structural deformations described in Sec. 4.1.1, rare-earth orthoferrites are moderately birefringent.

The strong magneto-optical activity in  $ErFeO_3$  arises predominantly from the  $Fe^{3+}$  transitions[83]. For this reason, the Faraday rotation - the polarization rotation of a linearly polarized beam propagating through a magnetized medium - is sensitive to the magnetic ordering of iron ions alone. In the experiment presented here, this effect will be exploited to probe the pump-induced magnetization dynamics on ultrafast timescales.

**FARADAY EFFECT** Because erbium orthoferrites exhibit strong optomagnetic coupling and low absorption in the near-infrared frequency range, the material is an ideal candidate for the study of ultrafast magnetization measurements in transmission.

The rotation of the plane of polarization of light propagating through a magnetized medium is known as the Faraday effect [25]. This property is often exploited to measure the magnetization of a material with optics, statically or on ultrafast timescales. In cubic ferromagnets and ferrimagnets, the polarization

rotation is proportional to the projection of the magnetization  $M$  along the propagation direction of light (identified by the unit vector  $\hat{k}$ ):

$$\theta_F \propto \vec{M} \cdot \hat{k} \quad (4.4)$$

This phenomenon can be understood by describing the interaction between light and matter in a magnetic material with the dielectric permittivity tensor  $\varepsilon$ :

$$\varepsilon = \begin{pmatrix} \varepsilon_{xx} & i\varepsilon_{xy} & 0 \\ -i\varepsilon_{xy} & \varepsilon_{yy} & 0 \\ 0 & 0 & \varepsilon_{zz} \end{pmatrix} \quad (4.5)$$

Note that the light is considered to propagate along the  $z$  direction. The on-diagonal terms account for the dielectric properties of the material, while the off-diagonal terms describe the Faraday effect. In isotropic media ( $\varepsilon_{xx} = \varepsilon_{yy}$ ), the tensor 4.5 can be diagonalized to obtain as eigenvectors left- and right-handed circularly polarized fields. In other words, a linearly polarized light field can be regarded as the linear superposition of two circularly polarized fields of opposite handedness but equal amplitude. Because these two waves interact differently with the magnetic system, they experience different dielectric permittivities and refraction coefficients,  $n_{Right} = \sqrt{(\varepsilon_{xx} - \varepsilon_{xy})}$  and  $n_{Left} = \sqrt{(\varepsilon_{xx} + \varepsilon_{xy})}$ . The difference in propagation speed results in a phase shift between the waves that translates into a rotation of the light polarization.

Despite the comparatively small ferromagnetic moment, the magneto-optic properties of rare-earth orthoferrites in the transparency region, are unusually big. This particularly strong magneto-optic coupling arises from the fact that in weak ferromagnets both the magnetization  $M$  and the antiferromagnetic

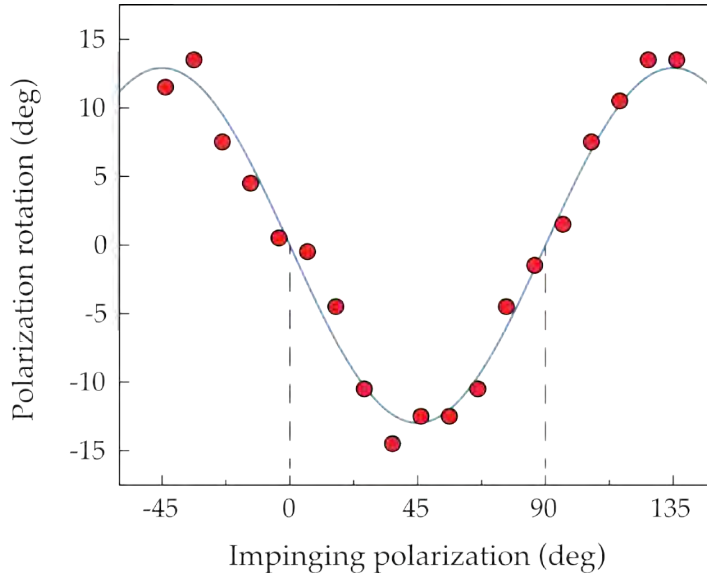


Figure 4.6: Static room-temperature birefringence of  $ErFeO_3$ . A half waveplate and a polarizer were used to define the incoming light polarization. The light transmitted by the sample was then passing through a second polarizer, and hit a detector. For each orientation of the first polarizer, the second polarizer was rotated to maximize the intensity on the detector.

vector  $L$  can contribute to the Faraday rotation [29]. In orthoferrites, the Faraday rotation takes the form:

$$\theta_F = (\alpha \vec{M} + \beta \vec{L}) \cdot \hat{k} \quad (4.6)$$

By symmetry, the tensors  $\alpha$  and  $\beta$  are:

$$\alpha = \begin{pmatrix} \alpha_{xx} & 0 & 0 \\ 0 & \alpha_{yy} & 0 \\ 0 & 0 & \alpha_{zz} \end{pmatrix}, \quad \beta = \begin{pmatrix} 0 & 0 & \beta_{xz} \\ 0 & 0 & 0 \\ \beta_{zx} & 0 & 0 \end{pmatrix} \quad (4.7)$$

Eq. 4.6 implies that even spin components orthogonal to the propagation of light might contribute to the total polarization rotation. As a matter of fact, in orthoferrites the antiferromagnetic contribution is often significantly higher than the ferromagnetic one [136]. Nevertheless, because of the tensors of Eq. 4.7, the

Faraday signal is still maximized when the light propagates in the direction of the magnetization  $\vec{M}$ .

It is important to note that in the presence of an external magnetic field  $\vec{H}$ , a paramagnetic term  $+\gamma\vec{H}$  should be added to Eq. 4.6. However, the tensor  $\gamma$  is rather small and its contribution is usually negligible compared to the ferromagnetic and antiferromagnetic components.

**BIREFRINGENCE CONSIDERATIONS** So far, in describing the optomagnetic properties of  $ErFeO_3$  the effects of birefringence have been neglected. However, for light propagating through an anisotropic medium such as orthoferrites, this contribution must be considered. From Eq. 4.5 one can see that when  $\epsilon_{xx} \neq \epsilon_{yy}$ , even in the absence of the Faraday effect, a light field linearly polarized in the  $xy$ -plane can experience a polarization change, which oscillate between linear and elliptical as a function of propagation length. Because of this oscillating behavior, the total polarization rotation also depends on the sample thickness. In the particular case of  $ErFeO_3$ , the polarization state of the transmitted light is affected by both magnetic and dielectric contributions. For these reasons, in birefringent media there is no trivial relationship that relates the magnetization and the amount of polarization rotation. However, the linear proportionality between  $\theta_F$  and  $M$  can be assured [130] for small angles  $\theta_F$  and provided that the polarization of the incoming light is directed along one of the crystallographic axes<sup>3</sup>.

In the present experiment, the in-plane sample orientation was determined by measuring its static birefringence at room temperature (Fig. 4.6). The crystallographic axes can be identified by the orientations in which the birefringence is zero, i.e. the light polarization is not altered by the transmission through the sample. All the ultrafast measurements presented in the chapter were performed

<sup>3</sup> Also the sample thickness plays a role in ensuring the linear proportionality between magnetization and polarization rotation.

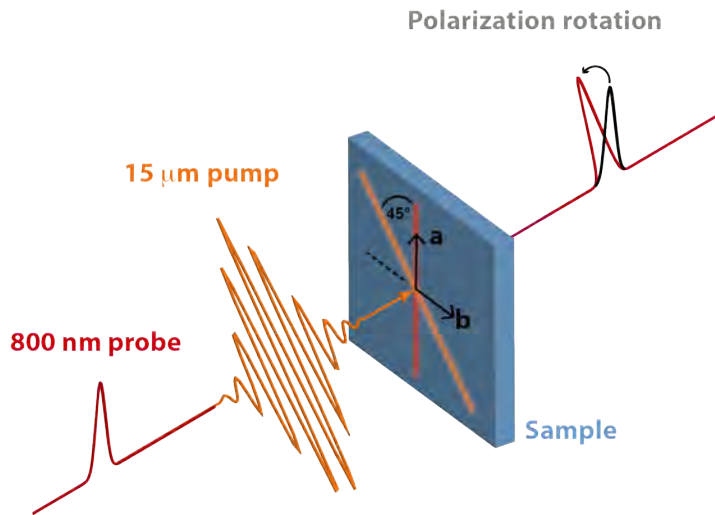


Figure 4.7: Experimental setup. The sample was excited with 20 THz pulses. The induced ultrafast dynamics was probed by looking at the polarization rotation of a linearly-polarized 800 nm-wavelength beam.

with the probe light oriented along one of the crystallographic axes to reduce the contribution of birefringence to the polarization rotation signal.

#### 4.2 EXPERIMENTAL OBSERVATION OF PHONON-DRIVEN EFFECTIVE MAGNETIC FIELDS

Intense linearly polarized mid-infrared light pulses were tuned into resonance ( $15 \mu\text{m}$ ,  $20 \text{ THz}$ ) with the highest-energy vibrational modes to drive the ferrite out of equilibrium. The pump spectral bandwidth ( $\sim 4 \text{ THz}$ ) was chosen in such a way that both in-plane infrared phonons,  $B_{ua}$  and  $B_{ub}$ , could be excited simultaneously. By rotating the pump polarization at different angles with respect to the in-plane crystallographic axes, these different phonons could be selectively excited. When the pump was polarized along the  $a$  ( $b$ ) crystallographic axis only the  $B_{ua}$  ( $B_{ub}$ ) mode was driven. However, for pump polarizations at a  $45^\circ$  angle from either axes both phonons could be simultaneously excited (Fig. 4.7). To probe the pump-induced dynamics, the polarization rotation of a linearly po-

larized near-infrared pulse (800-nm wavelength) was measured in transmission geometry. Changes in the polarization state of the probe can arise from both birefringence and Faraday effects, making our detection particularly sensitive to coherent phonon and magnon dynamics. During all the measurements the sample was kept in an external magnetic field to assure that only a single domain was sampled.

At 100 K, upon simultaneous excitation of both infrared phonons, the probe polarization was found to oscillate as a function of pump-probe delay at the frequency of multiple Raman-active modes (Fig. 4.8A). The oscillations at 3.36 THz and 4.85 THz correspond to Raman phonons of  $A_{1g} + B_{1g}$  and  $B_{1g}$  symmetry, respectively [67] (Fig. 4.8B). The inelastic excitation of these modes can be understood in the framework of nonlinear phononics, where the coupling term is:  $Q_{IR,ua} \cdot Q_{IR,ub} \cdot Q_{R,A_{1g}+B_{1g}/B_{1g}}$ . However, a third mode was detected at much lower frequency than any of the material's phonons (Fig. 4.8B). This oscillation has a magnetic origin and corresponds to the coherent spin motion of the quasi-antiferromagnetic mode [67] (Fig. 4.5A), associated with an amplitude modulation of the magnetization ( $M_c$ ). In the following, the dependence of this coherent magnon on various excitation conditions will be investigated in order to identify the driving mechanism.

**POLARIZATION, MAGNETIC FIELD AND FLUENCE DEPENDENCE** The coherent spin wave was detected when both phonons were simultaneously excited, that is, for pump polarizations at 45 degrees with respect to the  $a$  and  $b$  crystallographic axes (Fig. 4.9A, red). However, when only one infrared phonon was excited, that is with the pump polarization aligned with either one of the two crystallographic axes, only Raman phonons were observed (Fig. 4.9A, blue). This implies that pairs of orthogonal phonons are needed to trigger the magnetic response. Furthermore, the magnon phase was found to be controlled by the initial relative phase among the driven phonons. Indeed, when the pump polar-

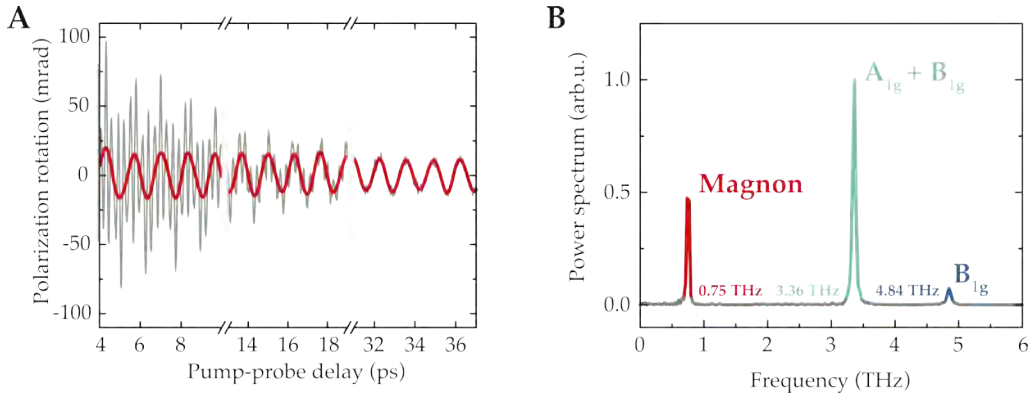


Figure 4.8: Pump-induced dynamics. (A) Polarization rotation as a function of pump-probe delay. The slow, incoherent dynamics has been removed. The oscillations due to coherent phonons (grey) can be filtered out by a low-pass filter (1.5 THz cutoff). The remaining oscillation (red) correspond to the quasi-antiferromagnetic magnon. These measurements were obtained at a pump fluence of  $17.6 \frac{\text{mJ}}{\text{cm}^2}$ . (B) Fourier spectrum of the pump-induced dynamics. Three Raman-active modes can be observed: 0.75 THz, quasi-antiferromagnetic (q-AFM) magnon (red), and 3.36 THz and 4.85 THz, Raman phonons of  $A_{1g} + B_{1g}$  (green) and  $B_{1g}$  (blue) symmetry, respectively.

ization was rotated from  $+45 (B_{ub} + B_{ua})$  to  $-45 (B_{ub} - B_{ua})$  degrees, the magnon oscillations switched sign (Fig. 4.9A, orange). This observation suggests that the initial impulsive perturbation that triggers the spin motion depends directly on the phonons' phase (Fig. 4.9A, right).

Furthermore, important information on the underlying spin-phonon coupling could be retrieved from the magnon dependence on an external magnetic field. The initial orientation of the spins could be controlled by applying a small static external field (Fig. 4.9B, right). Experiments showed that the magnon phase, that is, the direction of the initial magnetization change, was not affected by a reversal of the static magnetization (Fig. 4.9B). Hence, the impulsive perturbation on the magnetic system is independent on the initial spin direction.

Finally, the magnon amplitude was found to scale quadratically with the pump electric field (Fig. 4.9C). Because the phonon amplitude is directly proportional to the driving field ( $Q_{IR} \propto E_{\text{pump}}$ ), a quadratic dependence suggests that the magnetic excitation depends on the product of two phonon coordinates ( $\propto Q_{IR,i}Q_{IR,j}$ ).

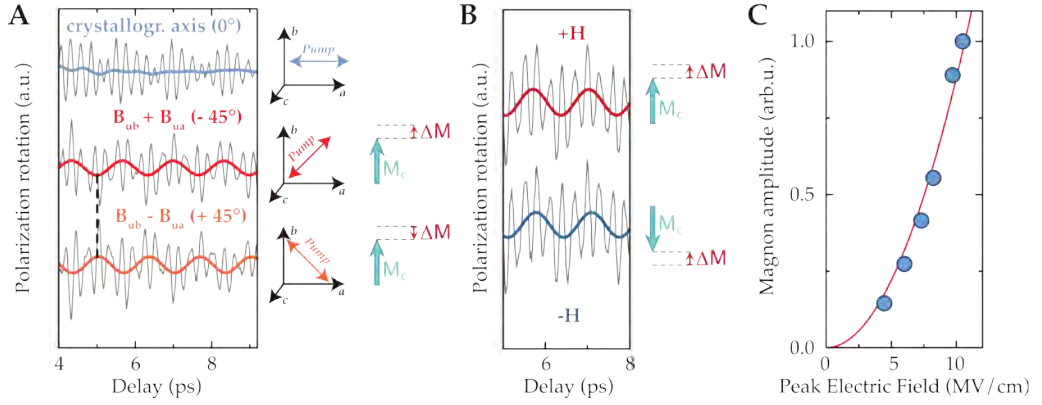


Figure 4.9: (A) Induced dynamics for different pump polarizations (grey). The color lines highlight the magnon oscillations (when present). Blue: while the pump polarization is aligned along one crystallographic axis, no magnon oscillation was detected. Red: when the two orthogonal phonons were excited with the same initial phase ( $B_{ub} + B_{ua}$ ) both Raman phonons and magnon oscillations were observed. Orange: when the two vibrational modes were driven with opposite phases ( $B_{ub} - B_{ua}$ ) the magnon phase changed sign. (B) Magnon dependence on an external magnetic field. The initial orientation of the spins did not affect the magnon phase. (C) magnon amplitude as a function of pump field.

**WAVELENGTH DEPENDENCE** To confirm the vibrational origin of the effect, the same experiment was repeated for different pump photon energies. The magnon amplitude was found to be maximum for wavelengths near the LO mode, that is where the dielectric function crosses zero (19.6 THz; Fig. 4.10A). To retrieve the corresponding magnetization change one has to take into account the penetration-depth mismatch between the pump and the probe. Indeed, while the probe is fully transmitted by the sample (constant probed volume), the penetration depth of the pump (and therefore the pumped volume) is strongly wavelength dependent, due to the proximity to a resonance. Therefore, the pump-induced relative magnetization change was computed as the ratio:

$$\frac{\Delta M}{M} = \frac{\left(\frac{\Delta\theta_F}{l_p}\right)}{\left(\frac{\theta_F}{L_S}\right)} \cdot 100 \quad (4.8)$$

where  $\Delta\theta_F$  and  $\theta_F$  are the pump-induced and static Faraday rotations, respectively,  $l_p$  is the pump penetration depth retrieved from reflectivity measurements

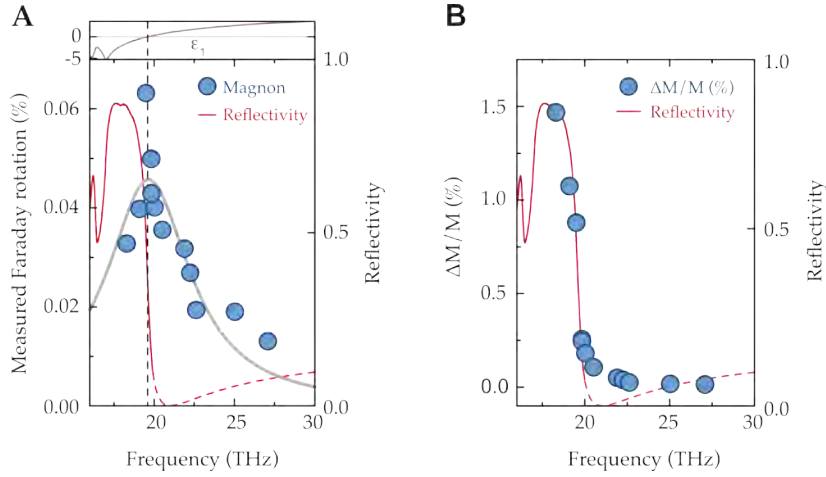


Figure 4.10: Wavelength dependence. (A) magnon amplitude as a function of pump wavelength (dots). The data is compared to the static reflectivity (red line) and real part of the dielectric function of the material (purple line). The dotted black line highlights the zero-crossing of the real part of the dielectric function. The grey line constitutes a guide to the eye. All measurements were taken at a constant fluence of  $20 \frac{\text{mJ}}{\text{cm}^2}$ . (B) Retrieved total magnetization change. The pump-probe penetration-depth mismatch was taken into account to estimate the absolute change of magnetization.

and  $L_S$  is the sample thickness. The maximum precession amplitude was found to be approximately 1.5% of the saturation magnetization (Fig. 4.10B). These observations confirm that the spin precession is driven by the optically-driven phonons.

**AN EFFECTIVE MAGNETIC FIELD** The experimental evidence so far reported are consistent with the formation of a phonon-driven directional magnetic field pulse. Because the excited spin wave is the q-AFM mode, the phonon-induced magnetic field must be orthogonal to the antiferromagnetic vector  $L$ . Moreover, any phenomenological description of the observed spin-phonon coupling must depend on pairs of phonons, must be independent on the preexisting magneti-

zation and must scale quadratically with the phonon field. By symmetry, the lowest-order Hamiltonian consistent with the above observations is:

$$U_{spin-phonon} = i\alpha_{abc}Q_{ua}Q_{ub}^*M_c \quad (4.9)$$

where  $\alpha_{ijk}$  is the magneto-elastic susceptibility,  $Q_{ua}$  and  $Q_{ub}^*$  are the phonon eigenvectors and  $M_c$  is the static magnetization.  $\alpha_{ijk}$  is an axial third rank tensor, antisymmetric over the first pair of indices  $\alpha_{ijk} = -\alpha_{jik}$ . For the crystallographic point group of the crystal,  $\alpha_{ijk}$  has 6 independent components ( $\alpha_{xyz}, \alpha_{xzy}, \alpha_{zxy}, \alpha_{yxz}, \alpha_{yzx}, \alpha_{zyx}$ ). Because the effect studied in this work only depends on the antisymmetric part of the tensor and because the pump propagates along the z-axis, the explicit form of the tensor is:

$$\alpha = \begin{bmatrix} 0 & \alpha_{abc} & 0 \\ -\alpha_{abc} & 0 & 0 \\ 0 & 0 & 0 \end{bmatrix} \quad (4.10)$$

Importantly, the tensor  $\alpha_{ijk}$  does not depend on the magnetization (i.e. magnetic point group). Eq. 4.9 can be rewritten in a more intuitive, vectorial form:

$$U_{spin-phonon} \propto \left[ \vec{Q}_{tot} \times \frac{\partial \vec{Q}_{tot}}{\partial t} \right] \vec{M}_c \quad (4.11)$$

where  $\vec{Q}_{tot} = Q_{ua}\hat{a} + Q_{ub}\hat{b}$  is the total phononic field ( $\hat{a}$  and  $\hat{b}$  are unit vectors aligned with the crystallographic axes). Eq. 4.11 describes the interaction of pairs of infrared phonons with the material magnetization. The lattice motion results in an effective magnetic field:

$$H_{eff} = -\frac{\partial U_{spin-phonon}}{\partial M_c} \propto -\left[ \vec{Q}_{tot} \times \frac{\partial \vec{Q}_{tot}}{\partial t} \right]_c \quad (4.12)$$

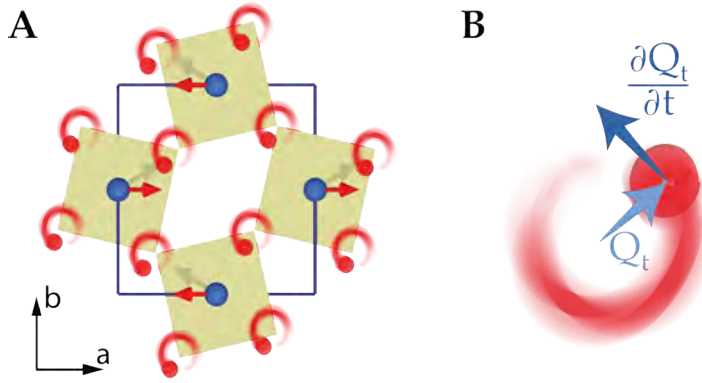


Figure 4.11: Circularly polarized phonons. Due to the non-degenerate nature of the driven vibrational modes, the ionic motion results in an elliptically polarized phononic field.

directed along the  $c$ -axis. Importantly,  $H_{eff}$  is a measure of the angular momentum of the phononic field (Fig. 4.11B) and it is nonzero only if the phonons are elliptically polarized. In this case, the sign of the field (and of the angular momentum) depends on the rotation direction of the ions. Note that Eq. 4.11 is reminiscent of the inverse Faraday effect, which arises from the electronic Raman scattering of magnons by circularly polarized light [30, 63, 97].

**CIRCULAR PHONONS FROM LINEARLY POLARIZED LIGHT** Because the pump field was linearly polarized, one could expect that the driven phononic field acquires the same polarization resulting in a zero effective magnetic field, in contrast to the experimental evidence. However, because of the orthorhombic distortion the driven infrared-active modes are non-degenerate, i.e. they have different oscillator frequencies and strengths. Therefore, even when simultaneously excited, the two orthogonal modes oscillate with a time-dependent relative phase resulting in an elliptical lattice polarization (Fig. 4.11A). Such time-reversal symmetry breaking ionic motion creates an effective magnetic field pulse orthogonal to the rotation plane ( $ab$ -plane in our case), as described by Eq.4.12.

PHONON-POLARITON SIMULATION A more quantitative analysis of the angular momentum that the phonons develop due to the orthorhombic distortion, can be obtained by solving Maxwell's equations in time and space with a one-dimensional finite difference time domain method (1D-FDTD) [114]. The space and time discretization were chosen in such a way that, in absence of free charges and currents, the divergence equations

$$\begin{aligned}\nabla \cdot \vec{D} &= 0 \\ \nabla \cdot \vec{H} &= 0\end{aligned}\tag{4.13}$$

were intrinsically satisfied (Yee grid [135]). On the other hand, the curl equations

$$\begin{aligned}\nabla \times \vec{E} &= -\mu \frac{\partial \vec{H}}{\partial t} \\ \nabla \times \vec{H} &= \varepsilon \frac{\partial \vec{D}}{\partial t}\end{aligned}\tag{4.14}$$

were explicitly solved by approximating the time and space derivatives with finite differences<sup>4</sup>. The optical properties of  $ErFeO_3$  can be reproduced by integrating the Lorentz model in the constitutive equation  $\vec{D} = \varepsilon_0 \varepsilon_r \vec{E}$ . As discussed in Chapter 2, the dielectric function  $\varepsilon_r$  is expressed as a series of damped harmonic oscillators corresponding to the infrared-active phonons:

$$\varepsilon_r = \varepsilon_\infty + \sum_k \frac{\omega_{p,k}^2}{\omega_{0,k}^2 - \omega^2 + i\omega\Gamma_k}\tag{4.15}$$

The values of the plasma frequency  $\omega_p$ , the TO frequency  $\omega_0$  and the damping  $\Gamma$  for each of the  $k$  phonons were extracted from a Lorentz fit to the static reflectivity measurements (Fig.4.2), while  $\varepsilon_\infty$  was obtained from the literature

<sup>4</sup> A detailed explanation of the simulations can be found in [17]

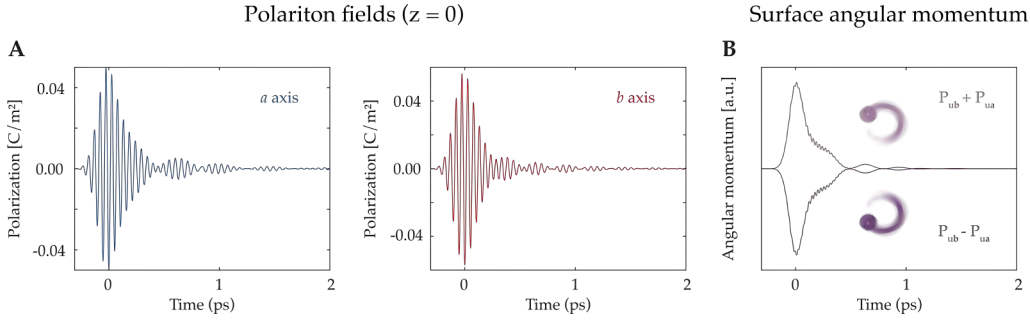


Figure 4.12: Calculated polariton dynamics at the surface. (A) Pump-driven polarizations along the  $a$ - (blue line) and  $b$ -axis (red line). In the simulations, the phonon-polariton response is initiated by a  $\frac{MV}{cm}$  amplitude, 19.5 THz central frequency and 130 fs long pump pulse. (B) Calculated angular momentum of the total phonon-polariton field. Even when simultaneously excited, the optical phonons respond with different initial phases and oscillate at different frequencies resulting in an elliptical polarization. The rotation direction and, as a consequence, the sign of the effective field can be controlled by the initial phase of the infrared-active phonons (light and dark purple).

([98]). The magnetic field constitutive equation is  $\vec{B} = \mu_0 \vec{H}$ . The time- and space-dependent lattice polarization inside the sample was calculated as:

$$\vec{P} = \epsilon_0 \sum_k \frac{\omega_{p,k}^2}{\omega_{0,k}^2 - \omega^2 + i\omega\Gamma_k} \vec{E} \quad (4.16)$$

In order to simulate the vibrational dynamics driven by pump pulse polarized at  $45^\circ$ , the calculations were performed twice, one for each crystallographic axes (Fig. 4.12A). The simulated polarizations along  $a$  and  $b$  axes were then combined to obtain the total lattice response:  $\vec{P}_{tot} = \vec{P}_a + \vec{P}_b$ .

#### ON THE RELATIONSHIP BETWEEN POLARIZATION AND DISPLACEMENT

Our simulations allow to reconstruct the behavior of the lattice polarization in space and time. However, the relevant quantity to compute the effective magnetic field is the total phononic displacement. Indeed, the polarization along each axis can be expressed as a function of the displacement of each ion  $q$  [138]:

$$P_a(x, t) = \frac{e}{L_a} \sum_i Z_i^* q_i(x, t) \quad (4.17)$$

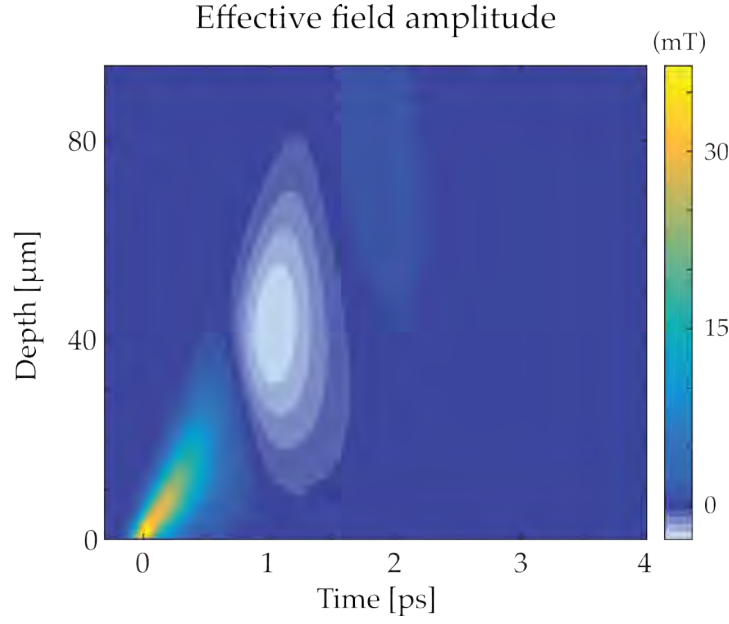


Figure 4.13: Effective field dynamics. The pair of propagating phonon-polaritons generates a time- and space-dependent effective magnetic field. Due to the dephasing of the two modes the rotational motion changes direction at around one picosecond when, however, the phonon amplitude has already decayed significantly.

where  $e$  is the electronic charge,  $L_a$  is the unit cell size,  $Z_i^*$  is the Born effective charge and  $i$  goes over the 20 atoms of the unit cell. While the effective charge for each ion is unknown, one can safely assume that the most significant displacements come from the oxygen atoms due to their lighter atomic masses as compared to the erbium and iron ions. This is a reasonable approximation especially for the higher energy phonons of Fig. 4.1B. Furthermore, one has to consider that all the oxygen atoms involved in the dynamics equally contribute to the total polarization, i.e. they exhibit the same effective charge. Under these conditions, the polarization becomes:

$$P_a(x, t) = \frac{n Z_O^* e}{L_a} q_O(x, t) \quad (4.18)$$

that is, the lattice polarization is directly proportional to the atomic displacement (bar a constant). As such, the above calculations represent an accurate estimate

of the phononic displacement field:  $\vec{Q}_{tot} = \vec{Q}_{ua} + \vec{Q}_{ub} \propto \vec{P}_{tot}$ . Fig. 4.12B shows the time-dependent effective field at the material surface retrieved<sup>5</sup> from the calculated total polarization using Eq.4.12. Upon simultaneous excitation of pairs of infrared phonons with linearly polarized light, a pulse of angular momentum develops at the surface of the material, confirming the rotational motion of the ions. As mentioned in Chapter 2, the light-lattice coupling results in the formation of phonon-polaritons. In this case, the circularly polarized phononic field, which carries an effective magnetic field, propagates into the material at 13% of the speed of light ( $0.4 \times 10^8 \frac{m}{s}$ ; see Fig. 4.13 for the time- and space-dependent  $H_{eff}$ ). Note that the photoinduced lattice rotation reverses its sign after approximately one picosecond. However, the oppositely oriented field has an amplitude an order of magnitude smaller than that at the surface, resulting in an effective total breaking of time-reversal symmetry. The sign change can be easily understood in terms of dephasing of the two non-degenerate phonons. In absence of dissipation, the total phononic field would keep switching between linear and circular polarizations with a period proportional to the inverse of their frequency difference.

**MAGNON DYNAMICS** In order to estimate the magnitude of the induced magnetic field, it is necessary to solve the equations governing the magnon dynamics. In a canted antiferromagnet the magnetic order evolution is described by the Landau–Lifshitz equations [45]:

$$\begin{aligned} \frac{d\vec{M}(t)}{dt} &= -\gamma \left\{ \left[ \vec{M}(t) \times H_{eff} \right] + \left[ \vec{L}(t) \times h_{eff} \right] \right\} \\ \frac{d\vec{L}(t)}{dt} &= -\gamma \left\{ \left[ \vec{M}(t) \times h_{eff} \right] + \left[ \vec{L}(t) \times H_{eff} \right] \right\} \end{aligned} \quad (4.19)$$

where  $\gamma = g \frac{\mu_B}{\hbar}$  is the gyromagnetic constant,  $\mu_B$  is the Bohr magneton and  $g \sim 2$  is the gyromagnetic ratio.  $H_{eff} = -\frac{\partial U_{spin-phonon}}{\partial M}$  and  $h_{eff} = -\frac{\partial U_{spin-phonon}}{\partial L}$  are

<sup>5</sup> Note that the proportionality constants between  $P$  and  $q$  do not play a role in estimating the size of the induced magnetic field. See next paragraph.

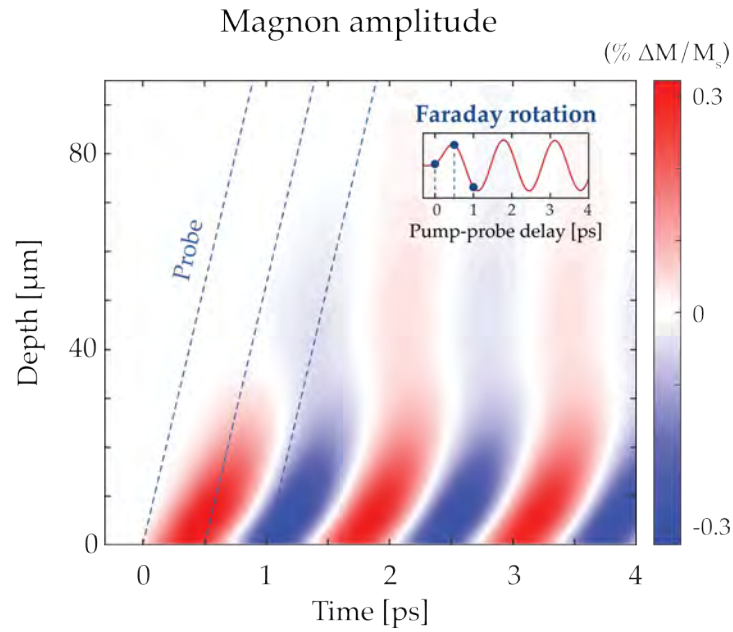


Figure 4.14: Magnetization dynamics. The Landau–Lifshitz equation was solved considering the calculated effective magnetic field as a driver. In order to compare the simulations to the experimental results, the phase-matched signal was retrieved by integrating the magnetization change along the lines of the propagating probe (oblique dotted blue line). This value was then normalized to the static magnetization magnitude. The simulated pump-probe signal is shown in the inset. The value of the phonon-driven effective magnetic field was estimated by matching the measured magnon amplitude with the simulated one.

the effective fields. In the case of the antiferromagnetic magnon and because of our excitation geometry, the only relevant field in our analysis is  $H_{eff}$ . For small deviations from the equilibrium Eq. 4.19 can be linearized and reduced to that of an harmonic oscillator [81]. The linearized equations were solved, considering the phonon-induced magnetic field as a driver, using a finite-difference method. The results of the calculations are shown in Figure 4.14. Note that because of the slow magnon velocity, any magnon propagation effect can be neglected<sup>6</sup>. To simulate the interaction of the probe light with the magnon, one needs to integrate the signal along the probe propagation lines (the slope is given by the group velocity). The simulated one-dimensional phase-matched signal measured by the probe is shown in the inset of Fig. 4.14. The effective field can be estimated from the calculated values by comparing the simulated magnetic dynamics with the measured one (Fig. 4.8A) without requiring the knowledge of any of the proportionality constants. The effective field was estimated to be 36 mT for a fluence of  $20 \frac{mJ}{cm^2}$ .

**MAGNON SELECTIVITY AND TEMPERATURE DEPENDENCE** The directionality of the effective field as perpendicular to the rotation plane of the atoms can be exploited to selectively couple to different spin waves [61]. While orthoferrites have two magnon branches, in the measurements at 100 K only the q-AFM could be excited (because of the orthogonality between  $H_{eff}$  and the antiferromagnetic vector  $L$ ). In order to drive the other resonance, that is the  $q$ -FM mode, it would be necessary to rotate the effective field to be orthogonal with respect to the ferromagnetic vector  $M$ . However, because of the SRT (Fig. 4.4), the spin axis spontaneously rotates by 90 degrees with respect to the crystallographic axes resulting in a progressive alignment of  $M$  with the  $a$  axis. By changing the temperature while leaving the mid-infrared excitation geometry unchanged the effective field goes from being orthogonal to  $L$  above the SRT to being orthogonal

<sup>6</sup> In other words, there is no phase matching between the phonon-polariton and the magnetic excitation.

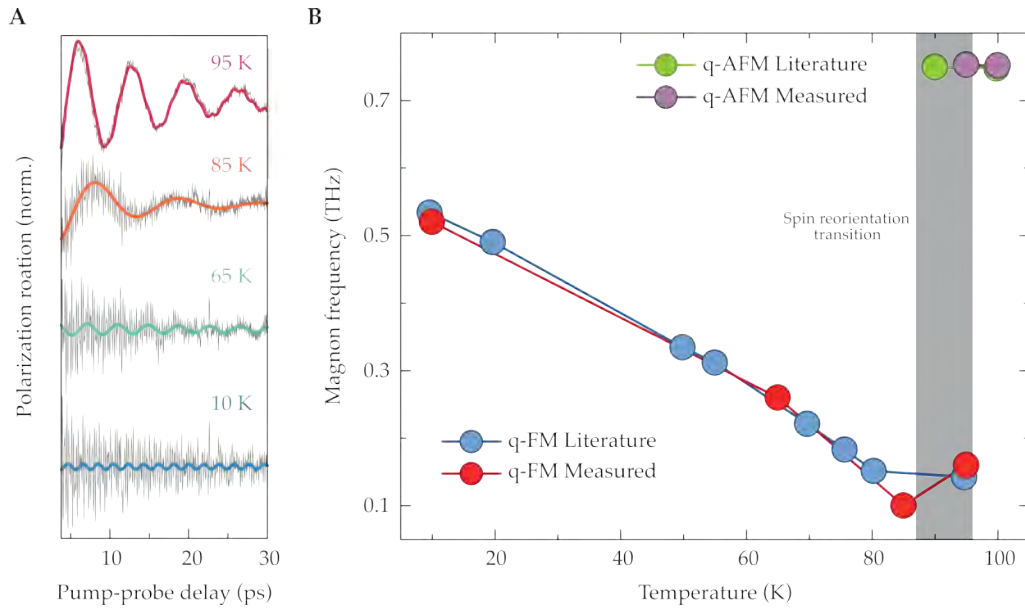


Figure 4.15: Temperature dependence of the magnetic oscillations. (A) Pump-induced polarization rotation at different sample temperatures. The signal comprising of both magnetic and vibrational excitations is shown in grey. The colored lines represent the magnon dynamics. The frequency of the oscillations changes dramatically with temperature. (B) Comparison of the detected frequency with literature data (from [131]). By changing the temperature of the system and, thus, the spin orientation, different magnon branches can be selectively excited.

to  $M$  below. These considerations were validated by temperature-dependent measurements.

The magnetic oscillations were found to strongly depend on the temperature as shown in Fig. 4.15A (these measurements were taken at 95, 65, 85 and 10 K). The excellent agreement between the measured magnon frequency with literature data confirmed that depending on the excitation geometry either resonances could be selectively excited (Fig. 4.15B).

### 4.3 CONCLUSIONS

The reported experiment proves that the framework of nonlinear phononics can be extended to include spin-phonon interactions and that infrared-active modes can couple to the magnetization of a material. This effect is found to create a

directional magnetic field pulse that can be used to selectively excite different spin waves. In more general terms, the observed phenomenon constitutes a rare example of *dynamical multiferroicity*, where magnetization control is achieved with electric fields. Furthermore, because the magnon strength scales nonlinearly with the phonon amplitude, much larger effects could be expected with a moderate increase in terahertz field. For example, phonon-driven nonlinear magnetic dynamics and possibly magnetic switching could be achieved. Lastly, as the magnetic field is created at terahertz frequencies, novel devices that work at such high speeds might be envisioned.



Part IV

CONCLUSIONS



---

## CONCLUSIONS

---

The functional properties of materials are intrinsically linked to their symmetry. When a symmetry is broken, new collective, ordered states can develop, such as ferroelectricity or superconductivity. The ability to control symmetries at will translates into the ability to manipulate the macroscopic phases of complex materials as well as their collective responses. Conventional techniques to achieve such degree of control are static. However, technological applications require collective properties to be modified dynamically, possibly at very high speeds. It was the goal of this thesis to explore new avenues to manipulate or even induce broken-symmetry phases in quantum materials with light.

The resonant excitation of infrared-active phonons with intense laser fields at terahertz frequencies stimulates highly nonlinear responses. In this regime, the coherent inelastic coupling among different degrees of freedom opens up new possibilities towards material control. For example, phonon-phonon interactions lead to large, transient and selective distortions of the crystal lattice which dramatically modify the electronic phases of strongly correlated materials [31, 88]. In this thesis, two different kinds of lattice nonlinearities were exploited: strain-phonon and spin-phonon coupling.

First, I studied the quantum paraelectric  $SrTiO_3$ . This material is particularly interesting because, despite its proximity to a ferroelectric instability, a long-range order never spontaneously develops. Here, quantum fluctuation of the

atomic positions prevent the transition to a broken-symmetry phase. However, I have shown experimentally that upon vibrational excitation with ultrashort pulses of light characteristics typical of ferroelectricity could be observed in the optical and electrical responses of the material. The photo-induced structural transition to a broken-symmetry state was highlighted by the appearance of a second-order optical nonlinearity, characterized by a polar point group. The hardening of a low-frequency vibration, reminiscent of a ferroelectric soft-phonon, suggests that the observed polarization is related to the stabilization of a long-range ferroelectric order. Unexpectedly, the photo-induced state was found to survive for hours after being created, suggesting that the material transitioned to a new metastable phase. This remarkable effect arises from strong nonlinearities of the crystal lattice. Due to strain-phonon coupling, the driven mode delivers some of its energy in the form of pressure to the material, leading to an inhomogeneous acoustic deformation of the photo-excited area. The resulting strain gradients activate a common material property called flexoelectricity which can locally break inversion symmetry and induce a polarization. Due to the nature of the coupling, pairs of ferroelectric domains are formed, as confirmed by spatially-resolved optical and electrical measurements.

This experiment proved that it is possible to induce a broken-symmetry phase with light even in materials that do not spontaneously develop one. While the mechanism which triggers the effect has been identified, it is still unclear what causes the observed accumulation and metastability of the photo-induced phase. Further experiments should be performed to isolate the origin of the phenomenon. For example, one could reduce the repetition rate of the pump to verify at what inter-pulse delay the accumulation ceases to occur. Systematic experiments should reveal the intrinsic timescales that govern such slow dynamics which could then be compared to different theoretical models. Another experiment could involve the AC measurement of the electrical properties of the photo-induced phase. If, for example, the accumulation and slow dynamics

was connected to a relaxor ferroelectric state a strong dispersion in the frequency of the AC field should be detected in both the dielectric constant and the dissipation.

The ability to induce flexoelectric polarizations in materials of any symmetry [142] with light should find extensive technological applications, especially in functional oxide interfaces. When different quantum materials, such as  $SrTiO_3$ , are combined to form oxide heterostructures, multiple collective phenomena can arise at the interface, such as superconductivity [102] or multiferroicity [71]. Under these conditions, because the electronic, structural, and magnetic degrees of freedom are closely tied together, the technique developed in this thesis could be used to manipulate the interfacial properties of strongly correlated oxides.

In the second part of the thesis, I have shown how lattice nonlinearities allow to control the order parameter of a preexisting broken-symmetry phase. In particular, I studied the canted ferromagnet  $ErFeO_3$  which displays multiple magnetic phase transitions and high-frequency magnons. The simultaneous excitation of orthogonal, non-degenerate, infrared-active vibrations resulted in the formation of circularly polarized phononic fields. This rotational atomic motion was found to break time-reversal symmetry and activate strong spin-phonon interactions. Under these conditions, the driven phonons mimicked the application of a directional magnetic field pulse and coupled directly to the magnetization of the material. As a result, large phonon-driven magnetic oscillations were observed. The experimental findings were also supported by the numerical solution of Maxwell and Landau-Lifshitz equations.

This experiment proved that optically-driven phononic fields can couple to and control the order parameter of a magnetic material at terahertz speed. Further experiments with larger excitation fields could promote interesting phonon-driven nonlinear effects, such as second harmonic magnon generation [2] or even magnetic switching [64, 111, 112].

Importantly, the present experiment was also the first one in which different phonons were simultaneously excited. Such approach largely expands the control capabilities by allowing the nonlinear coupling to modes of many different symmetries[100]. In this context, ultrafast structural switching [53] and phonon-induced piezomagnetic and piezoelectric effects [100] have been predicted. Lastly, the phonons excited here involved only the motion of the lighter *O* and *Fe* ions. However, many interesting properties arise from the heavier ions, such as *Er* in the studied orthoferrite. Novel magnetic, structural or electronic phenomena could be achieved by selectively driving lower-energy phonons [72] which exhibit larger Born effective charges and are connected to ions with stronger spin-orbit coupling.

Part V

APPENDIX



# A

---

## PARAMETRIC AMPLIFICATION OF OPTICAL PHONONS

---

Throughout this thesis we have shown how nonlinearities can be used to couple a driven infrared mode to other degrees of freedom leading to new possibilities for the optical control of materials. However, the nonlinear response of the driven phonon has been largely neglected. Here, we show how such nonlinearities allow for higher order nonlinear phononics effect such as the parametric amplification of the driven vibrational mode <sup>1</sup>.

**LINEAR POLARIZATION** The polarization induced by an electric field resonant with an infrared-active mode, already discussed in Chapter 2 and defined by the dielectric function Eq.2.15, can be rewritten to highlight the two most important contributions:

$$P_{tot} = P_{phonon} + P_{electrons} = Z^* Q_{IR} + \epsilon_0 (\epsilon_\infty - 1) E \quad (\text{A.1})$$

In Eq. A.1,  $P_{phonon}$  represents the polarization arising from the ionic displacement, where  $Z^*$  is the effective charge of the driven mode and  $Q_{IR}$  is the displacement from the equilibrium position. The second term  $P_{electrons}$  accounts for the polarization due to the electronic response to the driving electric field

---

<sup>1</sup> The experiment described in this chapter was published in [16].

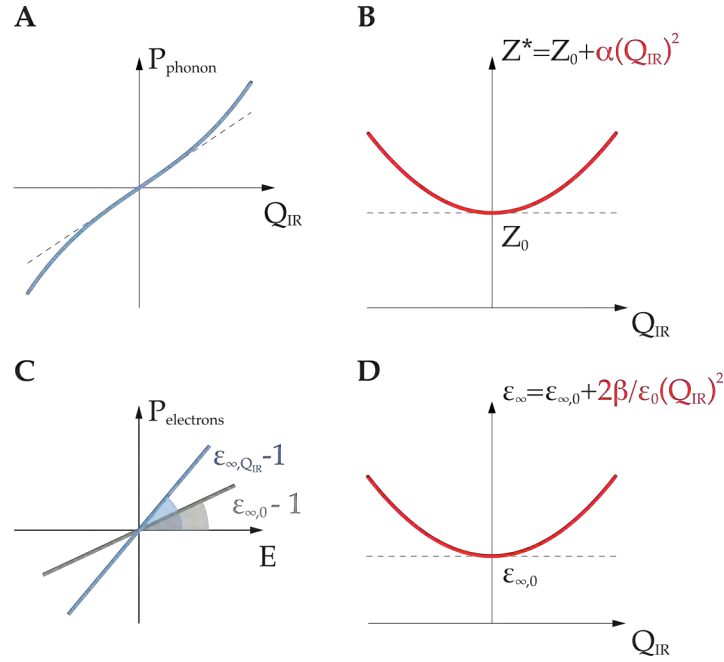


Figure A.1: Nonlinear expansion of the ionic and electronic contributions to the polarization in a solid, calculated from DFT. (A) Phonon polarization  $P_{\text{phonon}}$ . (B) Born effective charge. (C) Electronic polarization. The slope is given by the permittivity  $\epsilon_{\infty}$  which is shown in (D).

$E^2$ . It is possible to rewrite the potential of Eq.2.1 to explicitly include the above mentioned contributions:

$$U_{\text{linear}} = \frac{1}{2}\omega_{\text{TO}}^2 Q_{\text{IR}}^2 - Z^* E Q_{\text{IR}} - \frac{1}{2}\epsilon_0 (\epsilon_{\infty} - 1) E^2 \quad (\text{A.2})$$

The equation of motion defined by Eq.A.2 is the same that was introduced in Chapter 2 with Eq.2.5<sup>3</sup>:

$$\frac{\partial^2 Q_{\text{IR}}}{\partial t^2} + \Gamma \frac{\partial Q_{\text{IR}}}{\partial t} + \omega_{\text{TO}}^2 Q_{\text{IR}} = Z^* E \quad (\text{A.3})$$

**NONLINEAR POLARIZATION AND AMPLIFICATION** For strong driving fields, higher order nonlinear effects must be taken into account. In particular,

<sup>2</sup> As mentioned in Chapter 2,  $\epsilon_{\infty}$  represents the contribution of the higher-energy electronic resonances to the total dielectric response.

<sup>3</sup> Note that the lifetime term is introduced phenomenologically to account for dissipation.

both contributions to the total polarization must be modified. First, the lattice polarization  $P_{phonon}$  is no longer directly proportional to the lattice displacement  $Q_{IR}$  (Fig. A.1A). From first-principle calculations [10, 38, 39], for large electric fields we find that:

$$P_{phonon} = Z_0^* Q_{IR} + \alpha Q_{IR}^3 \quad (\text{A.4})$$

where  $\alpha$  is a material-specific coefficient. Eq.A.4 can be rewritten as:

$$P_{phonon} = Z^*(Q_{IR}) Q_{IR} = (Z_0^* + \alpha Q_{IR}^2) Q_{IR} \quad (\text{A.5})$$

to highlight that for strong driving fields the Born effective charge  $Z^*(Q_{IR}) = Z_0^* + \alpha Q_{IR}^2$  is no longer a constant but depends quadratically on displacement  $Q_{IR}$  (Fig.A.1B shows the DFT calculations for the semiconductor *SiC*).

Also the electronic polarization  $P_{electrons}$  must be modified to account for the nonlinear response of the material. For large excitation fields,  $P_{electrons}$  becomes:

$$P_{electrons} = \epsilon_0 (\epsilon_\infty(Q_{IR}) - 1) E = \epsilon_0 \left( \epsilon_{\infty,0} + \frac{2\beta}{\epsilon_0} Q_{IR}^2 - 1 \right) E \quad (\text{A.6})$$

This equation highlights that the electronic polarization is proportional to the impinging electric field only for small lattice displacements. In Fig.A.1C we show the calculated relationship between  $P_{electrons}$  and  $E$  both in the linear and nonlinear cases. For large ionic displacements, the slope increases. Similarly to the Born effective charge,  $\epsilon_\infty(Q_{IR}) = \epsilon_{\infty,0} + \frac{2\beta}{\epsilon_0} Q_{IR}^2$  is no longer a constant but depends nonlinearly on  $Q_{IR}$  (Fig.A.1D).

In the nonlinear regime, the energy potential becomes:

$$U_{nonlinear} = \frac{1}{2} \omega_{TO}^2 Q_{IR}^2 - (Z_0^* + \alpha Q_{IR}^2) E Q_{IR} - \frac{1}{2} \epsilon_0 \left( \epsilon_{\infty,0} + \frac{2\beta}{\epsilon_0} Q_{IR}^2 - 1 \right) E^2 \quad (\text{A.7})$$

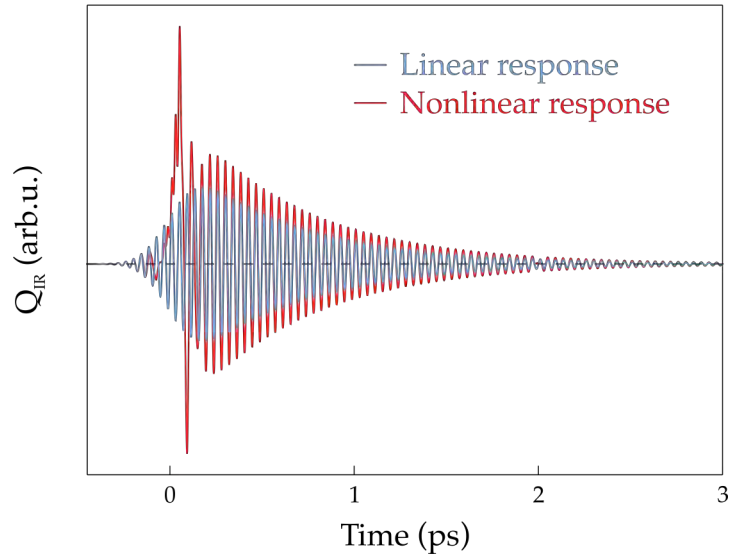


Figure A.2: Comparison between the response of a linear (blue) and a nonlinear (red) oscillator, driven by the same resonant electric field pulse.

which leads to the equation of motion:

$$\frac{\partial^2 Q_{IR}}{\partial t^2} + \Gamma \frac{\partial Q_{IR}}{\partial t} + (\omega_{TO}^2 - 2\beta E^2) Q_{IR} = (Z_0^* + \alpha Q_{IR}^2) E \quad (\text{A.8})$$

Fig. A.2 shows the linear and nonlinear phonon dynamics induced by the same driver defined by Eq. A.3 and Eq. A.8, respectively. Importantly, due to the lattice nonlinearities the phonon amplitude is amplified (purple line) with respect to the linear case (black line).

**EXPERIMENTAL PHONON AMPLIFICATION** In the previous paragraph we discussed how lattice nonlinearities can lead to phonon amplification. Here, we discuss of an experiment designed to verify these predictions.

Silicon carbide (SiC) is a semiconductor with a single infrared-active optical phonon. This mid-infrared vibration involves the in-plane motion of the carbon (blue) and silicon (red) ions (Fig. A.3A). The reflectivity associated with this mode (Fig. A.3B), displays the typical fingerprint of optical phonons in semiconductors: a high reflectivity spectral region in between the TO and LO

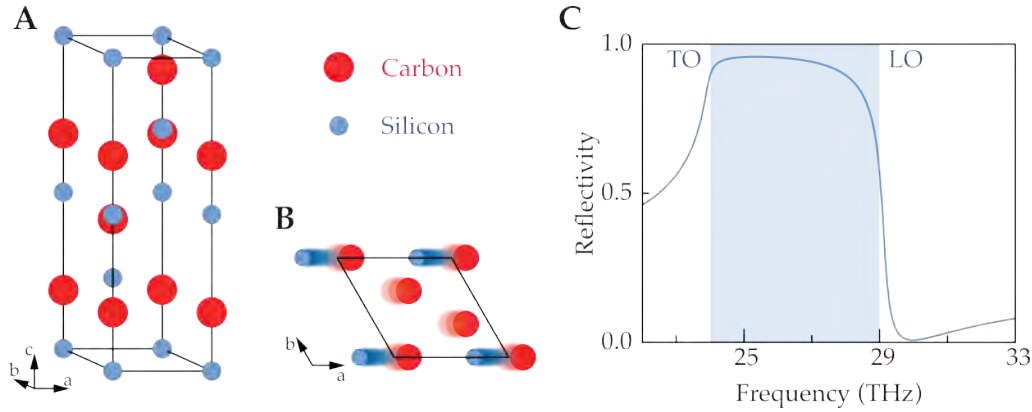


Figure A.3: (A) Crystal structure of 3C-SiC. (B) Investigated infrared active mode, with Silicon and Carbon atoms moving in opposite directions in the *ab*-plane. (C) Reflectivity associated with the studied mode.

frequencies ( $\omega_{TO} = 24 \text{ THz}$  and  $\omega_{LO} = 29 \text{ THz}$ ). The optical response can be modeled with a single Lorentz oscillator making it an ideal candidate for the investigation of the phononic nonlinear response.

The sample was excited with intense, CEP stable, 130 fs long pump pulses tuned at around 29 THz, i.e. in the proximity of the LO frequency. Fields of up to  $9 \frac{\text{MV}}{\text{cm}}$ , capable of driving the system into the nonlinear regime, could be achieved at the sample surface. The induced dynamics was probed with a 100 fs long mid-infrared pulse centered around 26 THz. The broad probe bandwidth, extending from 20 to 32 THz, covered the entire reststrahlen band of the phonon. In order to prevent any perturbative action on the sample, the probe electric field was one hundred times smaller than that of the pump. The probe pulses were employed to detect the pump-induced changes to the optical reflectivity in the proximity of the phonon resonance. Indeed, the pump and probe beams were modulated at different frequencies by a mechanical chopper allowing for the simultaneous detection of the unperturbed reflected field  $E_{off}(\tau)$  and the pump-induced changes  $\Delta E(t, \tau)$  [49] (Fig. A.5A). The electric field was measured directly using an electro-optic sampling technique where the amplitude and phase of an electric field is encoded in the polarization

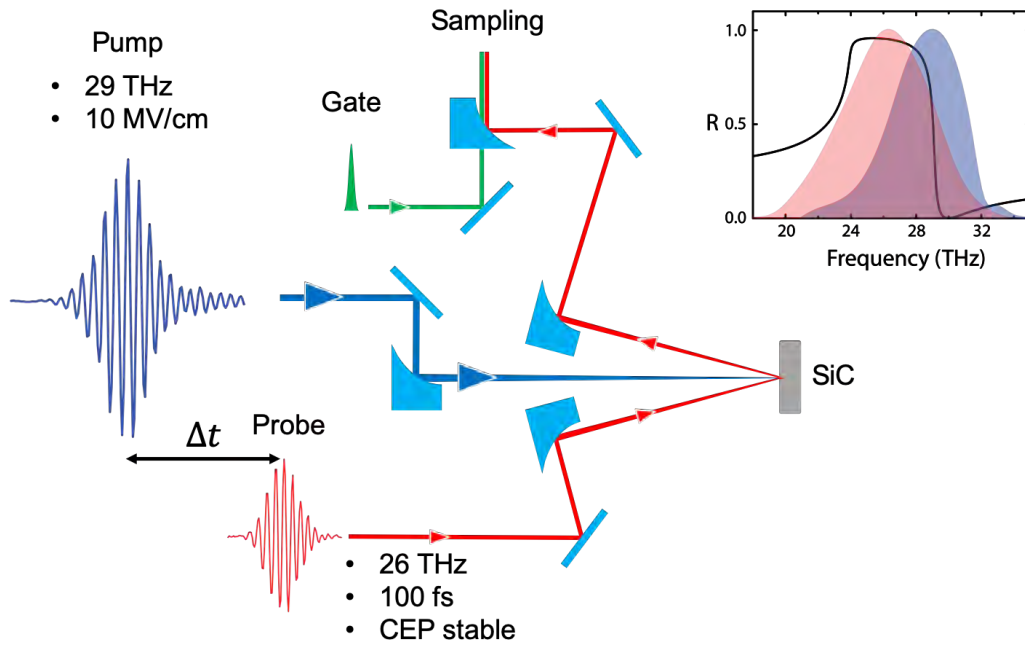


Figure A.4: Sketch of the experimental setup. The inset shows the spectral content of the pump (blue) and probe (red) pulses.

rotation of a sub-cycle sampling beam. Note that  $\tau$  is the sampling time while  $t$  is the pump-probe delay. A representative example of the measured field after reflection from the sample for a fixed pump-probe delay is shown in Fig. A.5A. The nonequilibrium reflectivity can then be directly calculated from the ratio  $\frac{\Delta E(\tau, t)}{E_{off}(\tau)}$ . For strong pump fields, a reflectivity higher than one was detected (Fig. A.5B). This observation signifies that the probe electric field has been amplified. In Fig. A.6A we show the time and frequency resolved reflectivity for different pump peak electric fields. The areas for which the reflectivity is greater than one are highlighted in red. Pump fields of at least  $4.9 \frac{MV}{cm}$  were needed to achieve amplification. For higher peak electric fields ( $5.9 \text{ MV/cm}$  and  $8.7 \text{ MV/cm}$ ), a reflectivity higher than one was observed in a broader frequency range and for longer times. The maximum measured reflectivity was  $R \sim 1.15$ . Note that only photons in the center of the reststrahlenband were amplified, independently on the pump field. Since the high reflectivity spectral region in the reststrahlen

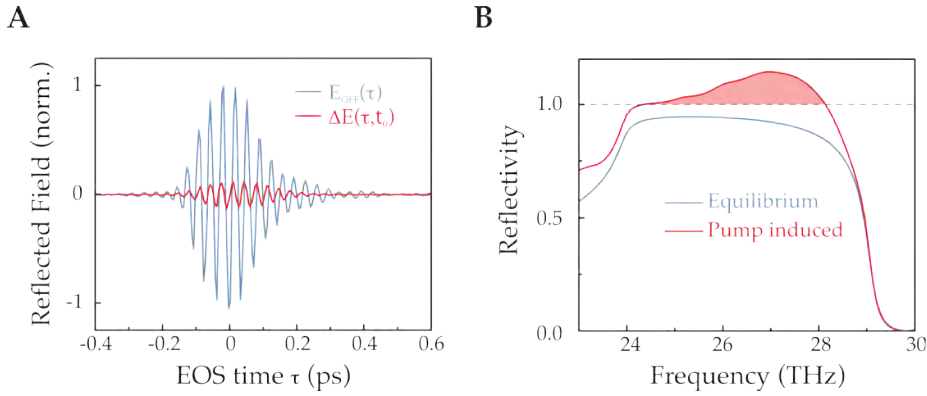


Figure A.5: (A) Electric field reflected from the sample at equilibrium (blue) and simultaneously measured pump-induced change (red). (B) Equilibrium (blue) and nonlinear (red) reflectivity of *SiC*.

band arises from the screening by the phonons of the impinging electric field, the amplification of probe photons is strongly suggestive of phonon amplification.

**SIMULATED PHONON AMPLIFICATION** In order to verify that the amplification of photons in the reststrahlen band corresponds to phonon amplification, we solved Maxwell's equations in the presence of lattice and electronic nonlinearities. The anharmonicities in  $Z^*(Q_{IR})$  and  $\epsilon_\infty(Q_{IR})$  were integrated in finite difference time domain (FDTD) calculations [47, 114, 135] which were used to simulate the experiment. This simple model, which in the case of a charged harmonic oscillator predicted phonon amplification, is also able to reproduce the experimental results in *SiC*. Figure A.6B shows the calculated time and frequency dependent reflectivity. The coefficients of the nonlinearities were adjusted to fit the experimental data. Like in the experiment, the reflectivity in the reststrahlen band exceeded unity for pump fields stronger than  $4 \frac{MV}{cm}$ . Higher field amplitudes also resulted in the amplification of more frequencies and for longer times. Because the model predictions are consistent with the experimental data, it is reasonable to assume that it captures the relevant physics of the phenomenon. In this case, we can compute the phonon dynamics that leads to the amplification of light to verify if it also gets amplified. Fig.A.7

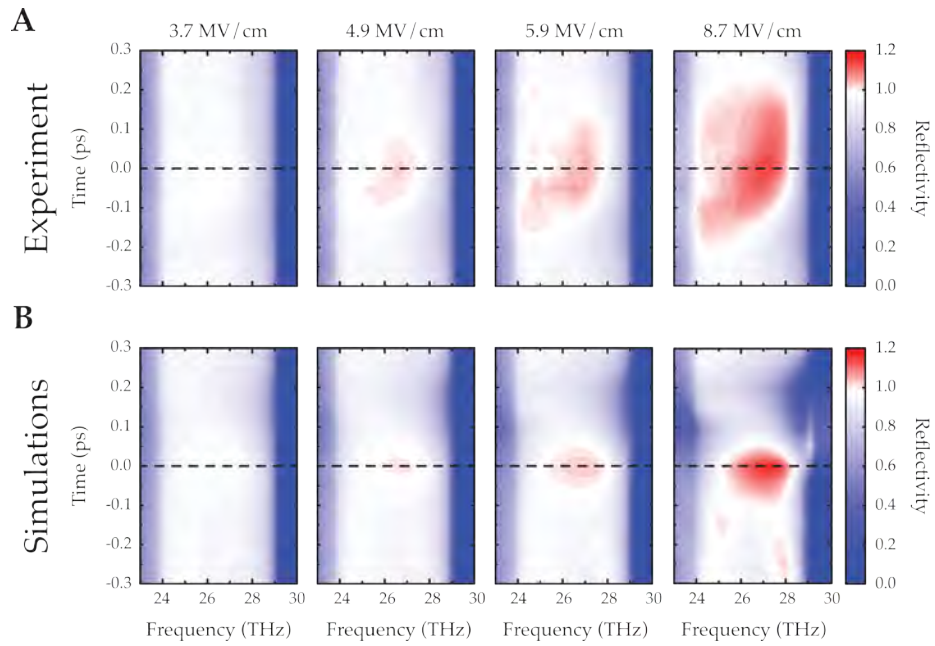


Figure A.6: Time and frequency dependent reflectivity for different intensities of the driving field. (A) Experimental results. (B) Simulations.

displays the electric field and corresponding phonon displacement initiated by the probe field just below the sample surface. Both quantities are significantly higher when the sample is excited by the pump (red lines) as compared to the equilibrium response (blue lines) confirming the simultaneous amplification of both photon and phonon fields .

**CONCLUSION** In this appendix, we have shown that lattice nonlinearities can severely modify the response of the driven phonon. In particular, we have proven that for large driving fields “constant” quantities such as the Born effective charge and  $\epsilon_\infty$  change with the intensity of the phononic field leading to the amplification of the phonon itself. This process can be regarded as parametric amplification or phononic four wave mixing where the parameters of the oscillator and the force acting on it change at twice the driving frequency.

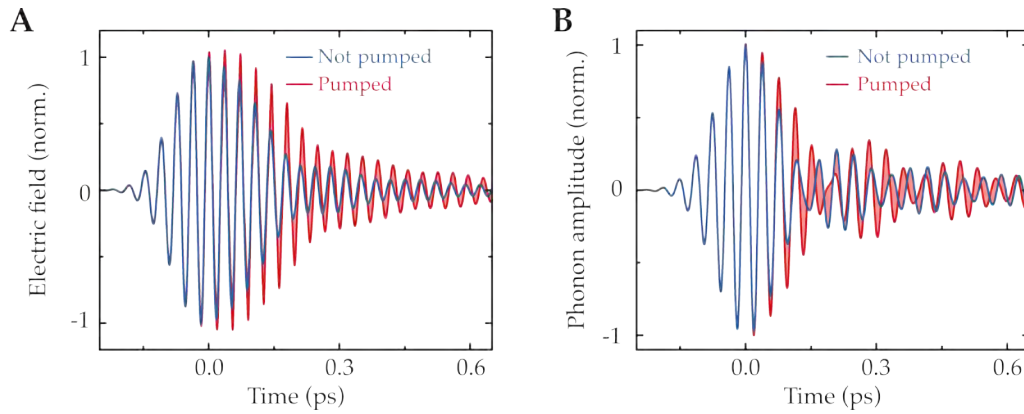


Figure A.7: Simulation results showing that a pump-induced increase of the electric field reflected from the sample (A) corresponds an amplification of the phonon oscillations amplitude (B).

This experiment proves that higher order nonlinear phononic effects can be significant and must be taken into account when exploiting lattice nonlinearities to control complex materials.



# B

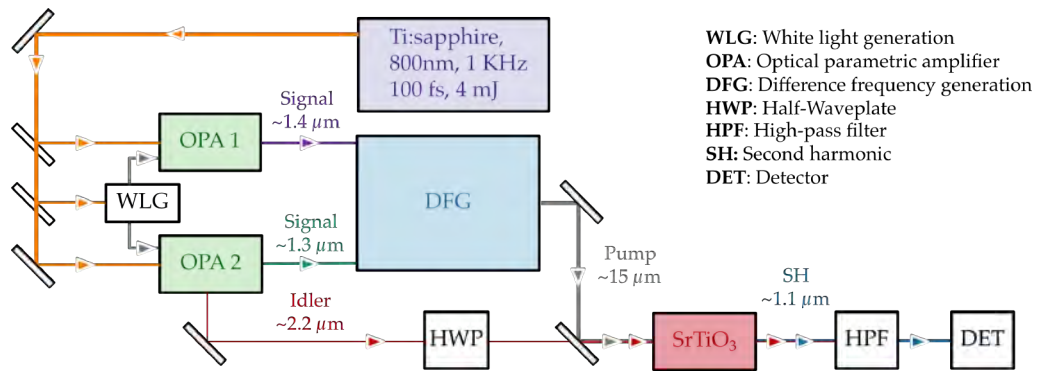
---

## EXPERIMENTAL SETUP

---

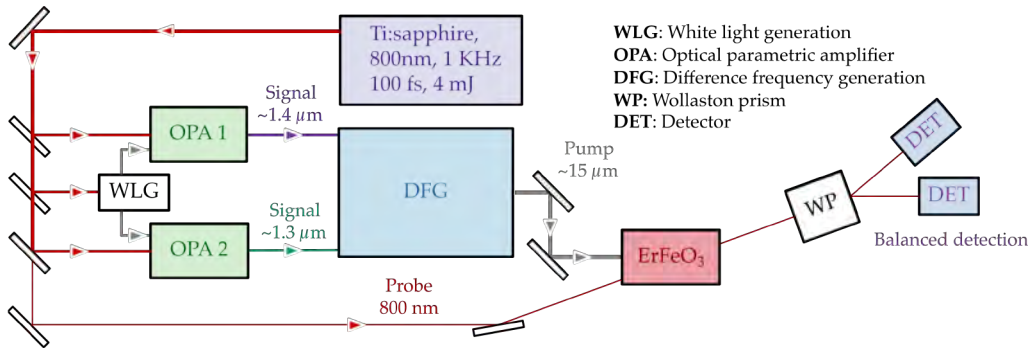
In this appendix, we describe the optical setups used for the experiments described in Chapter 3, 4 and in Appendix A.

All experiments had in common the same excitation light. The pump pulses were generated by converting the output of a 800 nm-wavelength commercial laser into mid-infrared radiation by means of multiple nonlinear optical processes. A Coherent Legend Ti:Sapphire regenerative amplifier capable of producing 100 femtosecond long, 800 nm-wavelength, 5.2 mJ pulses at 1 kHz repetition rate was used to seed two double-stages optical parametric amplifiers (OPA). A small fraction of the input power was used to generate a white light continuum (WLC) in a 2 mm thick sapphire window where self-phase modulation resulted in a dramatic broadening of the spectrum (hundreds of nanometers). The same WLC was then sent to the first amplification stages of both OPAs. Here, 120  $\mu\text{J}$ , 800 nm-wavelength pulses were combined with the WLC by dichroic mirrors. Non-collinear phase matching of these two beams in a 2 mm thick type-II BBO crystal resulted in the parametric amplification of selected frequencies within the WLC spectrum. Independently tunable, 60 femtosecond long, near infrared (from 1.2  $\mu\text{m}$  to 1.5  $\mu\text{m}$ ) pulses with energies ranging from 9 to 11  $\mu\text{J}$  were generated by each OPA. These pulses were further amplified by means of a second amplification stage in 3 mm thick type-II BBO crystals. 1.8 mJ, 800 nm-wavelength pump pulses were combined with the

Figure B.1:  $SrTiO_3$  setup.

output of the first stages to generate  $300 \mu J$ , 80 femtosecond long, near infrared pulses. The mid-infrared pump pulses were obtained by difference frequency generation (DFG) between the two near-infrared OPA outputs in a  $600 \mu m$  thick, z-cut GaSe nonlinear crystal. The frequency of the mid-infrared pulses could be tuned by changing the wavelength of the near-infrared beams. 100 femtosecond long, 5 to  $15 \mu J$  pump pulses could be consistently achieved in the 18 to 50 THz frequency range. In all experiments the pump pulse frequency was determined by either Fourier Transform Interferometry or electro-optic sampling.

**OPTICALLY-INDUCED FERROELECTRICITY** The pump beam was focused using an off-axis parabolic mirror down to a  $72 \mu m$  spot size. Fluences in excess of  $50 \frac{mJ}{cm^2}$  could be achieved for all pump wavelengths. As a probe, a fraction of the idler of one of the pump OPAs, tuned at  $2.2 \mu m$  was used as the fundamental beam in second-harmonic generation measurements. The idler polarization was controlled with a half-waveplate. A short-pass filter with a 1500 nm cut-off wavelength was used after the sample to block the fundamental ( $2.2 \mu m$ ) and isolate the second harmonic photons ( $1.1 \mu m$ ). Specific polarizations of the second harmonic electric field could be isolated by a polarizer positioned after the sample. The second harmonic intensity was measured with a low-noise InGaAs detector sensitive to 800-1700 nm photons. The detector was coupled to a lock-in amplifier. The probe beam profile in the focus was  $52 \mu m$ , smaller

Figure B.2:  $\text{ErFeO}_3$  setup

than the pump spot. Pump and probe were collinear and normal to the sample surface. The sketch of the optical setup is shown in Fig. B.1.

For the second harmonic shadow imaging experiment, the detector was replaced by a CMOS camera while the probe was collimated and no longer focused. The probe spot ( $1200 \mu\text{m}$ ) was much bigger than that of the focused pump ( $72 \mu\text{m}$ ). In all experiments, a cold finger cryostat was used to control the sample temperature.

**PHONON-INDUCED MAGNETIC FIELDS** A small part of the Ti:Sapphire 800 nm beam was used to probe the pump-induced dynamics. The polarization rotation of the transmitted linearly polarized probe was measured with a balanced detection scheme. A half-waveplate and a polarizer were used to align the probe polarization to one of the sample crystallographic axes to reduce the detrimental effects of birefringence to magnetic dynamics measurements. After the sample, a Wollaston prism was used to split the probe field in two orthogonal polarization components. A half-waveplate placed before the prism was used to balance the intensity on two identical diodes. The difference between the signals on the two detectors was measured by a lock-in amplifier. A nonzero difference signified that the polarization of the probe beam changed. A schematic representation of the setup is shown in Figure B.2.

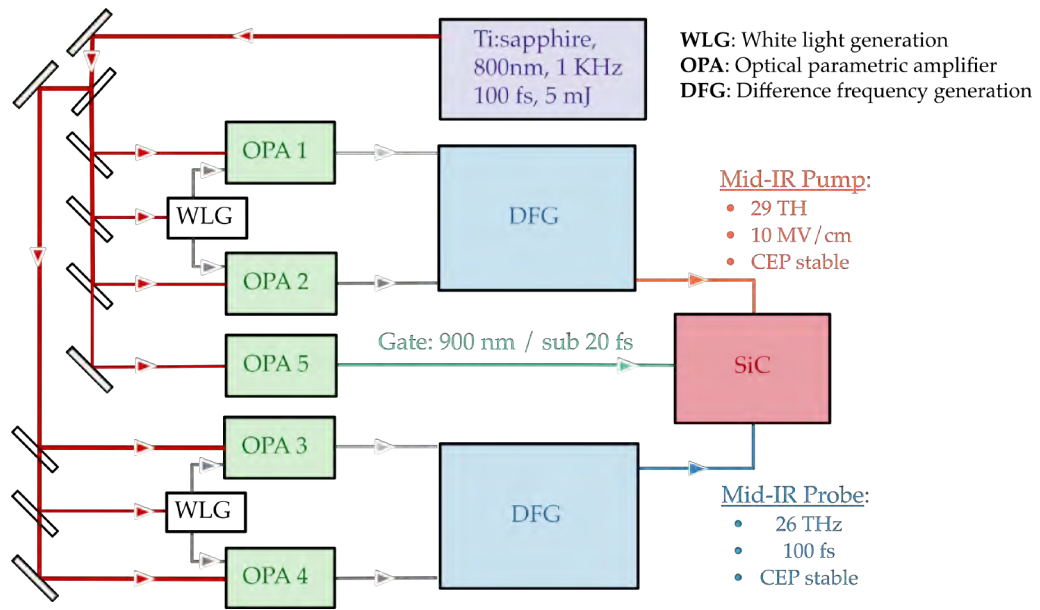


Figure B.3: SiC setup.

**PHONON AMPLIFICATION** The pump pulses were focused with an off-axis parabolic mirror down to a beam diameter of around  $240 \mu\text{m}$ . Peak fields of  $10 \frac{\text{MV}}{\text{cm}}$  could be achieved.

Unlike the other experiments, the probe pulses were also in the mid-infrared frequency range. A copy of the pump generation setup, comprising of two double-stages OPAs and DFG, was seeded by 15% of the Ti:Sapphire power. The system produced 100 femtosecond long pulses tuned to 26.5 THz. The probe was focused on the sample down to a beam diameter of around  $170 \mu\text{m}$  at a 15 degrees angle from normal incidence. The electric field of the reflected probe pulses was measured via electro-optic sampling (EOS) in a different GaSe crystal. The sub-cycle gate pulses were generated with a non-collinear optical parametric amplifier (NOPA) seeded with the second harmonic (400 nm) of 5% of the Ti:Sapphire power. Near-infrared pulses with a 60nm bandwidth centered at around 900 nm were compressed with chirped mirrors down to 20 femtoseconds. The pulse duration was measured with the frequency resolved optical gating (FROG) technique. A double modulation of pump and

probe beams at different frequencies via the same mechanical chopper was implemented to measure simultaneously the equilibrium ( $E_{off}(\tau)$ ) and pump-induced ( $\Delta E(\tau, t)$ ) reflected electric fields as a function of EOS time  $\tau$  and pump-probe delay  $t$ . Importantly, from these measurements, calibrated electric field amplitudes and phases could be retrieved. The measured changes in complex reflectance was then added to the equilibrium one allowing to calculate the optical reflectivity of the sample as a function of both frequency and pump-probe delay. This experiment was carried out at room temperature. Figure B.3 shows a sketch of the measurement setup.



---

## ACKNOWLEDGMENTS

---

The first week of my PhD, Andrea Cavalleri invited me to join him for a meeting. In Paris. In a wonderful 17th century building in the center of the city. There, despite being a beginner in his first week of work, I had the chance to have a friendly chat with some of the most accomplished scientists in the field. This memory, which has little to do with science, sets the scene for the kind of opportunities that I was given access to because of Andrea. I had the chance to work with state-of-the-art equipment in brand-new laboratories. I could present my research in many different venues. I had the opportunity to travel all around the world and to build a professional network. Thank you for exposing me to every aspect of the profession while continuously advising me. Thank you for constantly pushing me to grow and to develop my own ideas.

I owe a great deal of gratitude to Michael Först. Thank you for always finding the time to listen to me and for the continued support. And thank you for offering your help independently on the nature of the problem.

Thank you Martin for always being ready to discuss interesting problems and explain what I did not understand.

Thank you Michele, for all the discussions and the words of advice. Thank you for your positivity and for always being there when I needed it.

Thank you Thomas for always being ready to help. Thank you for sharing your knowledge on lasers, stock options and bitcoins. I hope I will be in the position to fulfill our deal.

Thank you Matthias, for being the kindest human being that ever was. Thank you for your optimism, thank you for listening and thank you for caring. Most importantly, thank you for initiating the masterpiece that is our office wall.

Thank you Adrian for letting me teach you what a good wine is and how to cook a steak. And thank you for gifting me the best wine glasses I ever had.

Thank you Michael Fechner for constantly offering your help. Thank you (and Sabine) for the nice barbecues at your place.

Happy birthday Gregor.

Thank you Toru for always being ready to answer all my trivial questions about electronics.

Thank you Guido for learning Italian, it made me feel at home.

Thank you Boris for always finding a solution to every electronics-related problem I ever had.

Thank you Alex for making me feel old and unsuccessful.

Thank you Daniele and Yannis for the nice evenings, especially during my first year in Hamburg.

Thank you Matteo and James for the career advice.

Thank you Srivats and Ivanka for all the nice dinners and boat excursions. Congratulations for becoming parents!

Thank you Sven for the many good memories throughout the years.

Thank you Mariana for being so kind to me.

Thank you Razvan for the wonderful drawings. The butterfly is still my favorite.

Thank you Alice and Regina for always being willing to help.

Thank you Joerg for creating such beautiful images.

Thank you to the purchasing team, Ulrike and Tania, for fulfilling way too many "urgent" order. You made my job much easier.

Thank you Francesca Calegari for being around at both my graduations, the one in Milano and the one in Hamburg. I am always happy to see you.

Thank you Andrea Trabattoni for being the living proof that it is possible to be close friends even with people of different believes. I am referring to football. Forza Inter.

Thank you Serena for still talking to me despite our first (completely fictional) meeting.

Thank you Ankit for all the help during these last, complicated years. Thank you especially for your enlightening business and political views, they always sparked entertaining discussions. Also, to be completely fair, your cat is the prettiest of all.

Thank you Jasone for the many times you made me laugh. Also, now because of you I can understand and process 500 words per second, thank you.

Thank you Hauke for being such a good friend. I will not forget the wonderful dishes you cooked for me when I could not move away from my sofa.

The most special thank you goes to the Italian crew of “cena domenica”. Thank you Francesca for the endless energy and for always trying to lift everybody’s spirits. And thank you for forcing me to be a little less boring than I usually am. Thank you Maria for being so kind and generous. Thank you for always writing first. But most importantly, thank you for the many wonderful plants that keep surviving despite my best efforts.

Thank you Andrea for supporting the only reasonable football team, for living in the right apartment and for working in the correct lab. Thank you for teaching me how to work in an experimental lab and for making me understand “che l’ottimo è nemico del buono”. Or at least you tried. I learned a lot from you. Thank you for the countless hospital visits. Thank you for always being there for me. Thank you for listening to me, over and over again. You helped me tremendously in countless ways; thank you for being my rock. Everything you did meant a lot to me and I will not forget it. Thank you for being my best friend.

Eliza, “*if you must blink, do it now*”. Thank you for transforming the simplest things in wonderful adventures. Thank you for the joy that your smile sparks in me and everybody around you. Thank you for the countless memories. We should find a way to bring THAT margarita to Paris. Thank you for your passion,

for your love and for being the funniest person I know (after Sabina). Thank you Sabala for the endless enthusiasm, the unexpected laughter, the hugs and the unforgettable dances. You are way too young to have so much to teach.

A heartfelt thank you to my family for gifting me the opportunity to follow my dreams. I know what was the cost.

Papà, vorrei poterti raccontare a che punto sono arrivato del cammino che mi hai mostrato.

---

## ROLE OF THE AUTHOR

---

This dissertation contains the work performed by the author during his PhD at the Max Planck Institute for the Structure and Dynamics of Matter, within the Quantum Condensed Matter Dynamics division and at the University of Hamburg. The two main projects at the core of this thesis were conceived by Andrea Cavalleri together with the author. The OPAs used for the generation of the pump pulses was built by the author together with Andrea Cartella.

- Chapter 3: The optical experiments were designed, implemented and performed by the author with help from Ankit Disa. The electrical measurements were designed by Ankit Disa with help from the author. The electrical measurements were performed by the the author together with Ankit Disa. The interpretation was developed by the author together with Andrea Cavalleri, Ankit Disa and Michael Fechner. The DFT calculations were performed by Michael Fechner. The data analysis was performed by the author together with Ankit Disa.
- Chapter 4: The experiments were designed, implemented and performed by the author together with Andrea Cartella. The data analysis was performed by the author. The code for the numerical solution of Maxwell's equations was developed by Andrea Cartella with help from the author. The code for the numerical solution of the Landau-Lifshitz equations was developed by the author. The data was interpreted by the author together with Andrea Cavalleri and under the guidance of Roberto Merlin. A. Kimel, R. Mikhaylovskiy and D. Bossini selected the physical system and provided the sample.

- Appendix A: The experiment was conceived by Andrea Cavalleri. The code for the simulations was developed by Andrea Cartella. The experiments were designed and implemented by Andrea Cartella with help from the author. The experiments were performed by Andrea Cartella together with the author. The data analysis was performed by Andrea Cartella. The simulations were performed by Andrea Cartella. The DFT calculations were performed by Michael Fechner. The theoretical model was developed by Michael Fechner and Andrea Cartella with input from the author.

The FTIR used to measure the frequency of the pump pulses was built by Andrea Cartella. The NOPA used to measure the electro-optic sampling of the mid-infrared pulses was built by Alice Cantaluppi and Andrea Cartella.

---

## BIBLIOGRAPHY

---

- [1] C. H. Ahn, K. M. Rabe, and J.-M. Triscone. “Ferroelectricity at the Nanoscale: Local Polarization in Oxide Thin Films and Heterostructures.” In: *Science* 303.5657 (2004), pp. 488–491 (cit. on p. 72).
- [2] S. Baierl et al. “Terahertz-Driven Nonlinear Spin Response of Antiferromagnetic Nickel Oxide.” In: *Physical Review Letters* 117.19 (2016), p. 197201 (cit. on p. 107).
- [3] M. Bartkowiak, G. J. Kearley, M. Yethiraj, and A. M. Mulders. “Symmetry of ferroelectric phase of SrTi<sub>18</sub>O<sub>3</sub> determined by ab initio calculations.” In: *Physical Review B* 83.6 (2011), p. 064102 (cit. on p. 45).
- [4] D. N. Basov, R. D. Averitt, and D. Hsieh. “Towards properties on demand in quantum materials.” In: *Nature Materials* 16.11 (2017), pp. 1077–1088 (cit. on p. 7).
- [5] D. N. Basov, Richard D. Averitt, Dirk van der Marel, Martin Dressel, and Kristjan Haule. “Electrodynamics of correlated electron materials.” In: *Reviews of Modern Physics* 83.2 (2011), pp. 471–541 (cit. on p. 8).
- [6] Ya. B. Bazaliy, L. T. Tsymbal, G. N. Kakazei, A. I. Izotov, and P. E. Wigen. “Spin-reorientation in ErFeO<sub>3</sub> Zero-field transitions, three-dimensional phase diagram, and anisotropy of erbium magnetism.” In: *Physical Review B* 69.10 (2004), p. 104429 (cit. on p. 79).
- [7] R. S. Beach, J. A. Borchers, A. Matheny, R. W. Erwin, M. B. Salamon, B. Everitt, K. Pettit, J. J. Rhyne, and C. P. Flynn. “Enhanced Curie temperatures and magnetoelastic domains in Dy/Lu superlattices and films.” In: *Physical Review Letters* 70.22 (1993), pp. 3502–3505 (cit. on p. 39).

- [8] J. G. Bednorz and K. A. Müller. “Sr<sub>1-x</sub>Ca<sub>x</sub>TiO<sub>3</sub>: An XY Quantum Ferroelectric with Transition to Randomness.” In: *Physical Review Letters* 52.25 (1984), pp. 2289–2292 (cit. on pp. 37, 38).
- [9] U. Bianchi, W. Kleemann, and J. G. Bednorz. “Raman scattering of ferroelectric Sr<sub>1-x</sub>Ca<sub>x</sub>TiO<sub>3</sub>, x=0.007.” In: *Journal of Physics: Condensed Matter* 6.6 (1994), pp. 1229–1238 (cit. on p. 55).
- [10] P. E. Blöchl. “Projector augmented-wave method.” In: *Physical Review B* 50.24 (1994), pp. 17953–17979 (cit. on p. 113).
- [11] Robert W. Boyd. *Nonlinear Optics*. Elsevier, 2003 (cit. on p. 42).
- [12] R. M. Bozorth, H. J. Williams, and Dorothy E. Walsh. “Magnetic Properties of Some Orthoferrites and Cyanides at Low Temperatures.” In: *Physical Review* 103.3 (1956), pp. 572–578 (cit. on p. 79).
- [13] I. Bozovic, G. Logvenov, I. Belca, B. Narimbetov, and I. Sveklo. “Epitaxial Strain and Superconductivity in La<sub>2-x</sub>S<sub>x</sub>CuO<sub>4</sub> Thin Films.” In: *Physical Review Letters* 89.10 (2002), p. 107001 (cit. on p. 39).
- [14] A. Cantaluppi et al. “Pressure tuning of light-induced superconductivity in K<sub>3</sub>C<sub>60</sub>.” In: *Nature Physics* 14.8 (2018), pp. 837–841 (cit. on p. 8).
- [15] A. Cartella, T. F. Nova, M. Fechner, R. Merlin, and A. Cavalleri. “Parametric amplification of optical phonons.” In: *Proceedings of the National Academy of Sciences* 115.48 (2018), pp. 12148–12151 (cit. on pp. 8, 22).
- [16] A. Cartella, T. F. Nova, M. Fechner, R. Merlin, and A. Cavalleri. “Parametric amplification of optical phonons.” In: *Proceedings of the National Academy of Sciences* 115.48 (2018), pp. 12148–12151 (cit. on p. 111).
- [17] Andrea Cartella. “Amplification of optically driven phonons.” In: (2018) (cit. on p. 94).
- [18] S. Catalano, M. Gibert, J. Fowlie, J. Íñiguez, J.-M. Triscone, and J. Kreisel. “Rare-earth nickelates RNiO<sub>3</sub>: thin films and heterostructures.” In: *Reports on Progress in Physics* 81.4 (2018), p. 046501 (cit. on p. 9).

- [19] A. D. Caviglia et al. "Ultrafast Strain Engineering in Complex Oxide Heterostructures." In: *Physical Review Letters* 108.13 (2012), p. 136801. (Visited on 10/11/2019) (cit. on p. 8).
- [20] Y.-D. Chuang, A. D. Gromko, D. S. Dessau, T. Kimura, and Y. Tokura. "Fermi Surface Nesting and Nanoscale Fluctuating Charge/Orbital Ordering in Colossal Magnetoresistive Oxides." In: 292.5521 (2001), pp. 1509–1513 (cit. on p. 6).
- [21] Robert L. Cummrow. "Photovoltaic Effect in  $p$ - $n$  Junctions." In: *Physical Review* 95.1 (1954), pp. 16–21 (cit. on p. 58).
- [22] Elbio Dagotto. "Complexity in Strongly Correlated Electronic Systems." In: *Science* 309.5732 (2005), pp. 257–262 (cit. on p. 9).
- [23] P. Dore, G. De Marzi, and A. Paolone. "Refractive indices of SrTiO<sub>3</sub> in the infrared region." In: *International Journal of Infrared and Millimeter Waves* 18.1 (1997), pp. 125–138 (cit. on p. 35).
- [24] V. Esposito et al. "Nonlinear Electron-Phonon Coupling in Doped Manganites." In: *Physical Review Letters* 118.24 (2017), p. 247601 (cit. on p. 29).
- [25] M. FARADAY. "On the Magnetization of Light and the Illumination of Magnetic Lines of Force." In: *Philosophical Transactions of the Royal Society of London* 136 (1846), pp. 1–20 (cit. on p. 83).
- [26] D. Fausti et al. "Light-Induced Superconductivity in a Stripe-Ordered Cuprate." In: *Science* 331.6014 (2011), pp. 189–191 (cit. on p. 8).
- [27] M. Fechner and N. A. Spaldin. "Effects of intense optical phonon pumping on the structure and electronic properties of yttrium barium copper oxide." In: *Physical Review B* 94.13 (2016), p. 134307 (cit. on p. 60).
- [28] Manfred Fiebig, Victor V. Pavlov, and Roman V. Pisarev. "Second-harmonic generation as a tool for studying electronic and magnetic structures of crystals: review." In: *JOSA B* 22.1 (2005), pp. 96–118 (cit. on p. 40).

- [29] Jan Fink-Finowicki. "The influence of crystal symmetry on magneto-optical effects in orthoferrites." In: *Physica B+C* 115 (1983), pp. 225–228 (cit. on p. 85).
- [30] P. A. Fleury and R. Loudon. "Scattering of Light by One- and Two-Magnon Excitations." In: *Physical Review* 166.2 (1968), pp. 514–530 (cit. on p. 93).
- [31] M. Först, R. Mankowsky, and A. Cavalleri. "Mode-Selective Control of the Crystal Lattice." In: *Accounts of Chemical Research* 48.2 (2015), pp. 380–387 (cit. on pp. 11, 105).
- [32] M. Först, C. Manzoni, S. Kaiser, Y. Tomioka, Y. Tokura, R. Merlin, and A. Cavalleri. "Nonlinear phononics as an ultrafast route to lattice control." In: *Nature Physics* 7.11 (2011), pp. 854–856. (Visited on 10/11/2019) (cit. on pp. 8, 22).
- [33] M. Först et al. "Displacive lattice excitation through nonlinear phononics viewed by femtosecond X-ray diffraction." In: *Solid State Communications* 169 (2013), pp. 24–27 (cit. on p. 9).
- [34] M. Först et al. "Displacive lattice excitation through nonlinear phononics viewed by femtosecond X-ray diffraction." In: *Solid State Communications* 169 (Sept. 2013), pp. 24–27 (cit. on p. 27).
- [35] V. M. Fridkin. "Bulk photovoltaic effect in noncentrosymmetric crystals." In: *Crystallography Reports* 46.4 (2001), pp. 654–658 (cit. on p. 58).
- [36] Q. Gan, R. A. Rao, C. B. Eom, J. L. Garrett, and Mark Lee. "Direct measurement of strain effects on magnetic and electrical properties of epitaxial SrRuO<sub>3</sub> thin films." In: *Applied Physics Letters* 72.8 (1998), pp. 978–980 (cit. on p. 39).
- [37] T. Gebert, D. Rompotis, M. Wieland, F. Karimi, A. Azima, and M. Drescher. "Michelson-type all-reflective interferometric autocorrelation in the VUV regime." In: *New Journal of Physics* 16.7 (2014), p. 073047 (cit. on p. 67).

- [38] Paolo Giannozzi et al. “QUANTUM ESPRESSO: a modular and open-source software project for quantum simulations of materials.” In: *Journal of Physics: Condensed Matter* 21.39 (2009), p. 395502 (cit. on p. 113).
- [39] Xavier Gonze and Changyol Lee. “Dynamical matrices, Born effective charges, dielectric permittivity tensors, and interatomic force constants from density-functional perturbation theory.” In: *Physical Review B* 55.16 (1997), pp. 10355–10368 (cit. on p. 113).
- [40] J. H. Haeni et al. “Room-temperature ferroelectricity in strained SrTiO<sub>3</sub>.” In: *Nature* 430.7001 (2004), pp. 758–761 (cit. on p. 39).
- [41] J. Hemberger, P. Lunkenheimer, R. Viana, R. Böhmer, and A. Loidl. “Electric-field-dependent dielectric constant and nonlinear susceptibility in SrTiO<sub>3</sub>.” In: *Physical Review B* 52.18 (1995), pp. 13159–13162 (cit. on p. 37).
- [42] J. Hemberger, M. Nicklas, R. Viana, P. Lunkenheimer, A. Loidl, and R. Böhmer. “Quantum paraelectric and induced ferroelectric states in.” In: *Journal of Physics: Condensed Matter* 8.25 (1996), pp. 4673–4690 (cit. on p. 37).
- [43] A. von Hoegen, R. Mankowsky, M. Fechner, M. Först, and A. Cavalleri. “Probing the interatomic potential of solids with strong-field nonlinear phononics.” In: *Nature* 555.7694 (2018), pp. 79–82 (cit. on pp. 8, 22).
- [44] W. Hu et al. “Optically enhanced coherent transport in YBa<sub>2</sub>Cu<sub>3</sub>O<sub>6.5</sub> by ultrafast redistribution of interlayer coupling.” In: *Nature Materials* 13.7 (2014), pp. 705–711 (cit. on p. 8).
- [45] Ryugo Iida, Takuya Satoh, Tsutomu Shimura, Kazuo Kuroda, B. A. Ivanov, Yusuke Tokunaga, and Yoshinori Tokura. “Spectral dependence of photoinduced spin precession in DyFeO<sub>3</sub>.” In: *Physical Review B* 84.6 (2011), p. 064402 (cit. on p. 97).

- [46] Masatoshi Imada, Atsushi Fujimori, and Yoshinori Tokura. “Metal-insulator transitions.” In: *Reviews of Modern Physics* 70 (1998), pp. 1039–1263. (Visited on 10/12/2019) (cit. on p. 6).
- [47] Umran S. Inan and Robert A. Marshall. *Numerical Electromagnetics: The FDTD Method*. Cambridge University Press, 2011 (cit. on p. 117).
- [48] M. Itoh, R. Wang, Y. Inaguma, T. Yamaguchi, Y-J. Shan, and T. Nakamura. “Ferroelectricity Induced by Oxygen Isotope Exchange in Strontium Titanate Perovskite.” In: *Physical Review Letters* 82.17 (1999), pp. 3540–3543 (cit. on p. 37).
- [49] Krzysztof Iwaszczuk, David G. Cooke, Masazumi Fujiwara, Hideki Hashimoto, and Peter Uhd Jepsen. “Simultaneous reference and differential waveform acquisition in time-resolved terahertz spectroscopy.” In: *Optics Express* 17.24 (2009), pp. 21969–21976 (cit. on p. 115).
- [50] H. W. Jang et al. “Ferroelectricity in Strain-Free SrTiO<sub>3</sub> Thin Films.” In: *Physical Review Letters* 104.19 (2010), p. 197601 (cit. on p. 71).
- [51] J. A. de Jong, A. V. Kimel, R. V. Pisarev, A. Kirilyuk, and Th. Rasing. “Laser-induced ultrafast spin dynamics in ErFeO<sub>3</sub>.” In: *Physical Review B* 84 (2011), p. 104421 (cit. on p. 79).
- [52] Maarten de Jong, Wei Chen, Henry Geerlings, Mark Asta, and Kristin Aslaug Persson. “A database to enable discovery and design of piezoelectric materials.” In: *Scientific Data* 2.1 (2015), pp. 1–13 (cit. on p. 60).
- [53] D. M. Juraschek, M. Fechner, and N. A. Spaldin. “Ultrafast Structure Switching through Nonlinear Phononics.” In: *Physical Review Letters* 118.5 (2017), p. 054101 (cit. on pp. 76, 108).
- [54] S. Kaiser et al. “Optically induced coherent transport far above T<sub>c</sub> in underdoped YBa<sub>2</sub>Cu<sub>3</sub>O<sub>6+δ</sub>.” In: *Physical Review B* 89.18 (2014), p. 184516 (cit. on p. 8).

- [55] Tobias Kampfrath, Koichiro Tanaka, and Keith A. Nelson. “Resonant and nonresonant control over matter and light by intense terahertz transients.” In: *Nature Photonics* 7.9 (2013), pp. 680–690 (cit. on p. 8).
- [56] Tobias Kampfrath et al. “Coherent terahertz control of antiferromagnetic spin waves.” In: *Nature Photonics* 5.1 (2011), pp. 31–34 (cit. on p. 8).
- [57] B. Keimer, S. A. Kivelson, M. R. Norman, S. Uchida, and J. Zaanen. “From quantum matter to high-temperature superconductivity in copper oxides.” In: *Nature* 518.7538 (2015), pp. 179–186 (cit. on p. 6).
- [58] B. Keimer and J. E. Moore. “The physics of quantum materials.” In: *Nature Physics* 13.11 (2017), pp. 1045–1055 (cit. on p. 6).
- [59] V. M. Khmara, N. M. Kovtun, and G. A. Troitskii. “Spin configuration of  $\text{ErFeO}_3$  below the ordering temperature of erbium.” In: *Solid State Communications* 15.11 (1974), pp. 1769–1771 (cit. on p. 79).
- [60] J. M. Kiat and Thierry Roisnel. “Rietveld analysis of strontium titanate in the Müller state.” In: *Journal of Physics: Condensed Matter* 8.19 (May 1996), pp. 3471–3475 (cit. on p. 35).
- [61] A. V. Kimel, A. Kirilyuk, P. A. Usachev, R. V. Pisarev, A. M. Balbashov, and Th Rasing. “Ultrafast non-thermal control of magnetization by instantaneous photomagnetic pulses.” In: *Nature* 435.7042 (2005), pp. 655–657 (cit. on p. 99).
- [62] A. V. Kimel, C. D. Stanciu, P. A. Usachev, R. V. Pisarev, V. N. Gridnev, A. Kirilyuk, and Th. Rasing. “Optical excitation of antiferromagnetic resonance in  $\text{TmFeO}_3$ .” In: *Physical Review B* 74.6 (2006), p. 060403 (cit. on p. 81).
- [63] Andrei Kirilyuk, Alexey V. Kimel, and Theo Rasing. “Ultrafast optical manipulation of magnetic order.” In: *Reviews of Modern Physics* 82.3 (2010), pp. 2731–2784 (cit. on p. 93).

- [64] Andrei Kirilyuk, Alexey V. Kimel, and Theo Rasing. "Ultrafast optical manipulation of magnetic order." In: *Reviews of Modern Physics* 82.3 (2010), pp. 2731–2784 (cit. on p. 107).
- [65] W. Kleemann, A. Albertini, M. Kuss, and R. Lindner. "Optical detection of symmetry breaking on a nanoscale in SrTiO<sub>3</sub>:Ca." In: *Ferroelectrics* 203.1 (1997), pp. 57–74 (cit. on p. 45).
- [66] C. S. Koonce, Marvin L. Cohen, J. F. Schooley, W. R. Hosler, and E. R. Pfeiffer. "Superconducting Transition Temperatures of Semiconducting SrTiO<sub>3</sub>." In: *Physical Review* 163.2 (1967), pp. 380–390 (cit. on p. 37).
- [67] N. Koshizuka and S. Ushioda. "Inelastic-light-scattering study of magnon softening in ErFeO<sub>3</sub>." In: *Physical Review B* 22.11 (1980), pp. 5394–5399 (cit. on pp. 80, 81, 88).
- [68] A. J. Kurtzig and W. Shockley. "Measurement of the Domain-Wall Energy of the Orthoferrites." In: *Journal of Applied Physics* 39.12 (1968), pp. 5619–5630 (cit. on p. 82).
- [69] L. D. Landau. "On the theory of phase transitions." In: *Zh.Eksp.Teor.Fiz.* 7 (1937), pp. 19–32 (cit. on p. 5).
- [70] Y. Le Page and Paul Saxe. "Symmetry-general least-squares extraction of elastic coefficients from ab initio total energy calculations." In: *Physical Review B* 63.17 (2001), p. 174103 (cit. on p. 60).
- [71] June Hyuk Lee et al. "A strong ferroelectric ferromagnet created by means of spin–lattice coupling." In: *Nature* 466.7309 (2010), pp. 954–958 (cit. on p. 107).
- [72] Xian Li, Tian Qiu, Jiahao Zhang, Edoardo Baldini, Jian Lu, Andrew M. Rappe, and Keith A. Nelson. "Terahertz field-induced ferroelectricity in quantum paraelectric SrTiO<sub>3</sub>." In: *Science* 364.6445 (2019), pp. 1079–1082 (cit. on p. 108).

- [73] Y. L. Li et al. "Phase transitions and domain structures in strained pseudocubic (100) SrTiO<sub>3</sub> thin films." In: *Physical Review B* 73.18 (2006), p. 184112 (cit. on p. 39).
- [74] Roman Mankowsky. "Nonlinear phononics and structural control of strongly correlated materials." PhD thesis. Universität Hamburg Hamburg, Nov. 2016 (cit. on p. 11).
- [75] Roman Mankowsky, Michael Först, and Andrea Cavalleri. "Non-equilibrium control of complex solids by nonlinear phononics." In: *Reports on Progress in Physics* 79.6 (2016), p. 064503 (cit. on p. 24).
- [76] R. Mankowsky et al. "Nonlinear lattice dynamics as a basis for enhanced superconductivity in YBa<sub>2</sub>Cu<sub>3</sub>O<sub>6.5</sub> ." In: *Nature* 516.7529 (2014), pp. 71–73 (cit. on p. 9).
- [77] R. Mankowsky et al. "Nonlinear lattice dynamics as a basis for enhanced superconductivity in YBa<sub>2</sub>Cu<sub>3</sub>O<sub>6.5</sub> ." en. In: *Nature* 516.7529 (2014), pp. 71–73 (cit. on p. 27).
- [78] A. A. Maradudin and R. F. Wallis. "Ionic Raman Effect. I. Scattering by Localized Vibration Modes." In: *Physical Review B* 2 (1970), pp. 4294–4299 (cit. on p. 22).
- [79] M. Marezio, J. P. Remeika, and P. D. Dernier. "The crystal chemistry of the rare earth orthoferrites." In: *Acta Crystallographica Section B: Structural Crystallography and Crystal Chemistry* 26.12 (1970), pp. 2008–2022 (cit. on p. 76).
- [80] T. P. Martin and L. Genzel. "Ionic Raman Scattering and Ionic Frequency Mixing." In: *physica status solidi (b)* 61.2 (1974), pp. 493–502 (cit. on p. 22).
- [81] R. V. Mikhaylovskiy et al. "Ultrafast optical modification of exchange interactions in iron oxides." In: *Nature Communications* 6.1 (2015), pp. 1–9 (cit. on p. 99).

- [82] M. Mitrano et al. "Possible light-induced superconductivity in  $K_3C_{60}$  at high temperature." In: *Nature* 530.7591 (2016), pp. 461–464 (cit. on p. 8).
- [83] A. S. Moskvin, A. V. Zenkov, E. A. Ganshina, G. S. Krinchik, and M. M. Nishanova. "Anisotropy of the circular magneto-optics of orthoferrites: A theoretical consideration on the basis of the charge-transfer transitions and exchange-relativistic interactions concept." In: *Journal of Physics and Chemistry of Solids* 54.1 (1993), pp. 101–105 (cit. on p. 83).
- [84] Arash A. Mostofi, Jonathan R. Yates, Giovanni Pizzi, Young-Su Lee, Ivo Souza, David Vanderbilt, and Nicola Marzari. "An updated version of wannier90: A tool for obtaining maximally-localised Wannier functions." In: *Computer Physics Communications* 185.8 (2014), pp. 2309–2310 (cit. on p. 60).
- [85] K. A. Müller and H. Burkard. "SrTiO<sub>3</sub>: An intrinsic quantum paraelectric below 4 K." In: *Physical Review B* 19.7 (1979), pp. 3593–3602 (cit. on p. 36).
- [86] K. Alex Müller, W. Berlinger, and E. Tosatti. "Indication for a novel phase in the quantum paraelectric regime of SrTiO<sub>3</sub>." In: *Zeitschrift für Physik B Condensed Matter* 84.2 (1991), pp. 277–283 (cit. on p. 36).
- [87] Jun Nagamatsu, Norimasa Nakagawa, Takahiro Muranaka, Yuji Zenitani, and Jun Akimitsu. "Superconductivity at 39 K in magnesium diboride." In: *Nature* 410.6824 (2001), pp. 63–64 (cit. on p. 6).
- [88] Daniele Nicoletti and Andrea Cavalleri. "Nonlinear light–matter interaction at terahertz frequencies." In: *Advances in Optics and Photonics* 8.3 (2016), pp. 401–464 (cit. on pp. 8, 10, 105).
- [89] David D. Nolte. *Photorefractive Effects and Materials*. Springer Science & Business Media, 2013 (cit. on p. 71).
- [90] T. F. Nova, A. Cartella, A. Cantaluppi, M. Först, D. Bossini, R. V. Mikhaylovskiy, A. V. Kimel, R. Merlin, and A. Cavalleri. "An effective magnetic field from

- optically driven phonons." In: *Nature Physics* 13.2 (2017), pp. 132–136 (cit. on pp. 25, 26).
- [91] T. F. Nova, A. Cartella, A. Cantaluppi, M. Först, D. Bossini, R. V. Mikhaylovskiy, A. V. Kimel, R. Merlin, and A. Cavalleri. "An effective magnetic field from optically driven phonons." In: *Nature Physics* 13.2 (2017), pp. 132–136 (cit. on p. 76).
- [92] T. F. Nova, A. S. Disa, M. Fechner, and A. Cavalleri. "Metastable ferroelectricity in optically strained SrTiO<sub>3</sub>." In: *Science* 364.6445 (2019), pp. 1075–1079 (cit. on p. 33).
- [93] A. Ohtomo and H. Y. Hwang. "A high-mobility electron gas at the LaAlO<sub>3</sub>/SrTiO<sub>3</sub> heterointerface." In: *Nature* 427.6973 (2004), pp. 423–426 (cit. on p. 72).
- [94] Sergei Orlov, Amnon Yariv, and Mordechai Segev. "Nonlinear self-phase matching of optical second harmonic generation in lithium niobate." In: *Applied Physics Letters* 68.12 (1996), pp. 1610–1612 (cit. on p. 71).
- [95] E. Pavarini, A. Yamasaki, J. Nuss, and O. K. Andersen. "How chemistry controls electron localization in 3d<sub>1</sub>perovskites: a Wannier-function study." In: *New Journal of Physics* 7 (Sept. 2005), pp. 188–188 (cit. on pp. 7, 8).
- [96] John P. Perdew, Adrienn Ruzsinszky, Gábor I. Csonka, Oleg A. Vydrov, Gustavo E. Scuseria, Lucian A. Constantin, Xiaolan Zhou, and Kieron Burke. "Restoring the Density-Gradient Expansion for Exchange in Solids and Surfaces." In: *Physical Review Letters* 100.13 (2008), p. 136406 (cit. on p. 60).
- [97] P. S. Pershan, J. P. van der Ziel, and L. D. Malmstrom. "Theoretical Discussion of the Inverse Faraday Effect, Raman Scattering, and Related Phenomena." In: *Physical Review* 143.2 (1966), pp. 574–583 (cit. on p. 93).

- [98] R. V. Pisarev, A. S. Moskvin, A. M. Kalashnikova, and Th. Rasing. “Charge transfer transitions in multiferroic BiFeO<sub>3</sub> and related ferrite insulators.” In: *Physical Review B* 79.23 (2009), p. 235128 (cit. on pp. 82, 95).
- [99] M. Porer et al. “Ultrafast Relaxation Dynamics of the Antiferrodistortive Phase in Ca Doped SrTiO<sub>3</sub>.” In: *Physical Review Letters* 121.5 (2018), p. 055701 (cit. on p. 48).
- [100] Paolo G. Radaelli. “Breaking symmetry with light: Ultrafast ferroelectricity and magnetism from three-phonon coupling.” In: *Physical Review B* 97.8 (Feb. 2018), p. 085145. (Visited on 10/13/2019) (cit. on pp. 25, 26, 108).
- [101] A. P. Ramirez. “Colossal magnetoresistance.” In: *Journal of Physics: Condensed Matter* 9.39 (1997), pp. 8171–8199 (cit. on p. 6).
- [102] N. Reyren et al. “Superconducting Interfaces Between Insulating Oxides.” In: *Science* 317.5842 (2007), pp. 1196–1199 (cit. on p. 107).
- [103] Matteo Rini, Ra’anan Tobey, Nicky Dean, Jiro Itatani, Yasuhide Tomioka, Yoshinori Tokura, Robert W. Schoenlein, and Andrea Cavalleri. “Control of the electronic phase of a manganite by mode-selective vibrational excitation.” In: *Nature* 449.7158 (2007), pp. 72–74 (cit. on pp. 8, 28).
- [104] Carl Willem Rischau et al. “A ferroelectric quantum phase transition inside the superconducting dome of Sr<sub>1-x</sub>Ca<sub>x</sub>TiO<sub>3-δ</sub>.” In: *Nature Physics* 13.7 (2017), pp. 643–648 (cit. on p. 37).
- [105] F. Rossol. “Temperature dependence of rare-earth orthoferrite properties relevant to propagating domain device applications.” In: *IEEE Transactions on Magnetism* 5.3 (1969), pp. 562–565 (cit. on p. 82).
- [106] T. Sakudo and H. Unoki. “Dielectric Properties of SrTiO<sub>3</sub> at Low Temperatures.” In: *Physical Review Letters* 26.14 (Apr. 1971), pp. 851–853 (cit. on pp. 35, 36, 65).

- [107] H. Sato and M. Naito. "Increase in the superconducting transition temperature by anisotropic strain effect in (001)  $\text{La}_{1.85}\text{Sr}_{0.15}\text{CuO}_4$  thin films on  $\text{LaSrAlO}_4$  substrates." In: *Physica C: Superconductivity* 274.3 (1997), pp. 221–226 (cit. on p. 39).
- [108] Darrell G. Schlom, Long-Qing Chen, Chang-Beom Eom, Karin M Rabe, Stephen K Streiffer, and Jean-Marc Triscone. "Strain Tuning of Ferroelectric Thin Films." In: *Annual Review of Materials Research* 37.1 (2007), pp. 589–626 (cit. on pp. 9, 37, 38).
- [109] J. F. Schooley, W. R. Hosler, and Marvin L. Cohen. "Superconductivity in Semiconducting  $\text{SrTiO}_3$ ." In: *Physical Review Letters* 12.17 (1964), pp. 474–475 (cit. on p. 37).
- [110] Takashi Shimizu and Hideyo Okushi. "Intrinsic electrical properties of  $\text{Au}/\text{SrTiO}_3$  Schottky junctions." In: *Journal of Applied Physics* 85.10 (1999), pp. 7244–7251 (cit. on p. 58).
- [111] C. D. Stanciu, F. Hansteen, A. V. Kimel, A. Kirilyuk, A. Tsukamoto, A. Itoh, and Th. Rasing. "All-Optical Magnetic Recording with Circularly Polarized Light." In: *Physical Review Letters* 99.4 (2007), p. 047601 (cit. on p. 107).
- [112] A. Stupakiewicz, K. Szerenos, D. Afanasiev, A. Kirilyuk, and A. V. Kimel. "Ultrafast nonthermal photo-magnetic recording in a transparent medium." In: *Nature* 542.7639 (2017), pp. 71–74 (cit. on p. 107).
- [113] Alaska Subedi, Andrea Cavalleri, and Antoine Georges. "Theory of nonlinear phononics for coherent light control of solids." In: *Physical Review B* 89.22 (2014), p. 220301 (cit. on pp. 9, 25, 28, 29).
- [114] Allen Taflove and Susan C. Hagness. *Computational electrodynamics: the finite-difference time-domain method*. 3rd ed. Artech House antennas and propagation library. Boston, MA: Artech House, 2005 (cit. on pp. 94, 117).

- [115] M. Takesada, M. Itoh, and T. Yagi. "Perfect Softening of the Ferroelectric Mode in the Isotope-Exchanged Strontium Titanate of  $\text{SrTi}_{18}\text{O}_3$  Studied by Light Scattering." In: *Physical Review Letters* 96.22 (2006), p. 227602 (cit. on pp. 37, 38, 55).
- [116] Yoshinori Tokura, Masashi Kawasaki, and Naoto Nagaosa. "Emergent functions of quantum materials." In: *Nature Physics* 13.11 (2017), pp. 1056–1068 (cit. on p. 6).
- [117] Y. Tomioka, A. Asamitsu, H. Kuwahara, Y. Moritomo, and Y. Tokura. "Magnetic-field-induced metal-insulator phenomena in  $\text{Pr}_{1-x}\text{Ca}_x\text{MnO}_3$  with controlled charge-ordering instability." In: *Physical Review B* 53.4 (1996), R1689–R1692 (cit. on p. 28).
- [118] L. T. Tsymbal, Ya. B. Bazaliy, G. N. Kakazei, Yu. I. Nepochatykh, and P. E. Wigen. "Natural behavior of the magnetization under spontaneous reorientation:  $\text{TmFeO}_3$ ,  $\text{ErFeO}_3$ ." In: *Low Temperature Physics* 31.3 (2005), pp. 277–282 (cit. on p. 78).
- [119] L. T. Tsymbal, G. N. Kakazei, and Ya. B. Bazaliy. "Single-domain-wall states in millimeter-scale samples of  $\text{ErFeO}_3$ ." In: *Physical Review B* 79.9 (2009), p. 092414 (cit. on p. 82).
- [120] P. A. Usachev, R. V. Pisarev, A. M. Balbashov, A. V. Kimel, A. Kirilyuk, and Th. Rasing. "Optical properties of thulium orthoferrite  $\text{TmFeO}_3$ ." In: *Physics of the Solid State* 47.12 (2005), pp. 2292–2298 (cit. on p. 82).
- [121] Hiromoto Uwe and Tunetaro Sakudo. "Stress-induced ferroelectricity and soft phonon modes in  $\text{SrTiO}_3$ ." In: *Physical Review B* 13.1 (1976), pp. 271–286 (cit. on p. 55).
- [122] David Vanderbilt, S. H. Taole, and Shobhana Narasimhan. "Anharmonic elastic and phonon properties of Si." In: *Physical Review B* 40.8 (1989), pp. 5657–5668 (cit. on p. 59).

- [123] E. L. Venturini, G. A. Samara, M. Itoh, and R. Wang. "Pressure as a probe of the physics of 18O-substituted SrTiO<sub>3</sub>." In: *Physical Review B* 69.18 (2004), p. 184105 (cit. on p. 38).
- [124] B. E. Vugmeister and M. D. Glinchuk. "Dipole glass and ferroelectricity in random-site electric dipole systems." In: *Reviews of Modern Physics* 62.4 (1990), pp. 993–1026 (cit. on p. 71).
- [125] R. F. Wallis and A. A. Maradudin. "Ionic Raman Effect. II. The First-Order Ionic Raman Effect." In: *Physical Review B* 3.6 (1971), pp. 2063–2075 (cit. on p. 22).
- [126] Ruiping Wang and Mitsuru Itoh. "Suppression of the quantum fluctuation in 18O-enriched strontium titanate." In: *Physical Review B* 64.17 (2001), p. 174104 (cit. on pp. 37, 38).
- [127] R. L. White. "Review of Recent Work on the Magnetic and Spectroscopic Properties of the Rare-Earth Orthoferrites." In: *Journal of Applied Physics* 40.3 (1969), pp. 1061–1069 (cit. on pp. 78, 79).
- [128] R. M. White, R. J. Nemanich, and Conyers Herring. "Light scattering from magnetic excitations in orthoferrites." In: *Physical Review B* 25.3 (1982), pp. 1822–1836 (cit. on p. 81).
- [129] D. L. Wood, L. M. Holmes, and J. P. Remeika. "Exchange Fields and Optical Zeeman Effect in ErFeO<sub>3</sub>." In: *Physical Review* 185.2 (1969), pp. 689–695 (cit. on pp. 79, 83).
- [130] S. R. Woodford, A. Bringer, and S. Blügel. "Interpreting magnetization from Faraday rotation in birefringent magnetic media." In: *Journal of Applied Physics* 101.5 (2007), p. 053912 (cit. on p. 86).
- [131] Keita Yamaguchi, Takayuki Kurihara, Yasuo Minami, Makoto Nakajima, and Tohru Suemoto. "Terahertz Time-Domain Observation of Spin Reorientation in Orthoferrite ErFeO<sub>3</sub> through Magnetic Free Induction Decay." In: *Physical Review Letters* 110.13 (2013), p. 137204 (cit. on pp. 79, 100).

- [132] T. Yamaguchi. "Theory of spin reorientation in rare-earth orthochromites and orthoferrites." In: *Journal of Physics and Chemistry of Solids* 35.4 (1974), pp. 479–500 (cit. on p. 80).
- [133] A. Yamanaka, M. Kataoka, Y. Inaba, K. Inoue, B. Hehlen, and E. Courtens. "Evidence for competing orderings in strontium titanate from hyper-Raman scattering spectroscopy." In: *EPL (Europhysics Letters)* 50.5 (2000), p. 688 (cit. on pp. 35, 36).
- [134] Shengyuan A. Yang, Xiaoqin Li, Alan D. Bristow, and J. E. Sipe. "Second harmonic generation from tetragonal centrosymmetric crystals." In: *Physical Review B* 80.16 (2009), p. 165306 (cit. on p. 46).
- [135] Kane Yee. "Numerical solution of initial boundary value problems involving maxwell's equations in isotropic media." In: *IEEE Transactions on Antennas and Propagation* 14.3 (1966), pp. 302–307 (cit. on pp. 94, 117).
- [136] A. V. Zenkov, B. B. Krichevtsov, A. S. Moskvina, K. M. Mukimov, R. V. Pisarev, and M. M. Ruvinshtein. "Anisotropy of the Faraday effect in the weak ferromagnet  $\text{YFeO}_3$ ." In: *Soviet Physics - JETP (English Translation)* 69.4 (1989), pp. 792–796 (cit. on p. 85).
- [137] Hai-Tian Zhang, Lei Zhang, Debangshu Mukherjee, Yuan-Xia Zheng, Ryan C. Haislmaier, Nasim Alem, and Roman Engel-Herbert. "Wafer-scale growth of  $\text{VO}_2$  thin films using a combinatorial approach." In: *Nature Communications* 6.1 (2015), pp. 1–8 (cit. on p. 6).
- [138] Xinyuan Zhao and David Vanderbilt. "Phonons and lattice dielectric properties of zirconia." In: *Physical Review B* 65.7 (2002), p. 075105 (cit. on p. 95).
- [139] W. Zhong and D. Vanderbilt. "Effect of quantum fluctuations on structural phase transitions in  $\text{SrTiO}_3$  and  $\text{BaTiO}_3$ ." In: *Physical Review B* 53.9 (1996), pp. 5047–5050 (cit. on pp. 36, 37).

- [140] P. Zubko, G. Catalan, A. Buckley, P. R. L. Welche, and J. F. Scott. "Strain-Gradient-Induced Polarization in SrTiO<sub>3</sub> Single Crystals." In: *Physical Review Letters* 99.16 (2007), p. 167601 (cit. on p. 63).
- [141] P. Zubko, G. Catalan, A. Buckley, P. R. L. Welche, and J. F. Scott. "Strain-Gradient-Induced Polarization in SrTiO<sub>3</sub> Single Crystals." In: *Physical Review Letters* 99.16 (2007), p. 167601 (cit. on p. 65).
- [142] Pavlo Zubko, Gustau Catalan, and Alexander K. Tagantsev. "Flexoelectric Effect in Solids." In: *Annual Review of Materials Research* 43.1 (2013), pp. 387–421 (cit. on pp. 63, 72, 107).



**COLOPHON**

*Final Version* as of February 17, 2020 (Hamburg).